

2.2

Active Flow Control strategies and novel tests-rigs for tidal turbines composite blades

Lead Beneficiary SSPA Sweden AB

Delivery date 2021-11-28

Dissemination level Public

Status Final

Version 1.0

Keywords [Keywords]



This project has received funding from the European Union's Horizon 2020 research and innovation programme under grant agreement No 815278.

www.nemmo.eu  [@NEMMO_Project](https://twitter.com/NEMMO_Project)  info@nemmo.eu

Document Information

Grant Agreement Number	815278
Project Acronym	NEMMO
Work Package	WP2
Task(s)	2.2.1, 2.2.2, 2.23, 2.2.4
Deliverable	D2.2
Title	Active Flow Control strategies and novel tests-rigs for tidal turbines composite blades
Author(s)	Michael Leer-Andersen, Yan Delure
File Name	Nemmo-D2.2

Change Record

Revision	Date	Description	Reviewer
1.0	2021-11-28	Final deliverable D2.2 to EC	EC

Table of contents

Introduction.....	4
Constant cross-sectional profiles.....	5
Profiles	5
Results.....	9
Rotating turbine	20
Model setup	24
Design.....	24
Results.....	28
Comparison between SSPA bronze and CANOE carbon fibre blades	30
LDV measurements on Blade 1	41
Blade geometry 2.....	64
Surface roughness modelling	74
Methodology	74
Results.....	79
Methodology	85
Recessed cavities	86
Raised structures	89
Concluding remarks on surface roughness modelling.....	96
Conclusion: the effect of surface texturing of blade on performance coefficient of Magallanes turbine	97
References.....	98

Introduction

This document reports the work conducted during the task 2.2 of the work package 2 of the NEMMO project. The overall goal of the NEMMO project is to improve blade of tidal turbine in composite material for tidal energy generation.

The work includes a large test programme at SSPA, including 3 sets of blades, which includes carbon fibre blades from Canoe and bronze blades from SSPA for blade geometry 1 and 2. It also includes testing of constant cross sectional profiles at 0.5R and 0.8R on the original blades. Two types of flow control were tested but reported in T2.3. Furthermore, LDV (Laser Doppler Velocometry) was used to measure the flow field at 3 planes upstream and downstream of the blades. Finally, surface roughness modelling is described. CFD and LES modelling are mainly described in WP1.

Constant cross-sectional profiles

Constant cross-sectional profiles have been manufactured and tested at SSPA. The profiles are not rotating but are instead attached to the roof of the SSPA cavitation tunnel on a rotating table to be able to test a range of angle attack. The reason for this approach (3 bladed rotating turbine is also tested) is two fold.

1. The scale is significantly increased (from 1/38 for rotating turbine to 1/7 for the constant cross-sectional profiles), which allows less Reynolds number scaling to full scale. This is important for passive and active flow control, as for example microtexturing and boundary layer control methods. The scale for the rotating turbine also renders it almost most impossible to create the necessary tubing and flow outlets inside the blades, which is much easier for the larger scale cross sectional profiles.
2. For CFD validation purposes, especially Q-blade used in WP1 will benefit from measurements of constant cross-sectional profiles.

The profiles used are a cross section of the original Magellans blades at $R=0.5$ and $R=0.8$, the difference in the geometry can be seen from Figure 5, where the small cross section have been scale to have the same chord length as the large cross section for illustration purposes.

Profiles

The profiles have been manufactured at SSPA using a CNC milling machine from a solid block of aluminium. The profiles have been primed and coated to ensure that they are hydraulically smooth. The choice of milling the profiles from a solid block of aluminum were chosen to allow using the profiles for testing microtexturing and especially AFC (Active Flow Control) for which the profiles can be modified after the original profiles have been tested in the cavitation tunnel.

Figure 4 show the geometry of each constant cross section profile. Both have a span of 0.4m, where the profile for $R=0.5$ have a chord length of 0250mm and $R=0.8$ a chord length of 129.42mm. Both profiles therefore have the same scale factor to full scale, and the difference in chord length reflects the difference in full scale chord length at $R=0.5$ and 0.8.

The method to extract the profiles are as follows. Both radii have been defined as cylindrical surfaces have been defined and the intersection between the blade and the cylindrical surfaces are created, see Figure 1. This intersection is not plane, and to simulate the flow over a rotating blade on a non-rotating constant cross-sectional profile, the correct method to use is to unroll the profile. In other words, the cylindrical surfaces at constant radial distance from the hub are unrolled, and not projected. As they are unrolled and not projected, the chord length is actually longer than if the profiles were extracted by either plane cut or a projection of the cylindrical cut. However, as the flow passes over the blades in a cylindrical coordinate system, the unrolling procedure is the correct method. Figure 2 shows the unrolled surface and profiles.

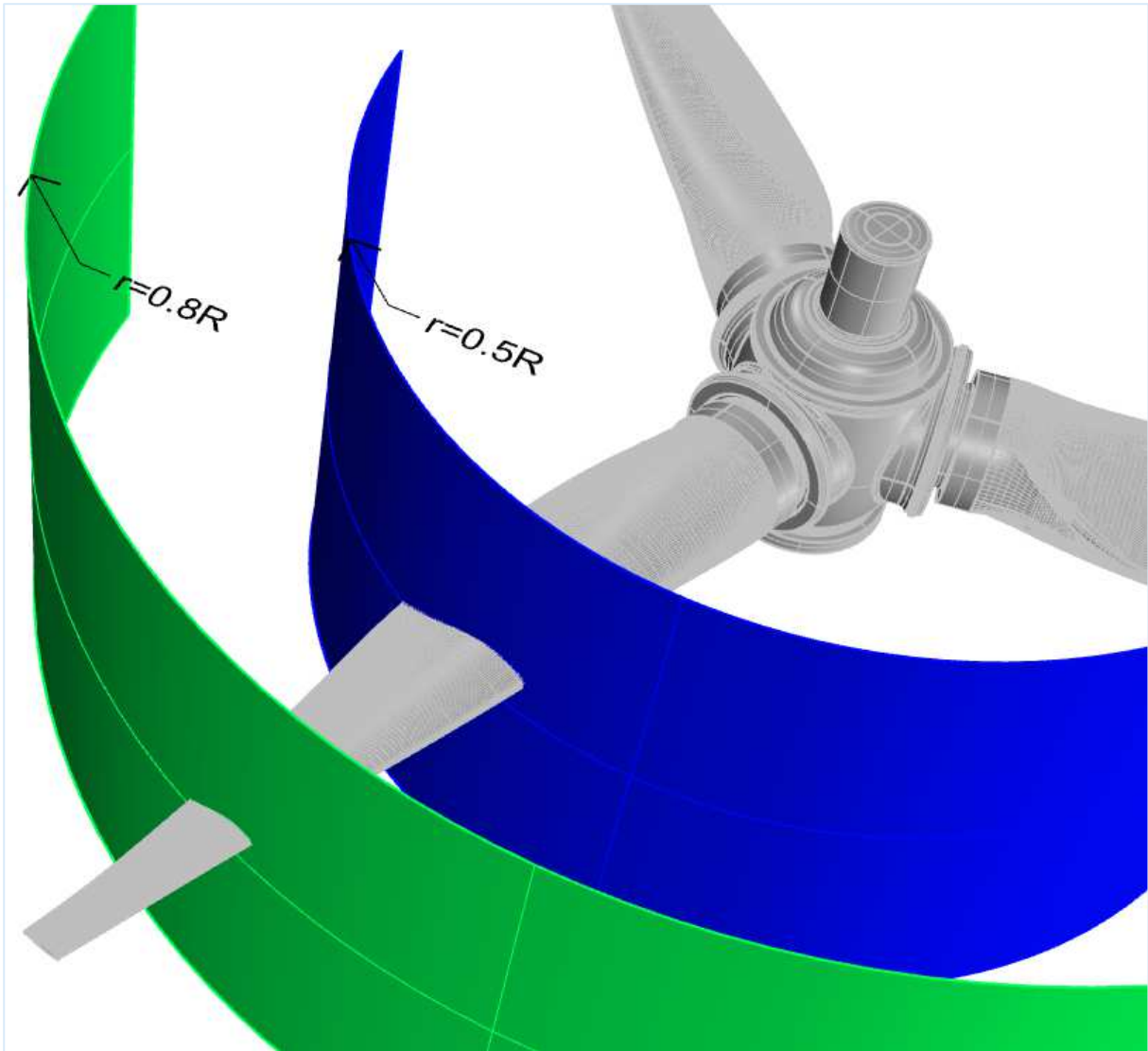


Figure 1: Radial intersections

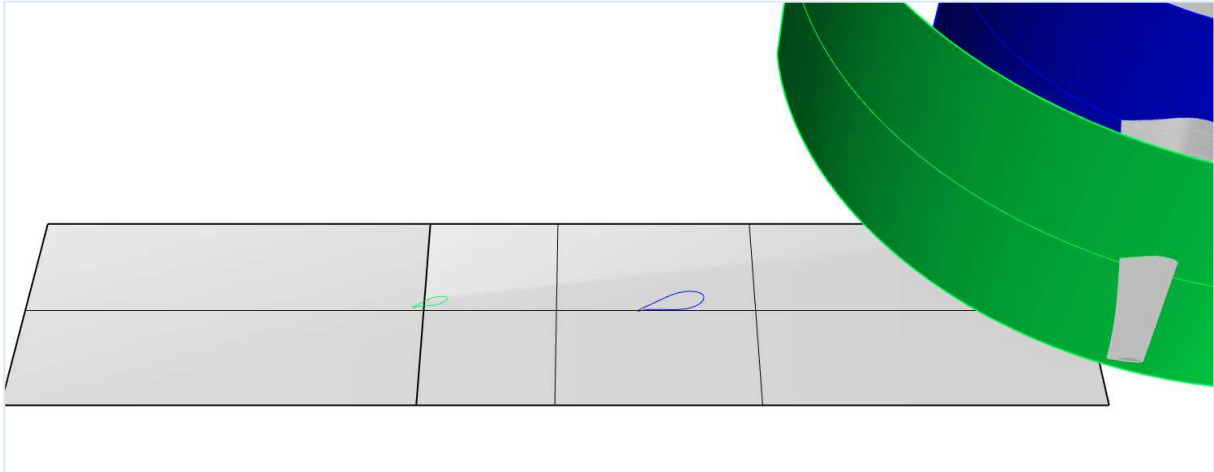


Figure 2: Unrolled surface and profile

In summary the chord length sizes are as follows

	Full scale		Model scale		Scale factor
	r [mm]	Chord length [mm]	Chord length [mm]	r [mm]	
r=0.8R	7600	810.4	129.4	1213.6	6.26
r=0.5R	4750	1562.4	250.0	760.0	6.25

The completed profiles are shown in Figure 6. The appendage in the bottom of each profile is fixed to top tunnel section on a turntable which rotates to test a range of pitch angles.

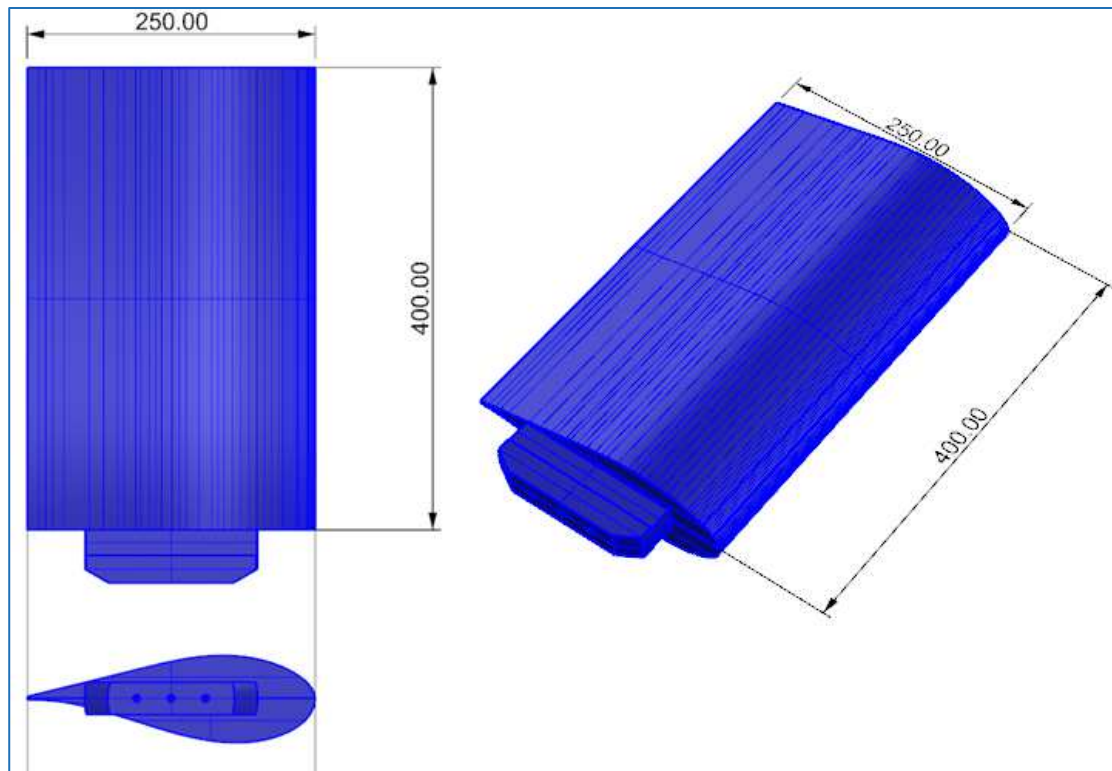


Figure 3: R=0.5 profile

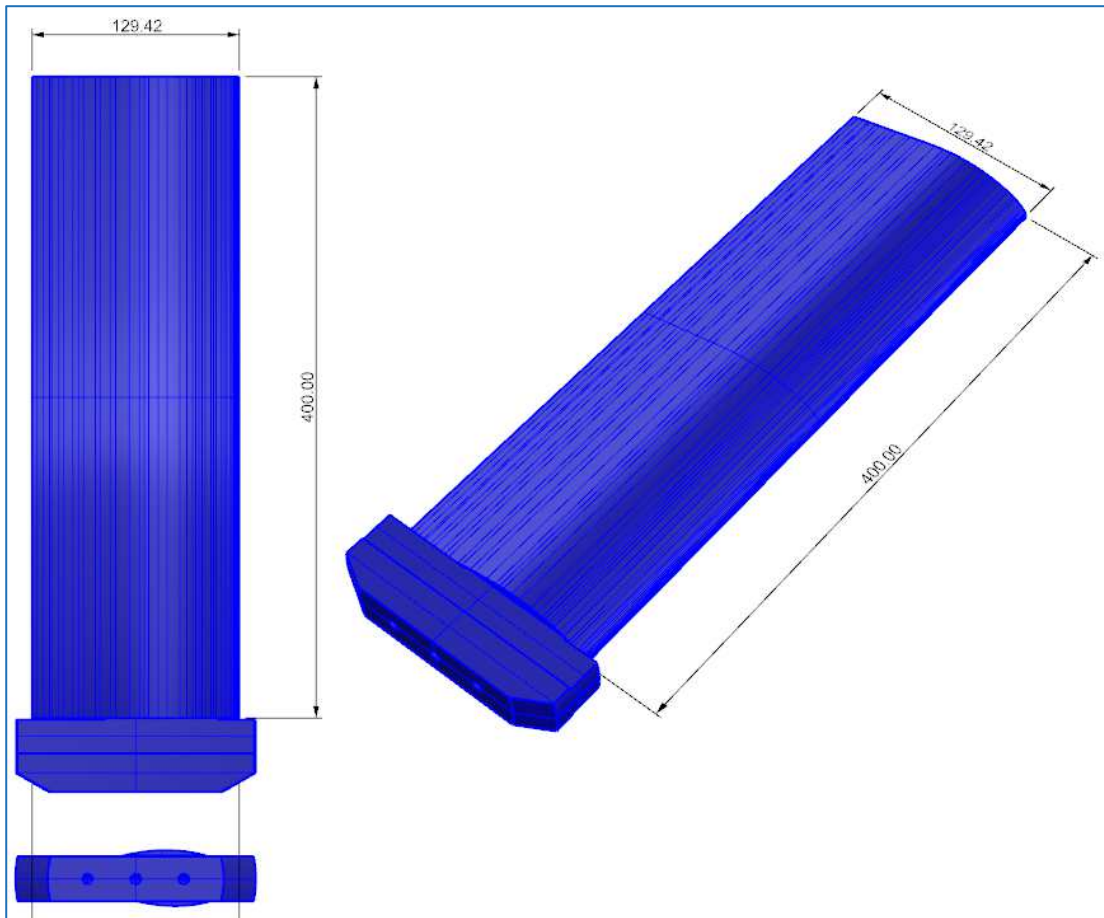


Figure 4: R=0.8 profile

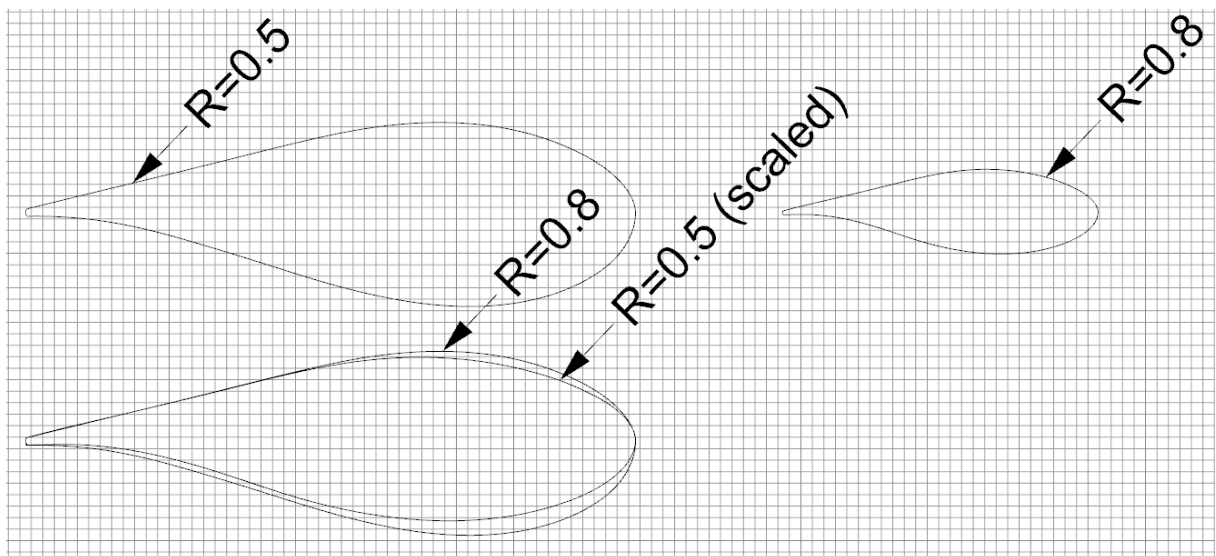


Figure 5: Comparison of cross sections



Figure 6: Finished profiles

Results

The following tests have been completed

serie	Test	Wing	V_0	P_0	A	c
1	1	R=0.5	5	250.000	0.10000	0.25000
1	2	R=0.5	7	250.000	0.10000	0.25000
1	3	R=0.5	7	102.275	0.10000	0.25000
2	1	R=0.8	5	250.000	0.05177	0.12942
2	2	R=0.8	7	250.000	0.05177	0.12942
2	3	R=0.8	7	36.900	0.05177	0.12942
2	4	R=0.8	9	250.000	0.05177	0.12942

where V_0 refers to the tunnel flow speed, P_0 the tunnel pressure in kPa (102.275kPa being atmospheric pressure, 250kPa the maximum pressure corresponding to 15m's water depth full scale)

Using a coordinate system as shown in the figure below, with the center of rotation and moment as shown in figures Figure 7-Figure 8. Positive pitch angle leading edge down in Figure 7.

All data have been made dimensionless with

$$C_{D,L,Z} = \frac{F}{0.5 \cdot \rho \cdot A \cdot U^2}$$

$$C_{Mx,My,MZ} = \frac{F}{0.5 \rho A c U^2}$$

where c is the chord length and A is the chord length times profile span (0.4m for both)

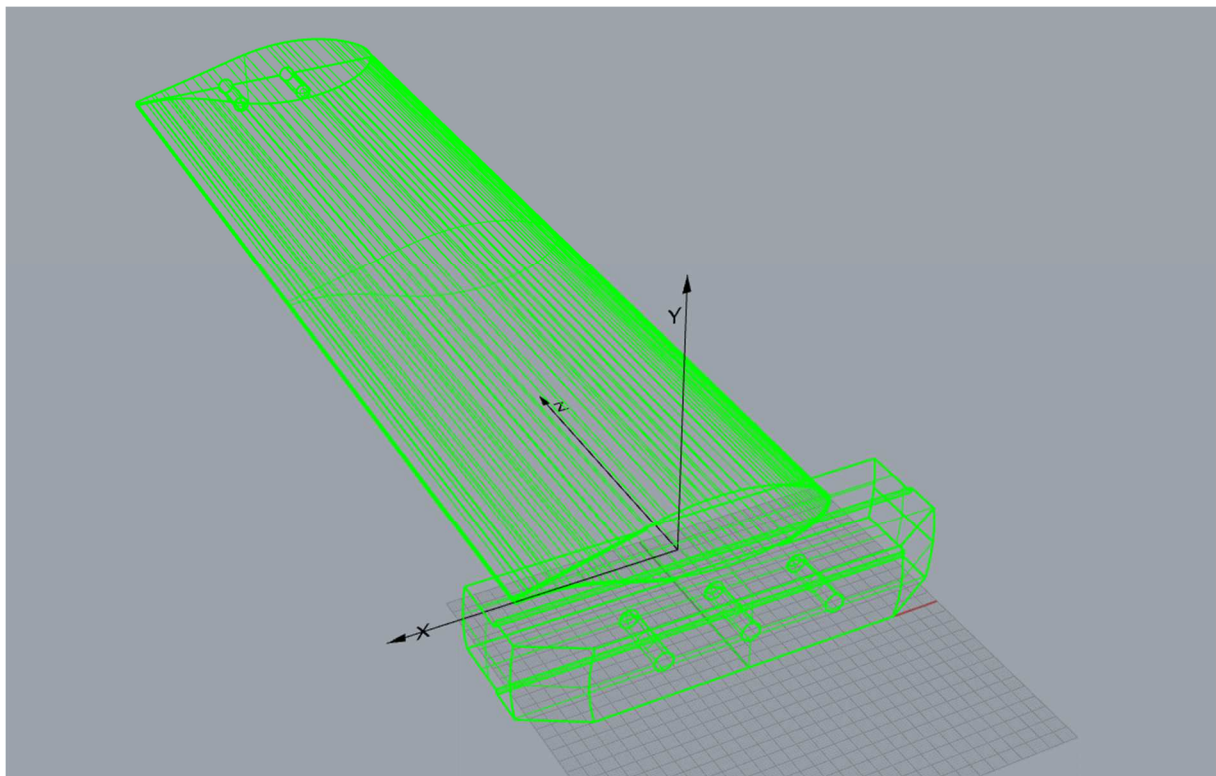


Figure 7: Coordinate system

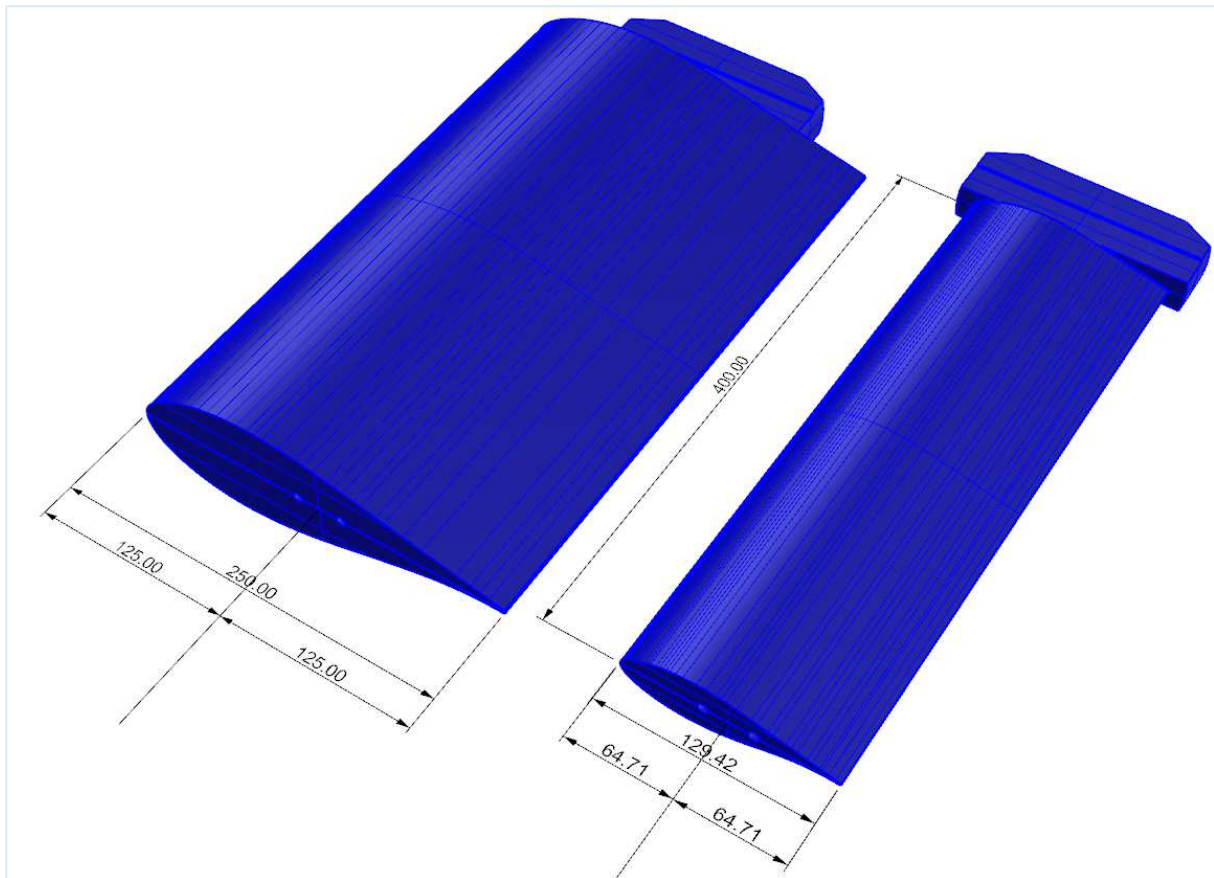
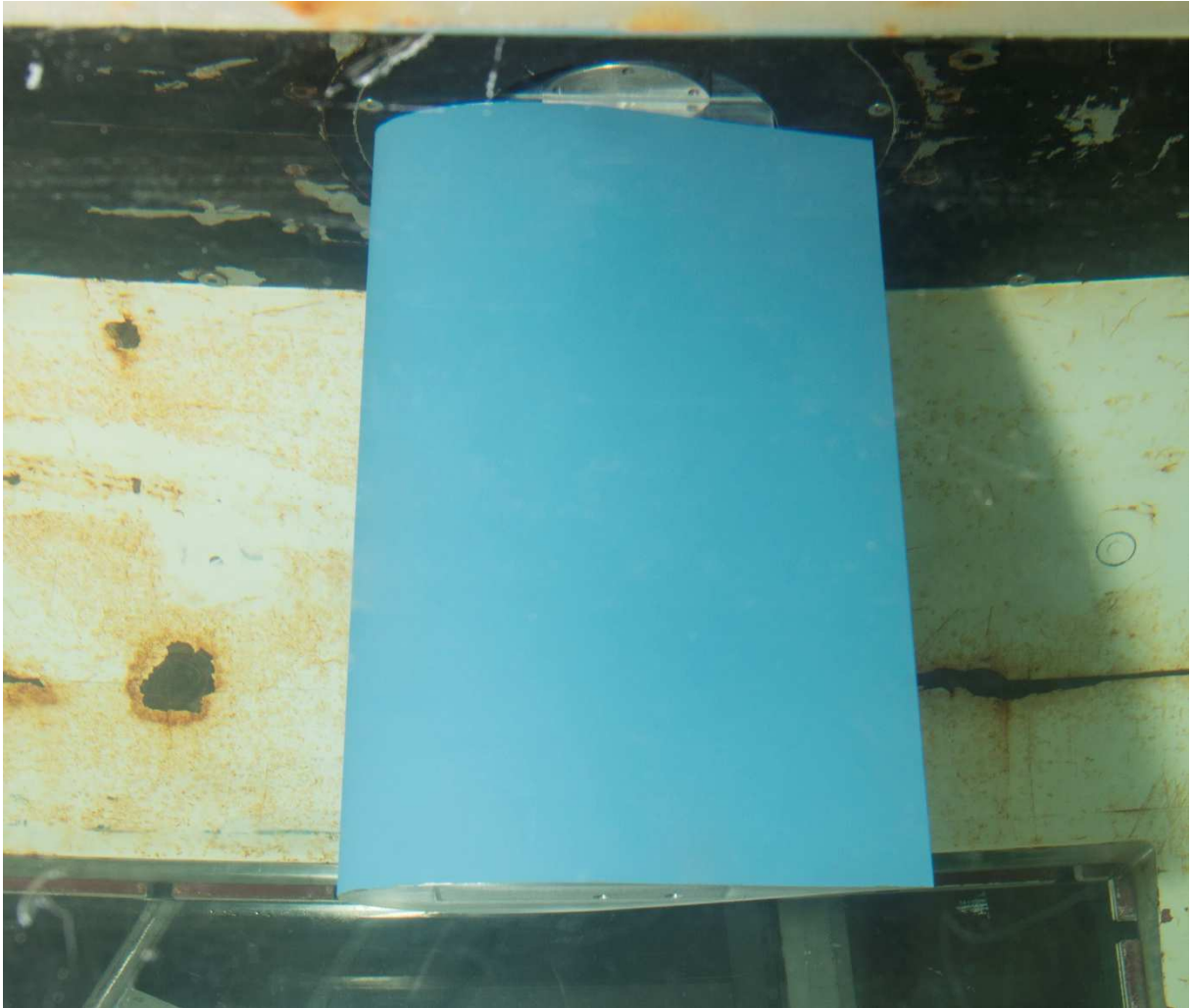


Figure 8: Center of rotation and moment

In the graphs below two graphs are shown for each test series. The first show the primary results of C_L , C_D , C_{Mz} , and C_L/C_D . Please note that the dimensionless coefficients have been scaled to better show the results. The secondary results consist of C_z , C_{My} and C_{Mx} . These are included as they indicate the effect of the walls of the cavitation tunnel and end effects of the profile.

The tests were completed using test section 1, which have a circular test section with a diameter of 1m. The picture below shows the large profile ($R=0.5$) installed in the test section.



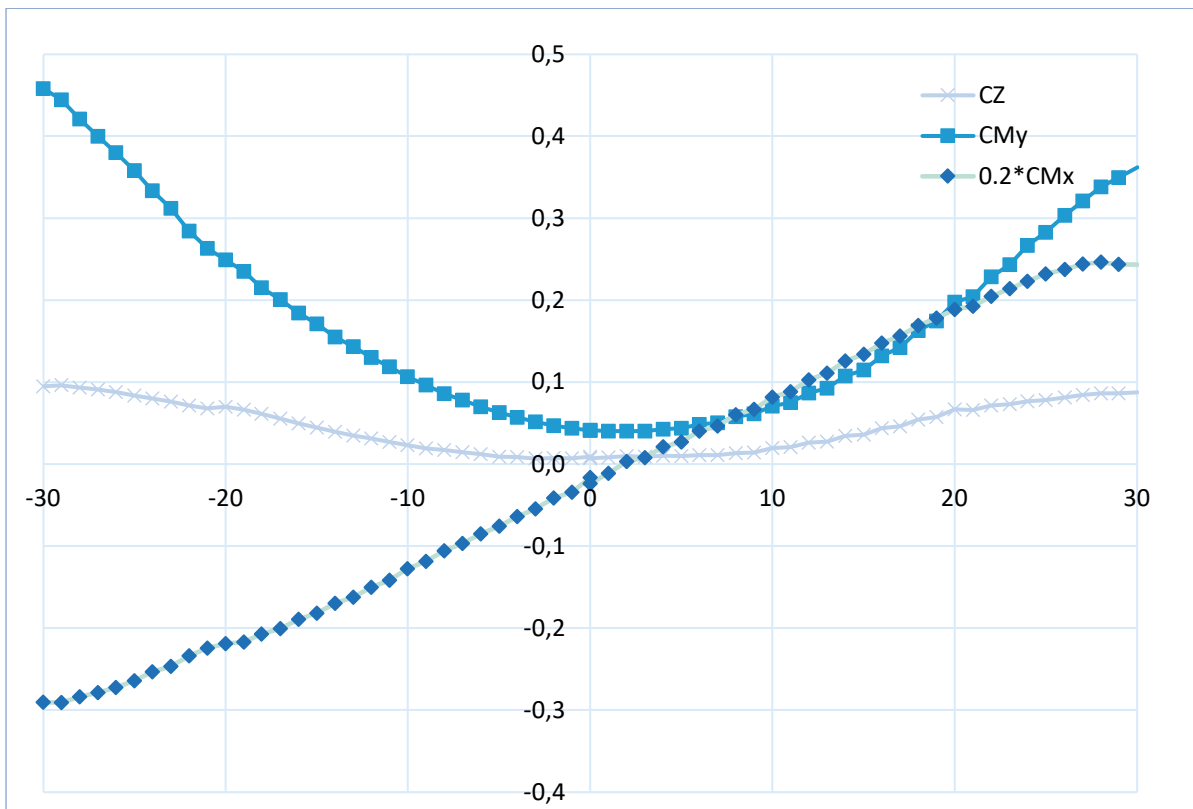
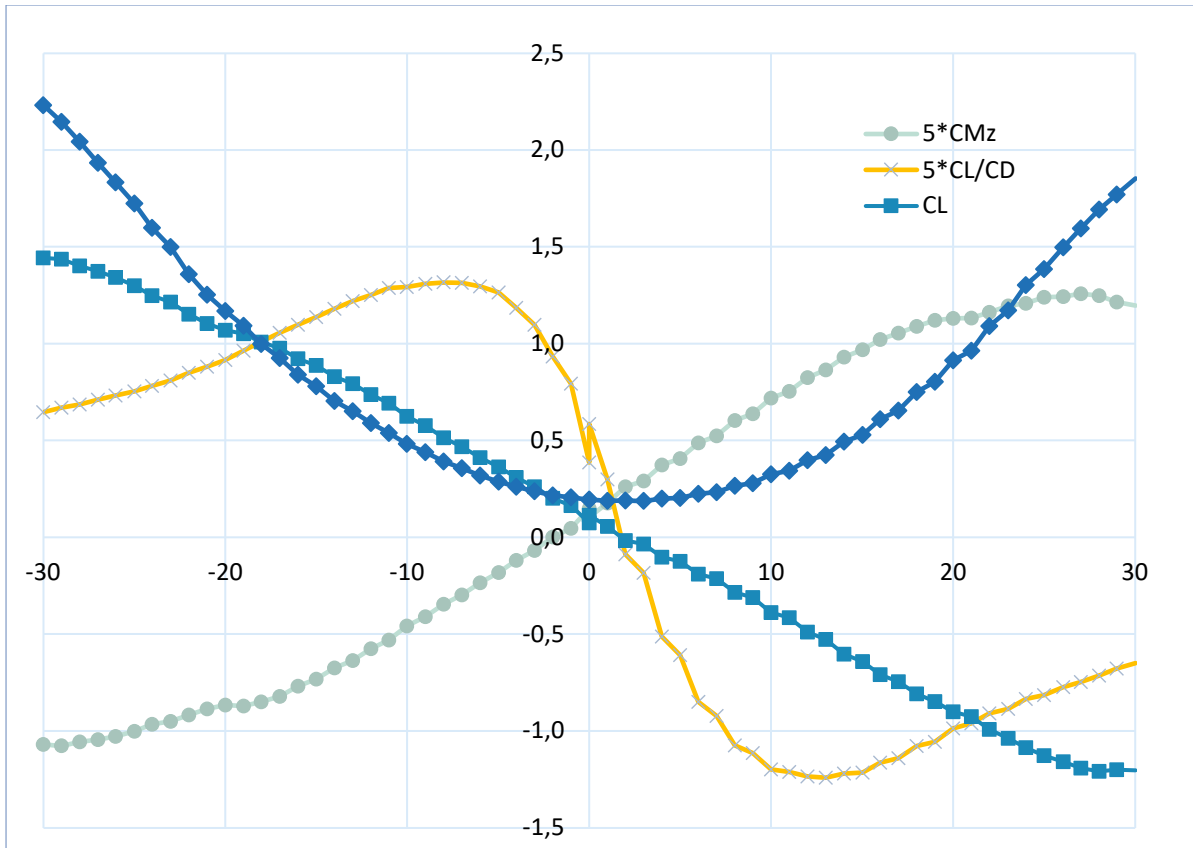


Figure 9: $R=0.5, U=5\text{m/s}, P_0=250\text{kPa}$

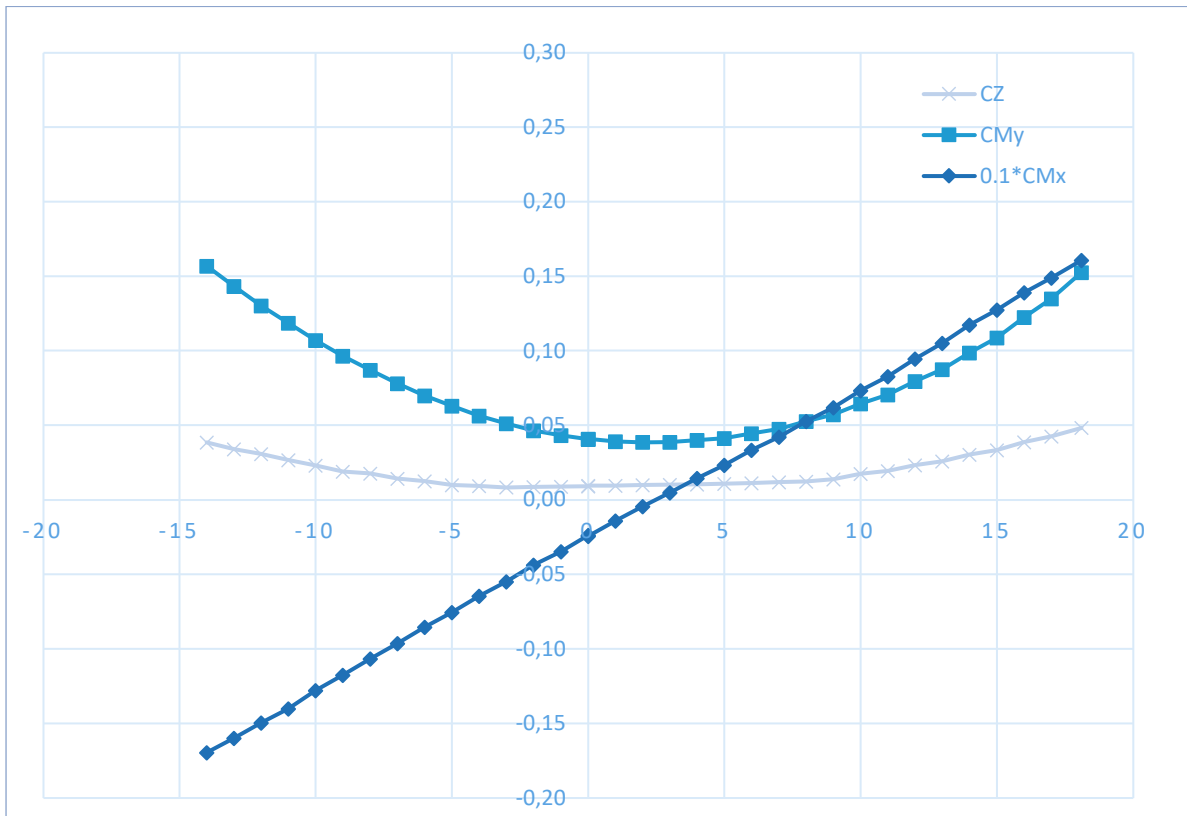
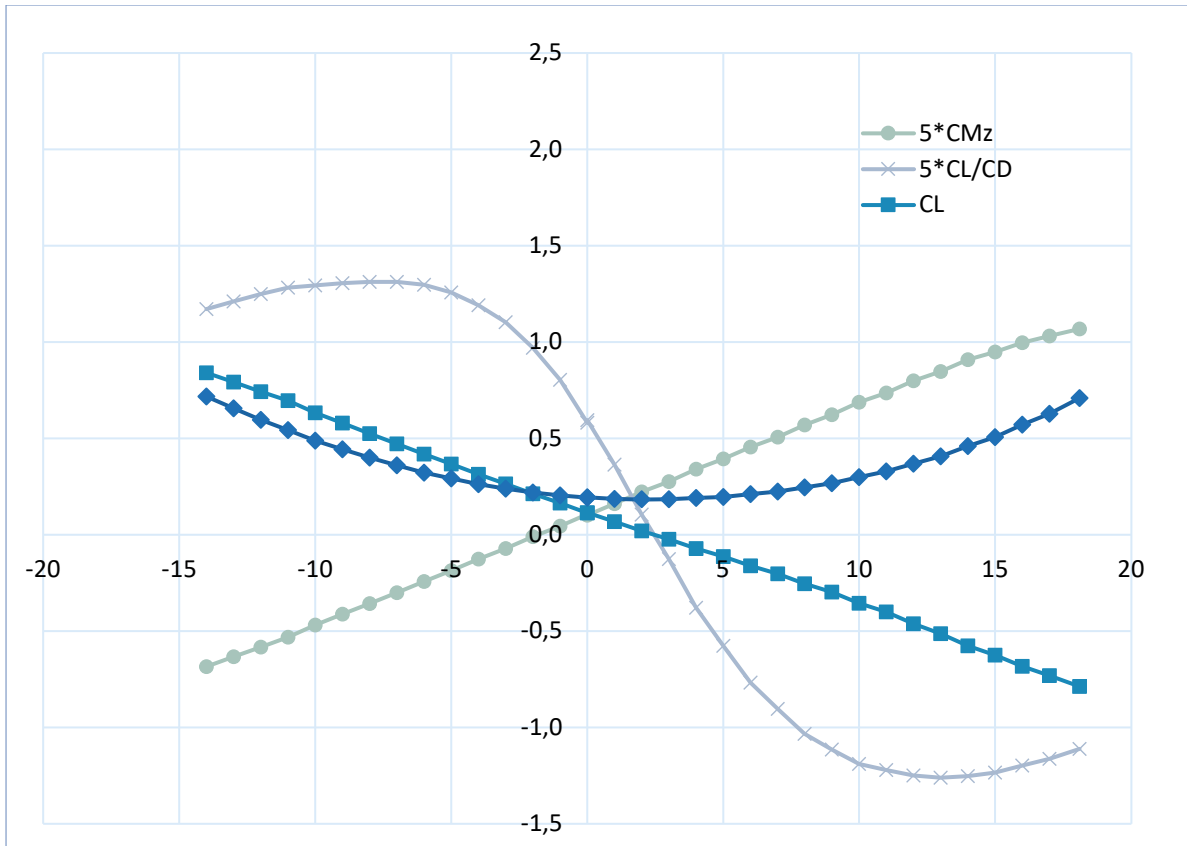


Figure 10: $R=0.5, U=7m/s, P_0=250kPa$

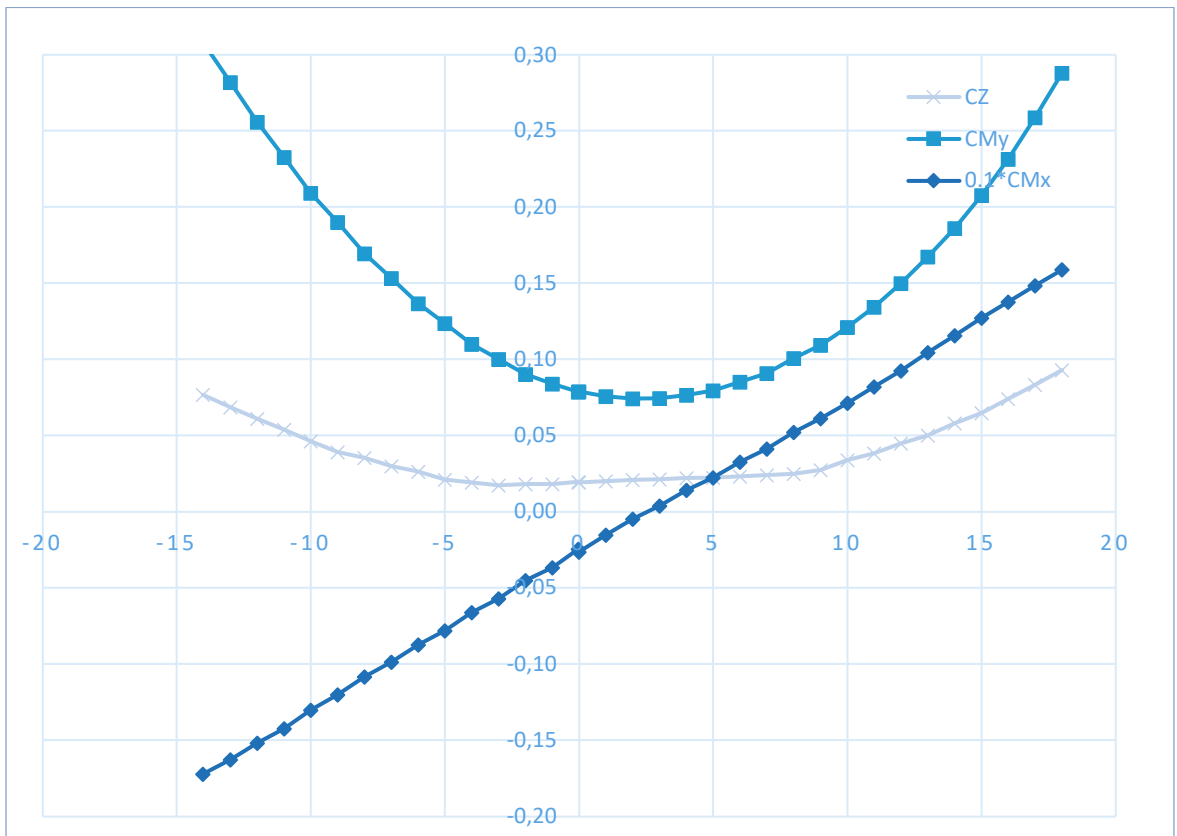
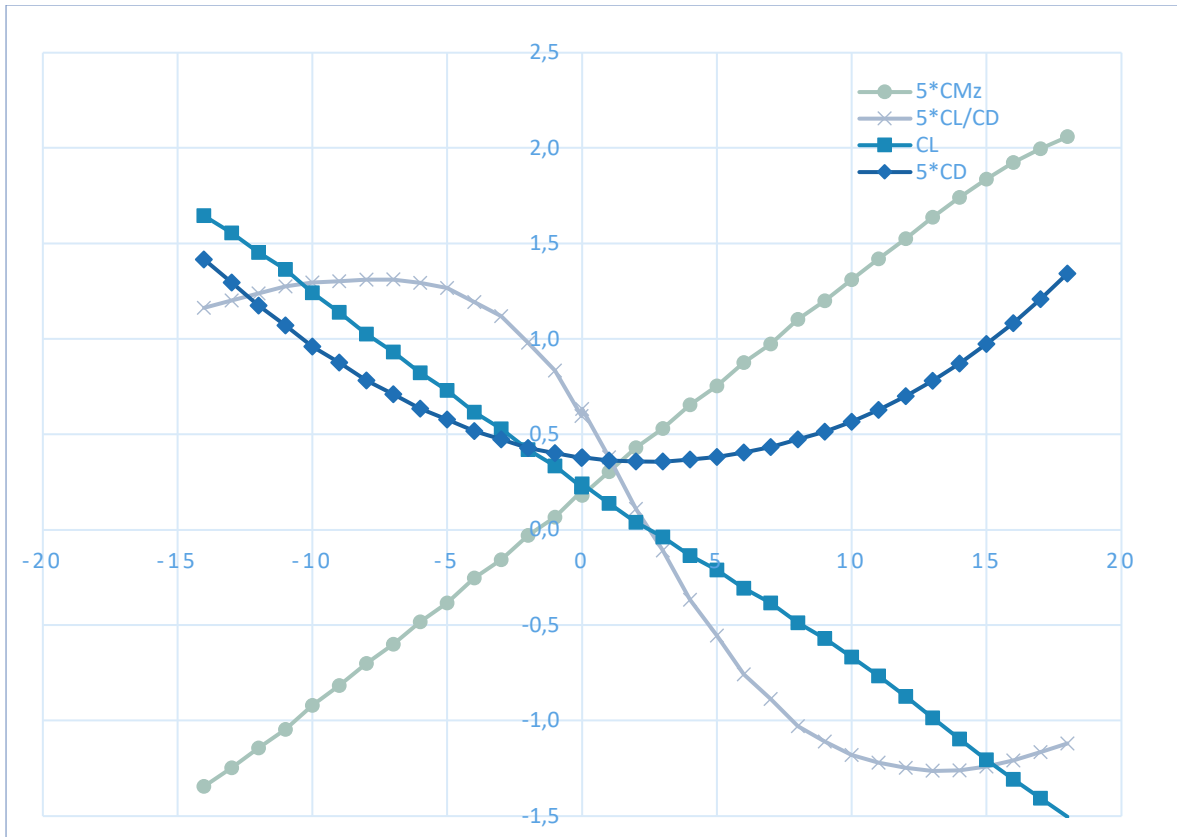


Figure 11: $R=0.5, U=7\text{m/s}, P_0=102\text{kPa}$

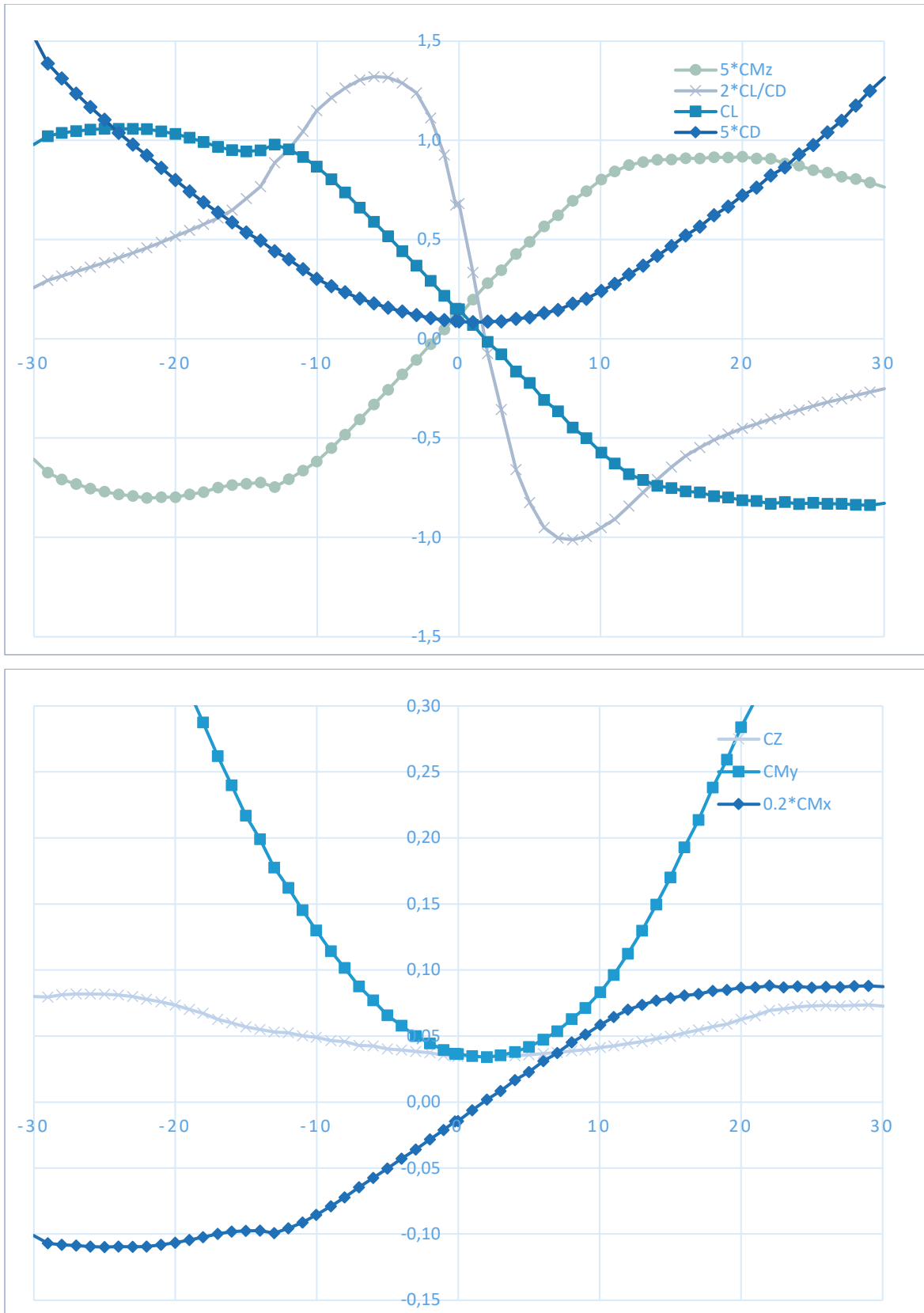


Figure 12: $R=0.8, U=5m/s, P_0=250kPa$

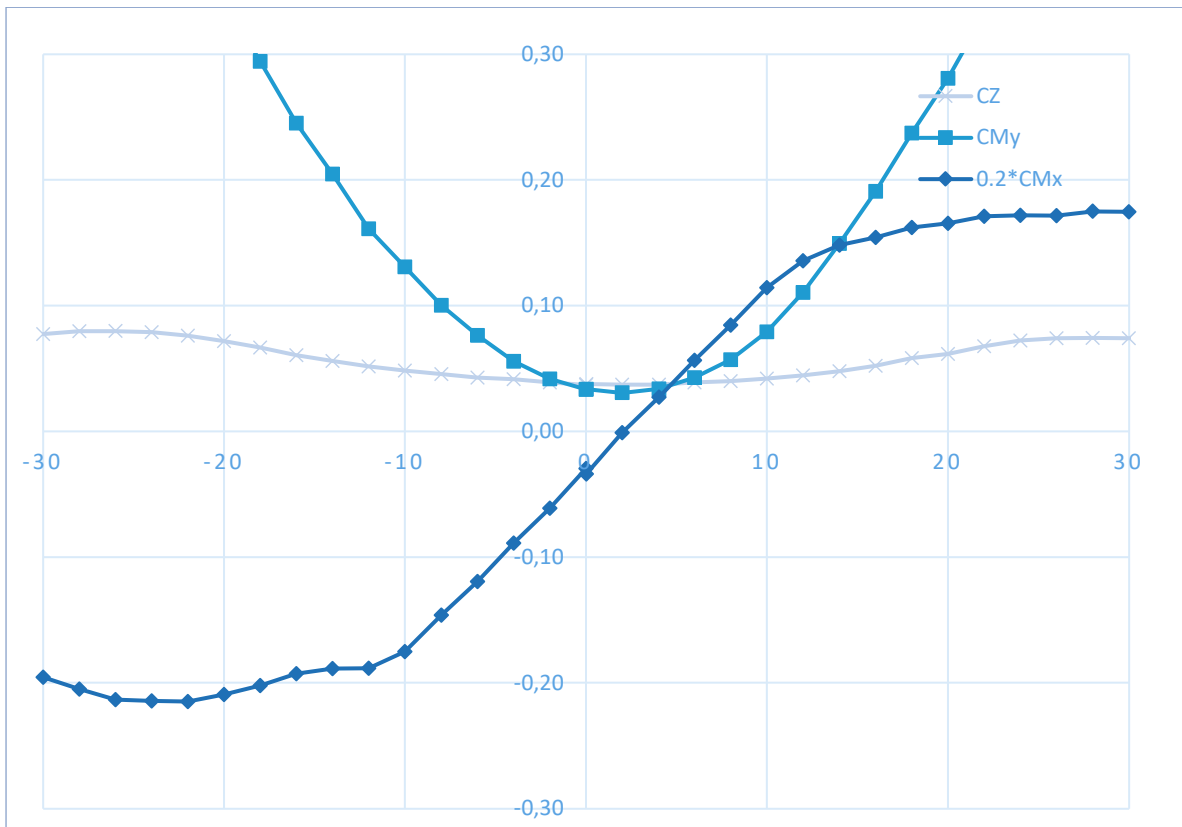
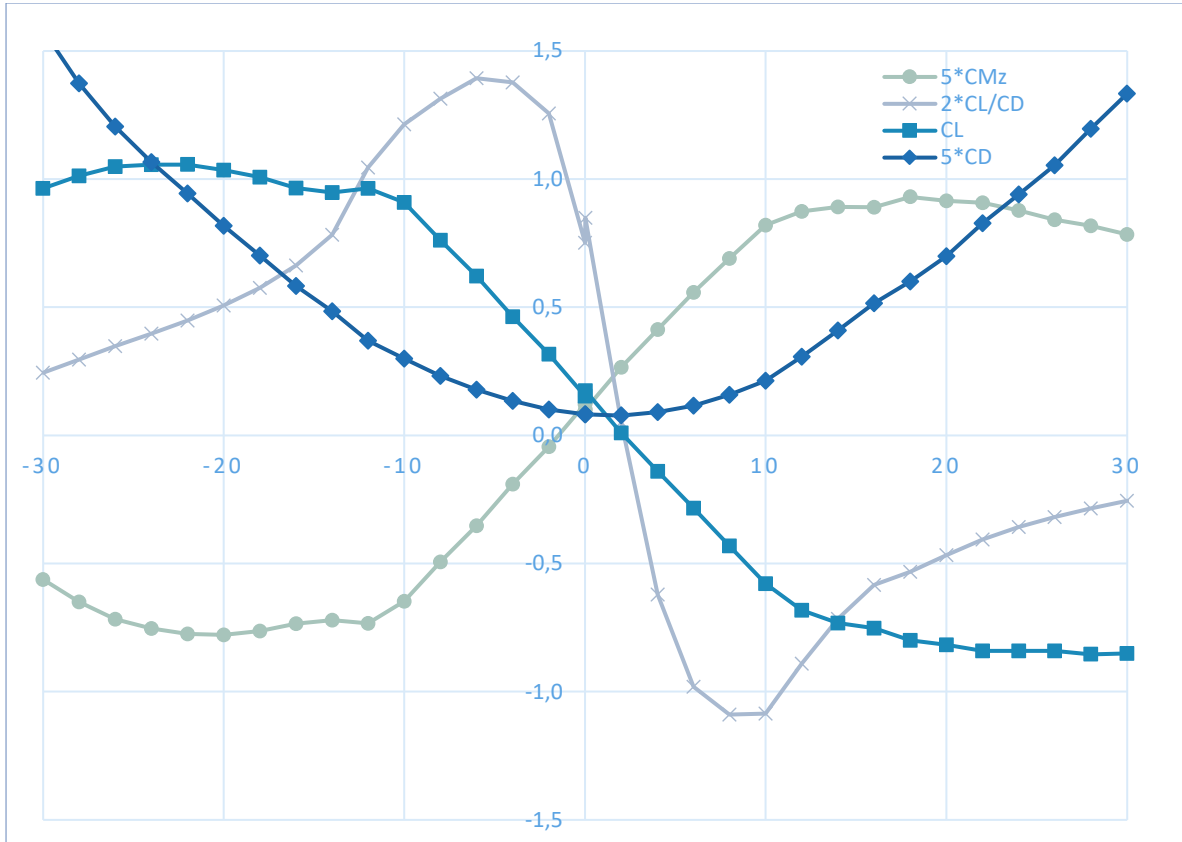


Figure 13: $R=0.8, U=7\text{m/s}, P_0=250\text{kPa}$

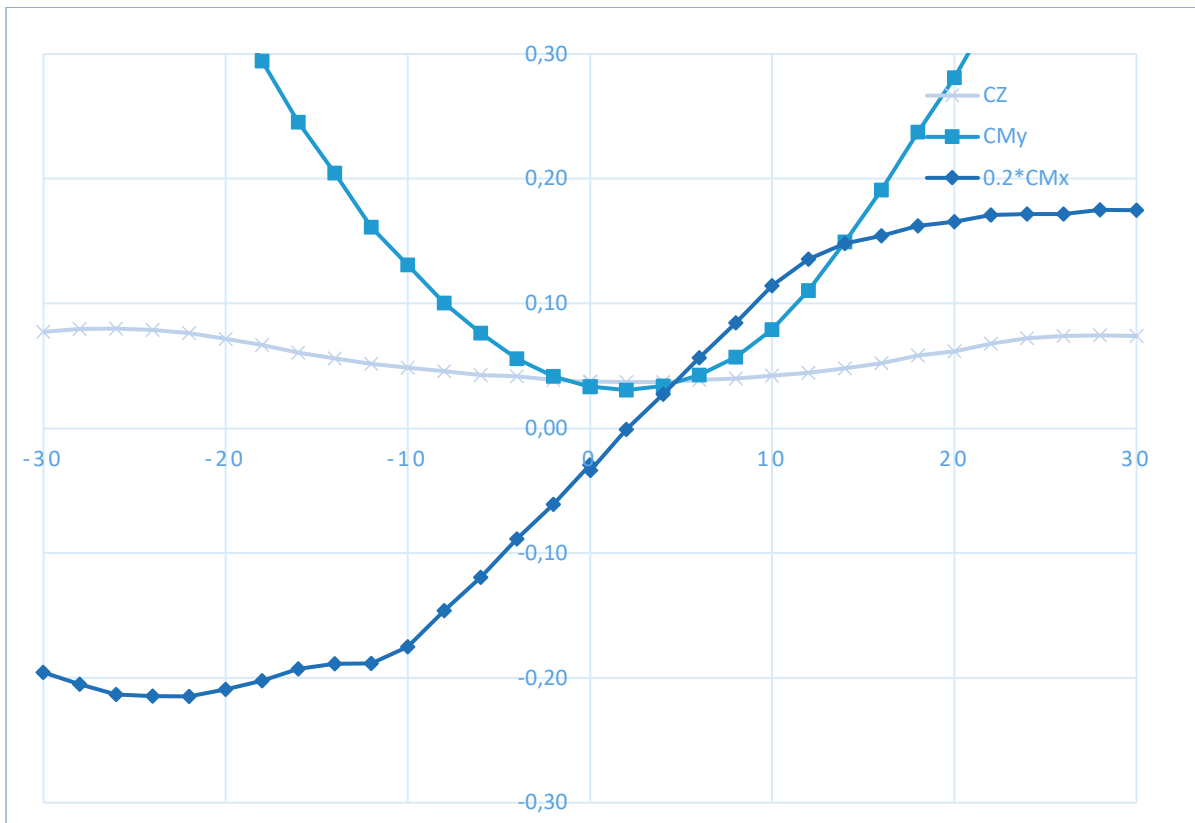
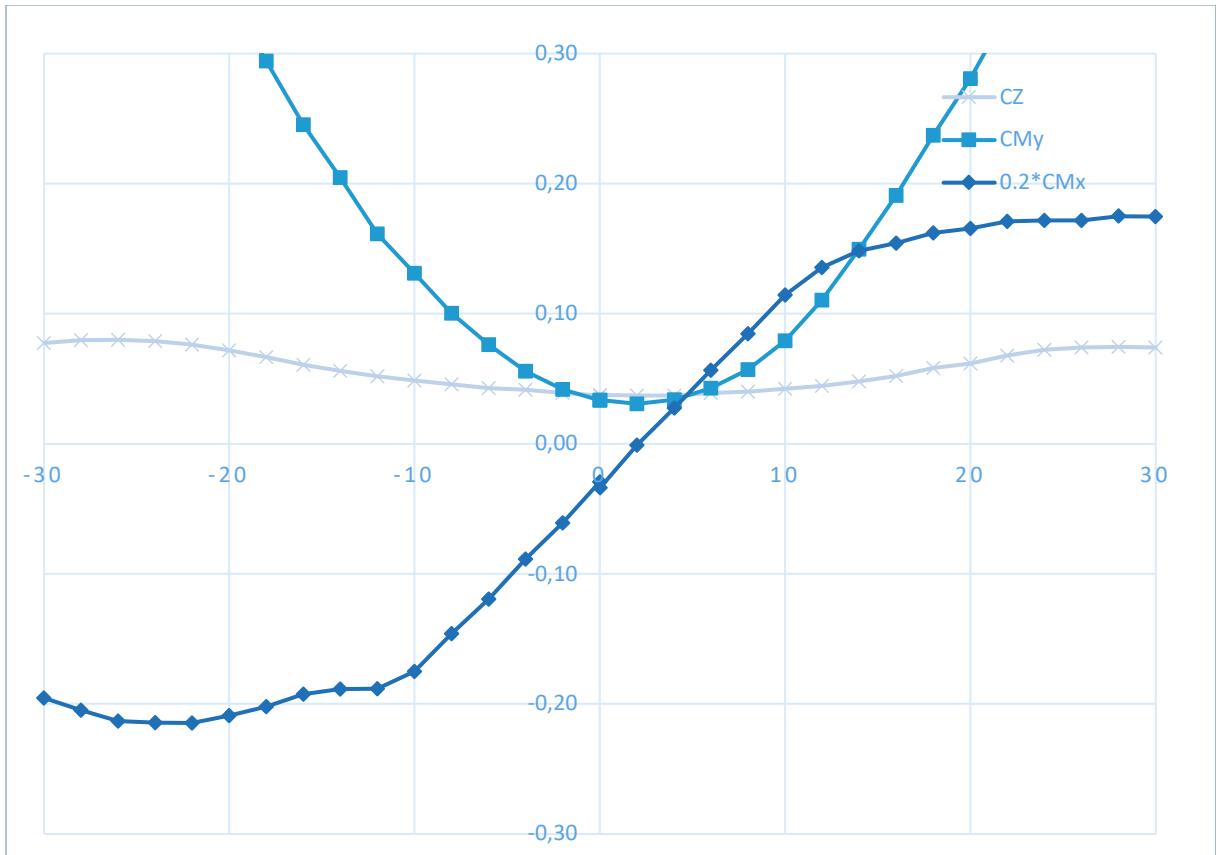


Figure 14: $R=0.8, U=7\text{m/s}, P_0=250\text{kPa}$

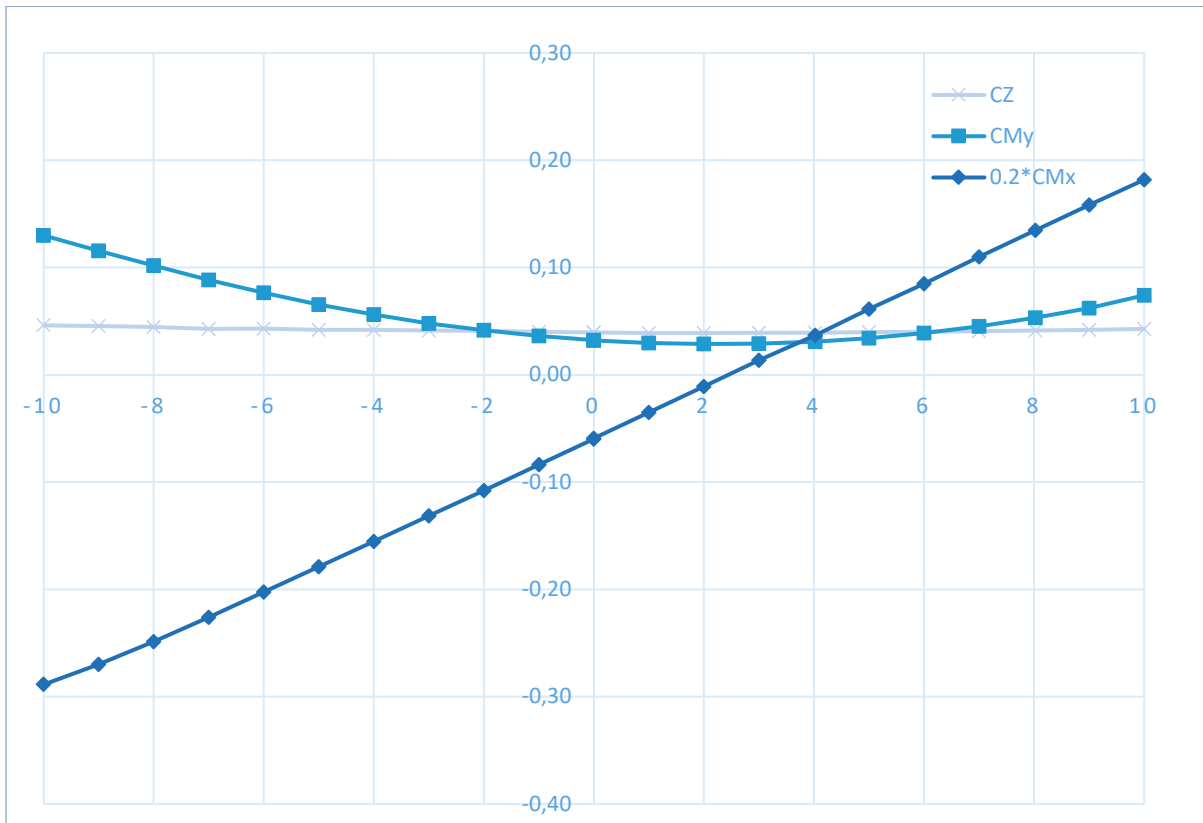
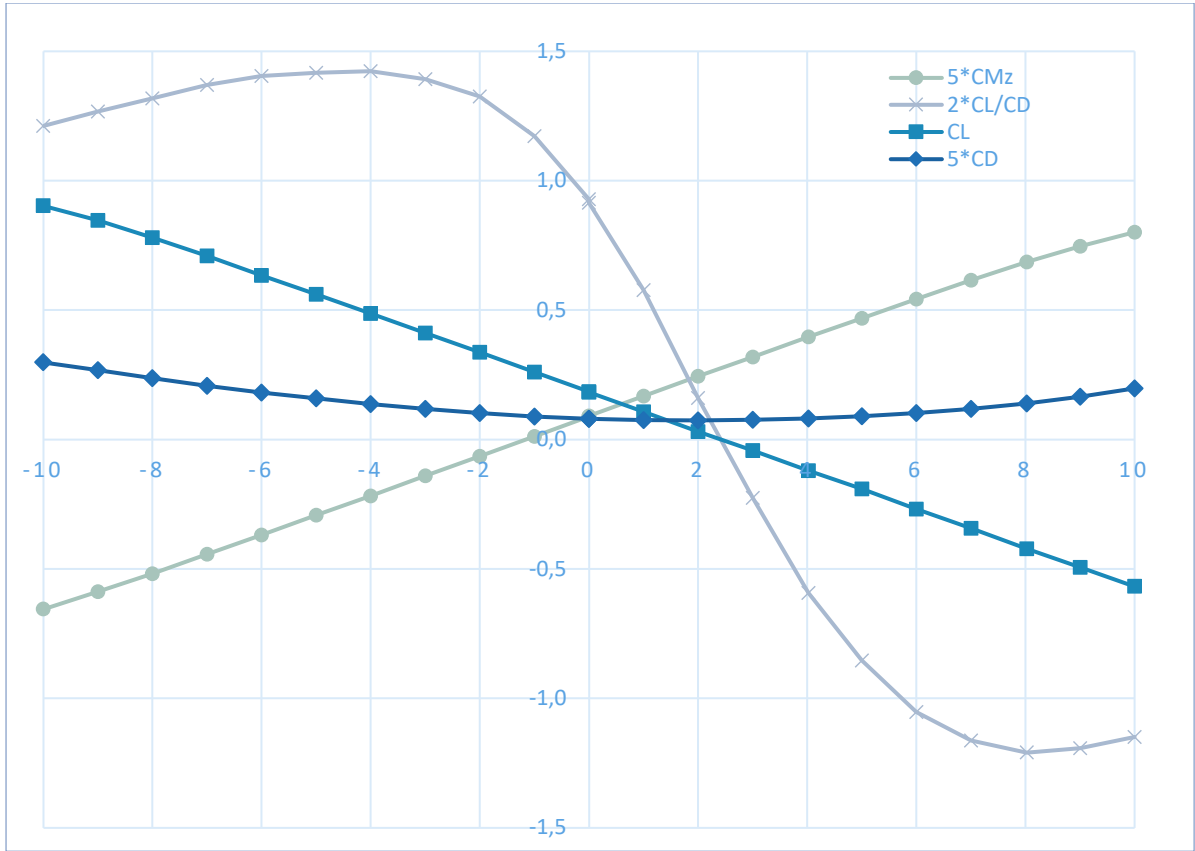


Figure 15: $R=0.8, U=9\text{m/s}, P_0=250\text{kPa}$

Rotating turbine

The blade design will be tested in SSPA's cavitation tunnel, shown in pictures below.

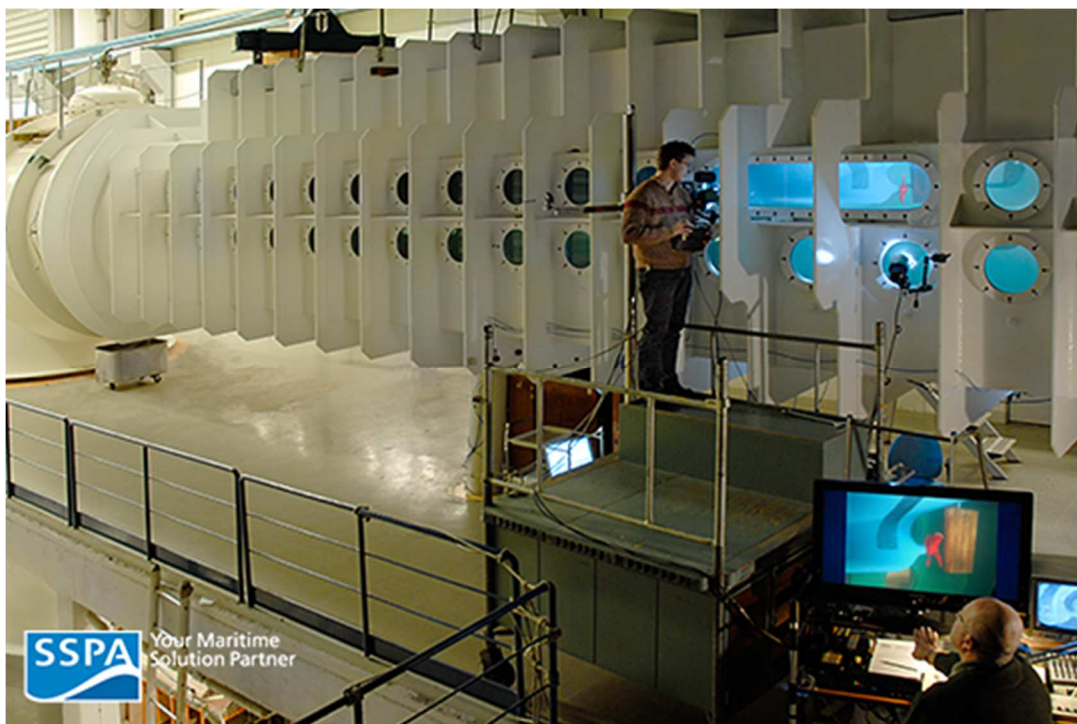


Figure 16: SSPA Cavitation Tunnel

The tunnel has three different measurement sections:

Tunnel section	1	2	3
Length, metres	2.5	9.6	8.0
Test section, m ²	diam 1 m	2.6 × 1.5	2.1 × 1.22
Max speed, m/sec	23	6.9	9.9
Min. cav number	0.06*	1.45**	0.30**

Table 1: Section dimension

Scale considerations

For scale effect reasons and because a larger blade is easier to build achieving sufficient stiffness the blades should be as large as possible. The the largest test section will be used, also because that section can maintain the lowest flow speed in the tunnel.

However, there are constraints on size of blades other than the obvious geometrical constraints imposed by the tunnel cross section dimensions of 2.6m x 1.5m. As a rule of thumb no more than 2% of the cross sectional area should be obstructed for reasons of blockage effect and interaction with the wall of the tunnel, which would allow a turbine diameter of no more than 0.31m, illustrated by the table below. Therefore, we have to allow a little more blockage than normally with a maximum diameter around 0.5m, ie. a scale factor of 38 (with a fullscale diameter of 19m), with a blockage of 5%.

Scale	D	Area turb	Area Cav	Blockage
15	1.27	1.26	3.9	32%
20	0.95	0.71	3.9	18%
25	0.76	0.45	3.9	12%
30	0.63	0.32	3.9	8%
35	0.54	0.23	3.9	6%
40	0.48	0.18	3.9	5%
45	0.42	0.14	3.9	4%
50	0.38	0.11	3.9	3%
55	0.35	0.09	3.9	2%
60	0.32	0.08	3.9	2%
65	0.29	0.07	3.9	2%

Table 2: Blockage as a function of scale

Regarding flow speed and RPM for the tests, the following are the design specifications

	Range	Nominal
Diameter (m)	19 to 21.5	21.5
RPM	12 to 18	15.3
Current speed (m/s)	1.7 to 3	2.7
Depth of turbine center (m)		16

Table 3: Full scale design specifications

The main parameter to match is the advance ratio of the blades, defined by

$$J = \frac{V_a}{nD}$$

where V_a is the free stream velocity (i.e. current speed in full scale and flow speed in tunnel at model scale), n is RPS and D is turbine diameter. For the range of RPM in fullscale this amounts to advance ratios as a function of V_A as below

RPM	12	15.3	18
VA	J	J	J
1.7	0.395	0.310	0.264
2	0.465	0.365	0.310
2.3	0.535	0.420	0.357
2.6	0.605	0.474	0.403
2.9	0.674	0.529	0.450
3.2	0.744	0.584	0.496

Table 4: Advance ration as function of free stream velocity and RPM (full scale)

To get the same advance ratio in model scale as for full scale the fullscale advance ratio can be used to find the model scale RPS as $n = \frac{V_a}{JD}$ as below, where RPM is rounds pr minute in full scale and RPS is rounds per second in model scale, and V_A is the current speed for full scale diameter of 0.5m. The tunnel speed below is kept constant, only the RPS is changed to achieve the same advance ratio as for full scale.

RPM(full)	12.24	15.3	18.36
VA	RPS(model)	RPS(model)	RPS(model)
1.7	12.90	16.13	19.35
2	10.97	13.71	16.45
2.3	9.53	11.92	14.30
2.6	8.43	10.54	12.65
2.9	7.56	9.45	11.34
3.2	6.85	8.57	10.28

Table 5: RPS with same advance ratio as in full scale

The cavitation number defined as

$$\sigma = (p_r - p_v) \left(\frac{1}{2} \rho V^2 \right)$$

where p_r is the reference pressure and p_v is the vapor pressure (1.7kPa at 15 degrees). In full scale with a the static pressure at 16m's depth the cavitation number will be

VA	sigma
1.7	175.9
2	127.1
2.3	96.1
2.6	75.2
2.9	60.4
3.2	49.6

Table 6: Full scale cavitation number

The corresponding necessary pressure at model scale with a flow velocity in the tunnel at 2.5m/s (the minimum flow speed for this section is 1.5m/s, but its where difficult to maintain, therefore SSPA prefers to run minimum 2.5m/s flow speed).

max P0	200000
VA	P0 (Pa)
1.7	551291
2	398779
2.3	301949
2.6	236658
2.9	190561
3.2	156809

Table 7: Model scale cavitation number

The above pressure is necessary overpressure in the cavitation tunnel to achieve the same cavitation number as for full scale. The maximum attainable overpressure in the tunnel is 200kPa, for which reason we cannot obtain the pressure needed for the lower current velocities, on for the higher range. A little more tweaking with the numbers, especially going a little lower in tunnel flow speed would improve this, but as stated going to lower flow speeds creates its own set of issues.

To conclude, the above setup of flow speed, RPM and pressure seems to be the best option. Moving the numbers slightly for better cavitation number similarity, does not change the conclusion of the scale aiming for a turbine with a diameter 0.5m.

Model setup

For RPM control, pitch control and torque/thrust measurements, SSPA needs to install a gondola suspended from the cavitation tunnel ceiling by a sword. To fit electric motor (for RPM control and RPM measurement) and thrust and torque measurement device in the gondola the gondola will have length of 1.2m and a diameter of 0.2m. With a scale factor of 38, the full scale diameter would be 8m, which is much larger than the full scale diameter. To reach the full scale hub diameter an attachment upstream of the gondola will be build extending the drive axel.

Design

The following aspects must accommodate in the model:

- Manual or automatic pitch control (+/- 20degrees)
- Blades from CANOE must be interchangeable on hub
- Scale: 1:38
- RPS (in model scale) is in the range from 8-15, with a flow speed of 2.5m/s
- Pitch angle +/- 20degrees, manual setting.
- Nacelle should be same geometry as full scale
- Nacelle and blades must be able to rotate relative to the free stream direction (ie. sword must be able to rotate)
- Torque and thrust must be measured
- Electrical engine must drive shaft to be able to control RPM

To accomplish the above the following hub design have been chosen (see Figure 17). The hub will be manufactured in brass. Interlocking the blades in the hub after assembly. The (with a diameter of 5cm in model scale) is too small to allow for motorized pitch control. Therefore manual pitch control will be used (ie. each blade is rotated manually relative to an etched angle indication on the hub).

The hub design is a copy of the fullscale design (see Figure 17, with the only major difference being bolts attaching the blades to the hub in full scale. These will not be included in model scale.

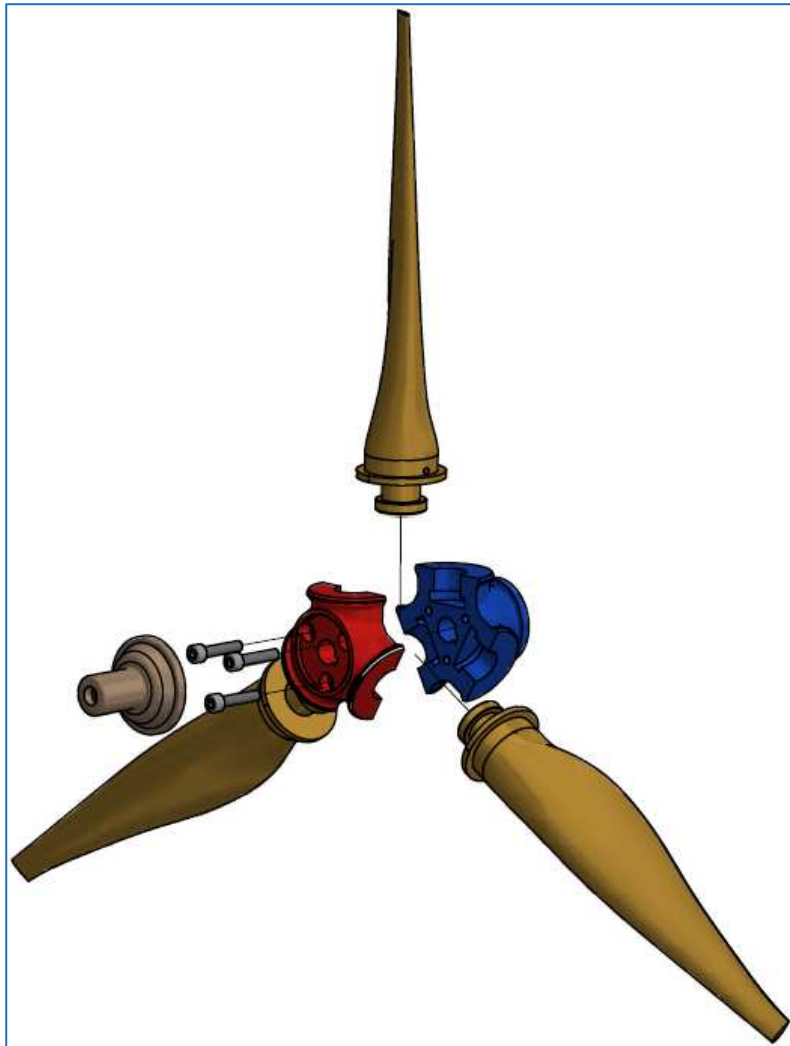


Figure 17: Hub assembly

The Nacelle and sword will be reproduced to the exact fullscale geometry. A drive motor and torque/thrust assembly will be used to control axel rotational speed and measurements. From left to right in Figure 18 the hub can be seen (without blades), gondola geometry with shaft inside, dynamometer (dark grey) and finally electrical engine (cyan).

The entire drive unit is attached to the roof of the cavitation tunnel section by two struts, the first being a copy of the Magellans turbine sword, and the aft for structural rigidity. Both struts rotate around a plywood disc (see Figure 19) to a rotation table above the cavitation tunnel section to simulate oblique angles of flow (yaw angle). As the center of rotation is not at the hub, translation of the hub to either side occurs when yawed, however it is possible to move the entire rotation table to keep the hub centered in the cavitation tunnel.

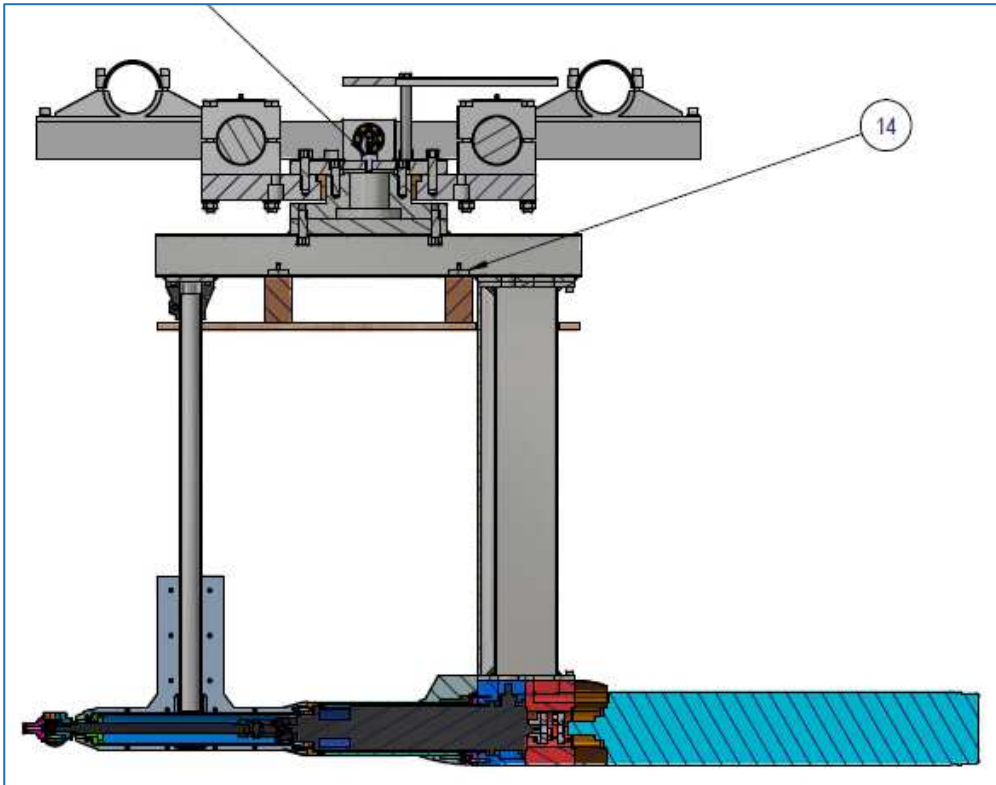


Figure 18: Assembly of model, side view

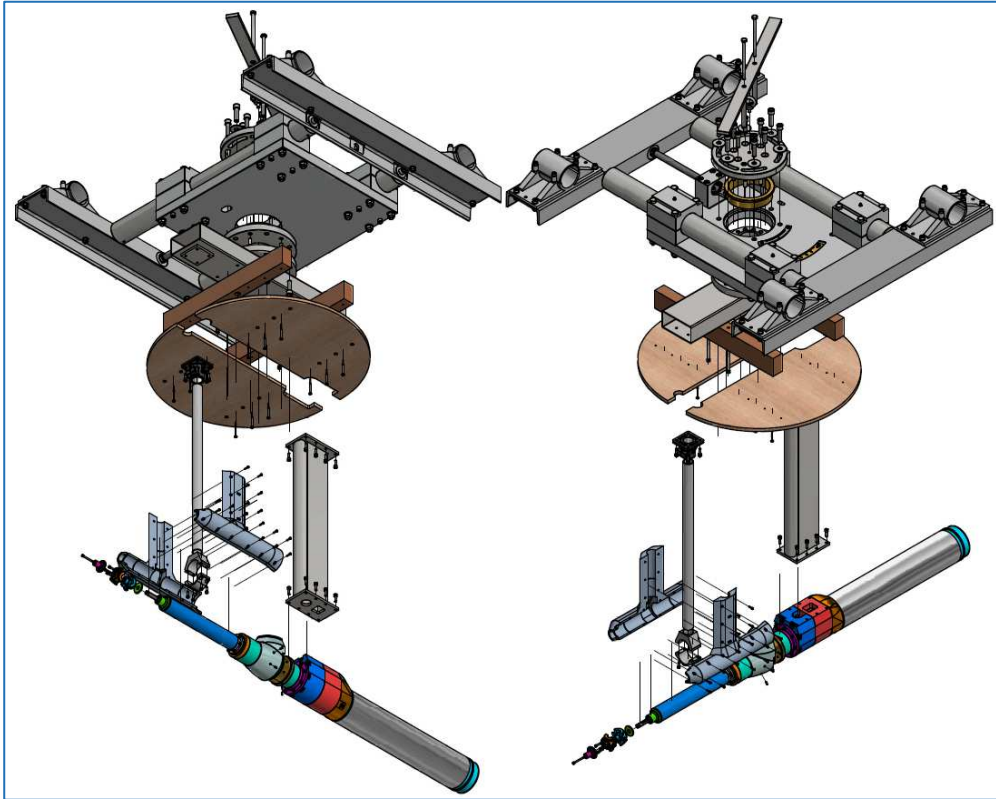


Figure 19: Entire construction

The test section (section 2) has the following dimensions (and a width of 2.6m) as shown in Figure 20. The reason for using section 2 (the largest section) are twofold. First of all using the largest section will allow the smallest scale factor, ie. largest blades without increasing the blockage too much. Secondly, the cavitation tunnel has a minimum allowable flow speed, as the impeller driving the flow is water cooled and lubricated by the water flow in the tunnel. Using a smaller section would require a too high minimum flow velocity attain the advance ratios necessary to simulate the full scale turbine's operating conditions. The turbine is placed in the aft part of the section (flow is moving from left to right in Figure 20), as flow is more uniform in this part of the section.

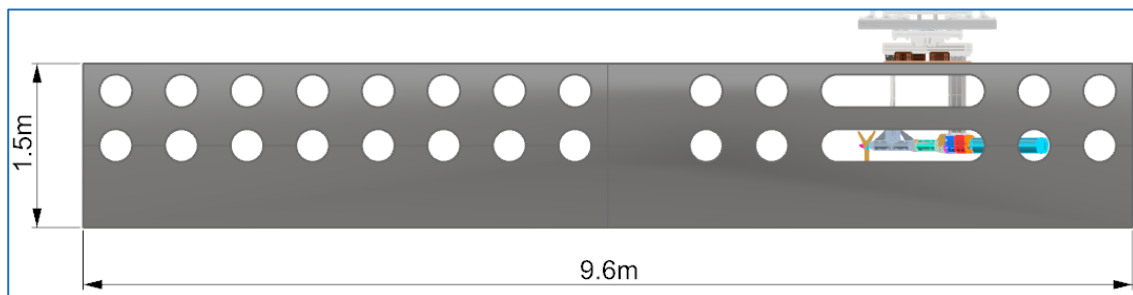


Figure 20: Side view of cavitation tunnel section 2 including turbine model

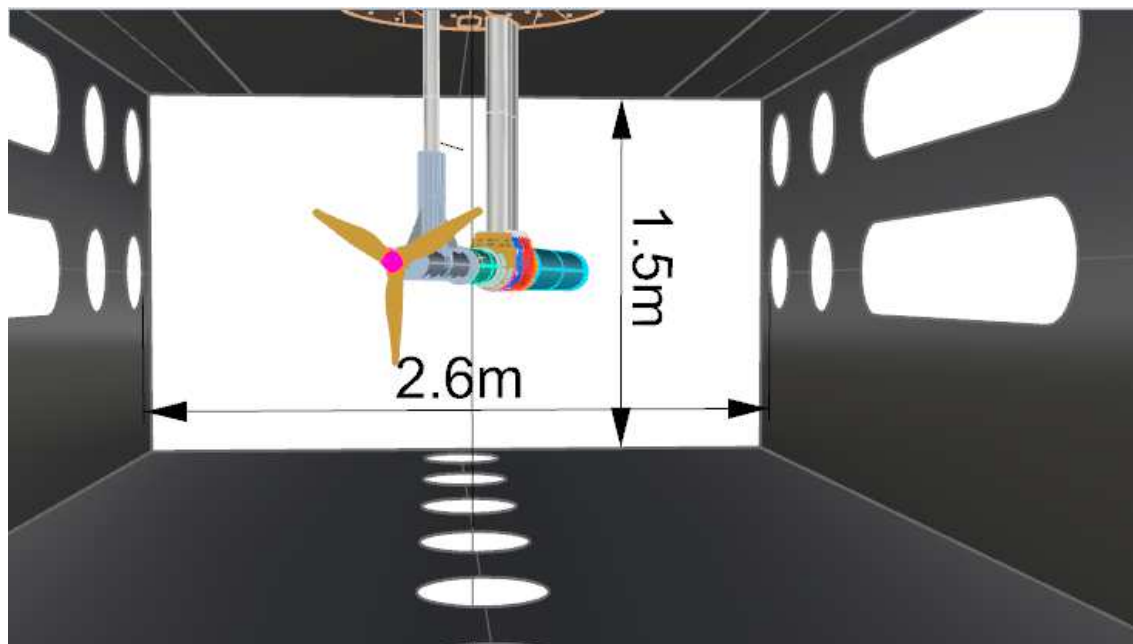


Figure 21: Turbine assembly inside cavitation tunnel at 20degrees yaw angle

Figure 21 shows the dimensions of the turbine in the tunnel section. Distance to roof/floor of section is 0.5m in either direction, and 1.05m to either side depending on the center of the hub (changing with yaw angle of turbine).

Results

All tests are run at a cavitation tunnel flow speed of 2.5m/s. To test a range of advance ratios or tip speed ratio, the speed of revolutions are changes. The ranges tested are N (rps) between 7-17 1/s. Where

RPM: Revolutions pr Minute

N: Revolutions pr second

T: Thust [N]

Q: Torque [Nm]

P₀: Static cavitation tunnel pressure [kPa]

λ: Tip Speed Ratio ($\pi \cdot N \cdot D/V$)

J: Advance ratio ($\frac{V}{D \cdot N}$)

σ: Cavitation number

D: Turbine diameter

V: Flow speed

α: Blade pitch Angle

β: Yaw angle

C_P: $C_P = \frac{P}{\frac{1}{2}\rho\pi R^2 V^3}$ where $\rho = \frac{1000kg}{m^3}$ and $R = 0.25m$

P = $2\pi NQ$

C_T: $C_T = \frac{T}{\frac{1}{2}\rho\pi R^2 V^2}$

All tests are run at a cavitation tunnel flow speed of 2.5m/s. To test a range of advance ratios or tip speed ratio, the speed of revolutions are changes. The ranges tested are N (rps) between 7-17 1/s.

Blade pitch angles are tested between 0 to 12degrees, where 0 degrees refers to the original optimum pitch angle from Magellans. The reference is 20.79degrees from vertical using the blade tip direction between suction and pressure side of the blade defined in the CAD model of the blade, see Figure 22. In summary, the range of test parameters are as follows

Yaw: 0-19.5° (0, 7, 13 and 19.5)

Pitch: 0-18° (0, 4, 8, 12 and 18)

V: 2.5m/s

P: P_{atm}, P=250kPa, P=38kPA

Not all combination are tested. As the tests have shown some influence of cavitation most tests are completed at over pressure corresponding to the full scale hydrostatic pressure. Only one test was completed with 18° pitch angle.

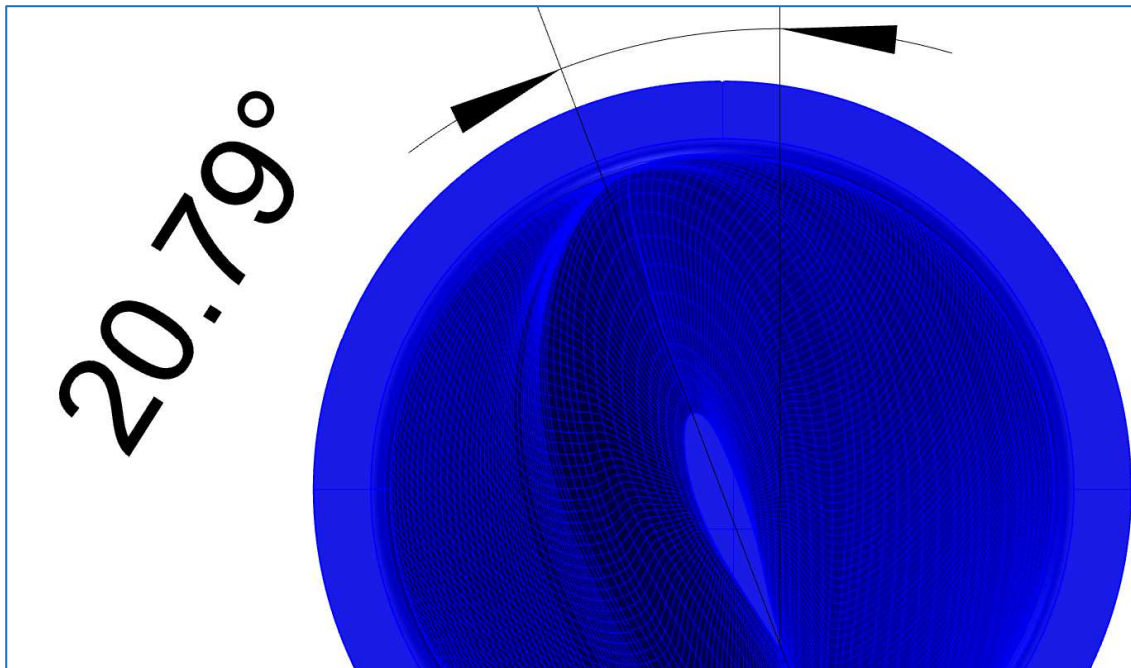


Figure 22: Reference pitch angle

The following test matrix have been completed completed, tests marked in yellow have been completed at the time of delivering this report.

Table 8: Test matrix for original blade geometry

Serie	Test	α	β	P_0	Comment
5	3	0	0	Atm,220	
6	1	4	0	220	
7	1	8	0	220	
4	1	12	0	Atm,220	
7	2	8	7	220	
5	2	18	7	Atm	
4	4	12	7	Atm	
		4	13	220	
7	3	8	13	220	
4	4	12	13	Atm	
7	4	8	19.5	220	
4	2	12	19.5	Atm	Only angle of attack, no translation
4	3	12	19.5	Atm	Angle of attack and crossstream translation to have hub in same position

Comparison between SSPA bronze and CANOE carbon fibre blades

The two sets of blades are shown in Figure 23



Figure 23: CANOE carbon fibre and SSPA bronze blade, original geometry

Both the SSPA bronze blades and CANOE carbon fibre blades were run at 12° pitch angle at 0° yaw. The resulting Thrust (T) and Torque (Q) measurements is shown Figure 24 and Figure 25.

The difference is quite high, at points up to 20% in thrust. The carbon fibre blades have been coated at polished to create a smooth surface, however this procedure and the underlying manufacture method have probably created blades which does not meet necessary geometrical tolerances to produce blades which meets necessary tolerances to be comparable to CNC milled bronze blades. While balancing the CANOE blades a thickness difference of 0.6mm were measured.

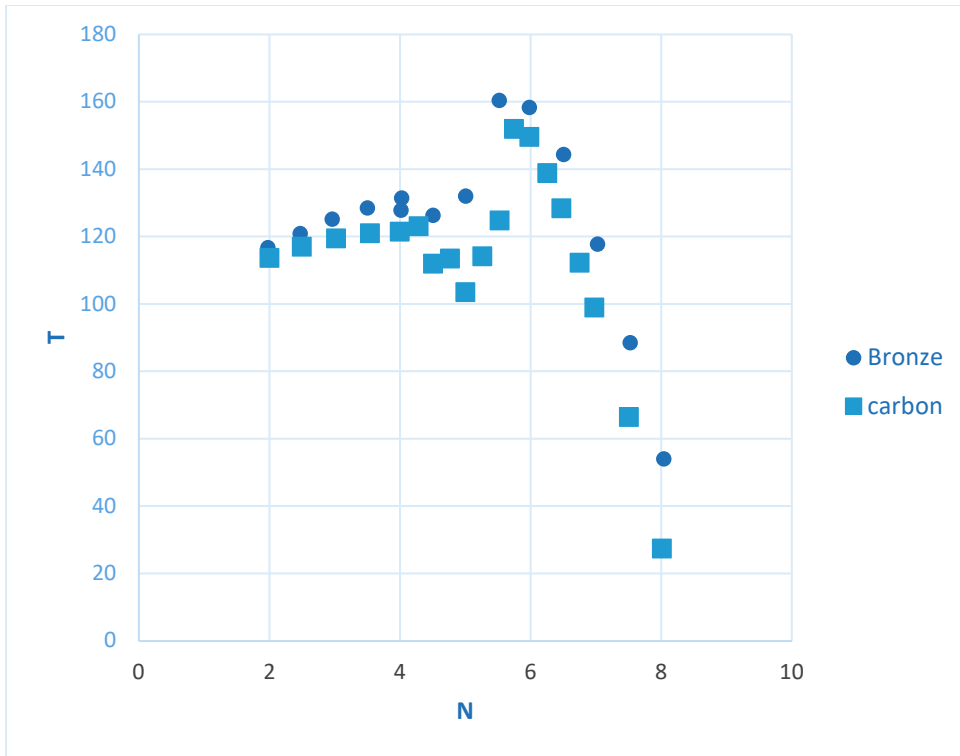


Figure 24: Thrust comparison between carbon and bronze blades

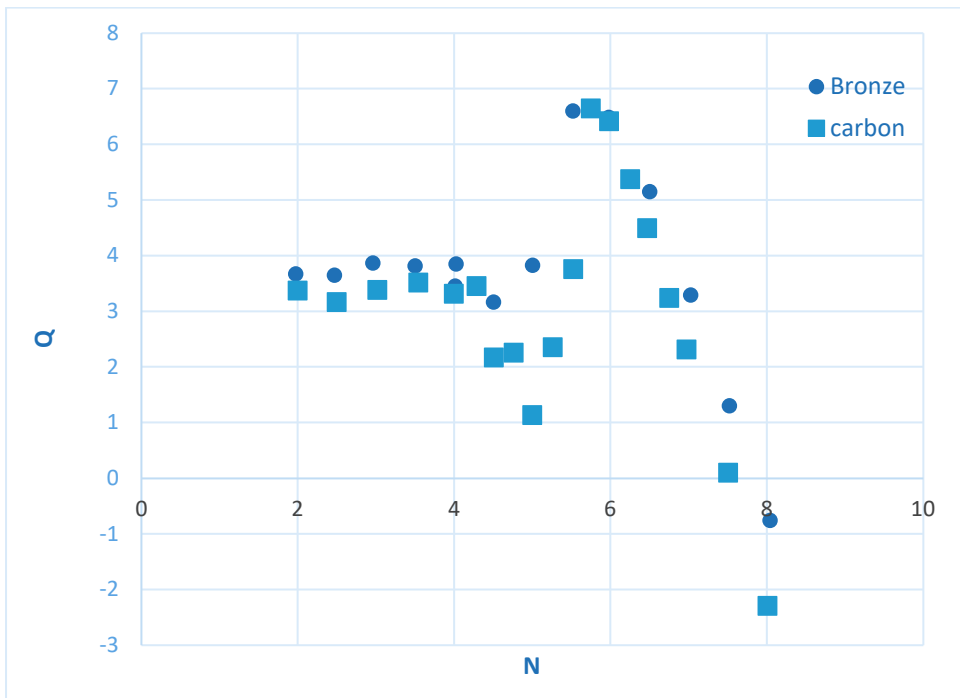


Figure 25: Thrust comparison between carbon and bronze blades

As the carbon blades does not produce the same results as the bronze blades, it was decided to complete measurements on the bronze blades. SSPA have build several thousand propeller blades during the years, and we are therefore confident in our tolerances.

Influence of cavitation and translation due to yaw

Initial measurements were for quite high pitch angles (+12 degrees) and showed no cavitation influence on, see Figure 26. However, tests at a later stage chronologically at 0° degrees pitch angle showed influence of cavitation both visually and in the measurement data, see Figure 27. This is the case at high tip speed ratio, but less so closer to maximum C_p and beyond stall angle. As the initial results showed no influence of cavitation, the pressure for the first tests were at atmospheric pressure (until series 5, test 3) and the remaining tests were completed at overpressure which is the actual hydrostatic full condition for the turbine.

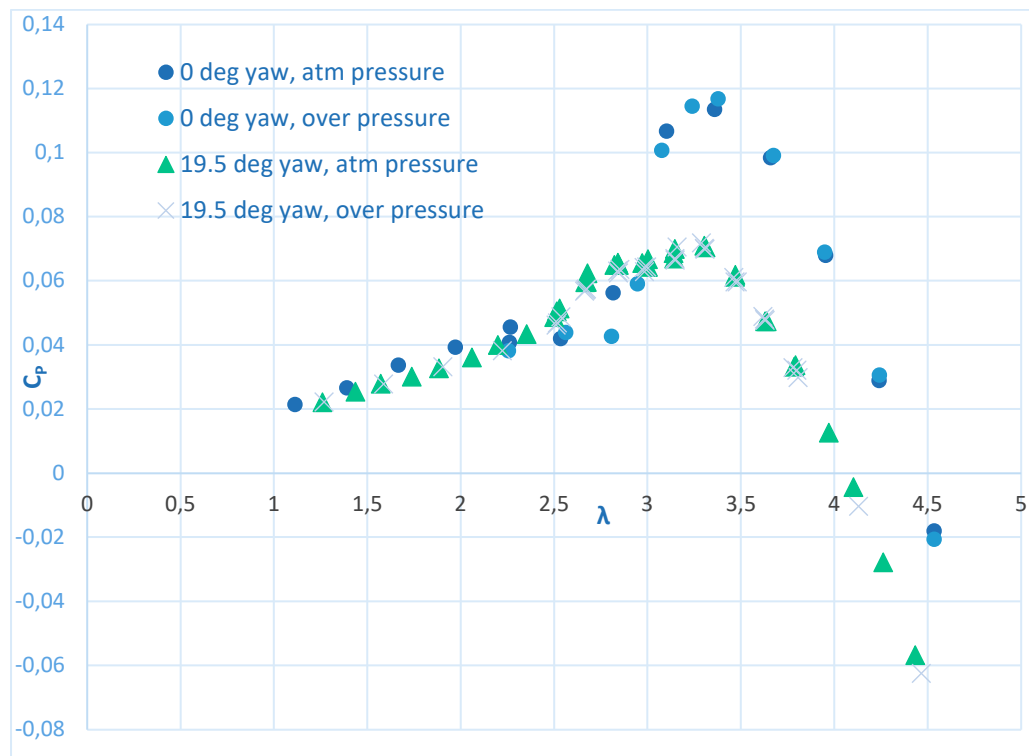


Figure 26: C_p at atmospheric and over pressure (220kPa) at 0° and 19.5° yaw angle, 12° pitch

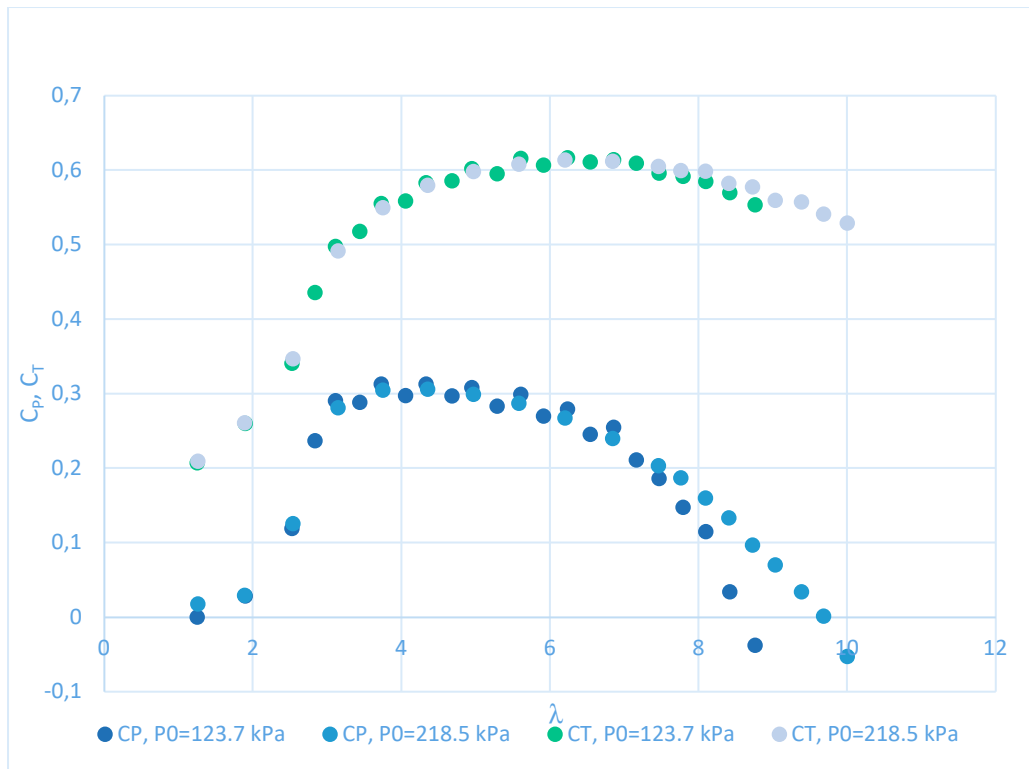


Figure 27: Atmospheric and over pressure (220kPa) at 0° yaw angle, 0° pitch

As the center of the hub is translated when the turbine is yawed, it was investigated if this affects the C_p values by measuring C_p at 19.5 yaw angle with only yaw and comparing to the same yaw with the hub recentered (translated 20cm back). From Figure 28 it can be seen that the C_p values are almost identical. Therefore within yaw angles 0-20 degrees the turbine will not be recentered.

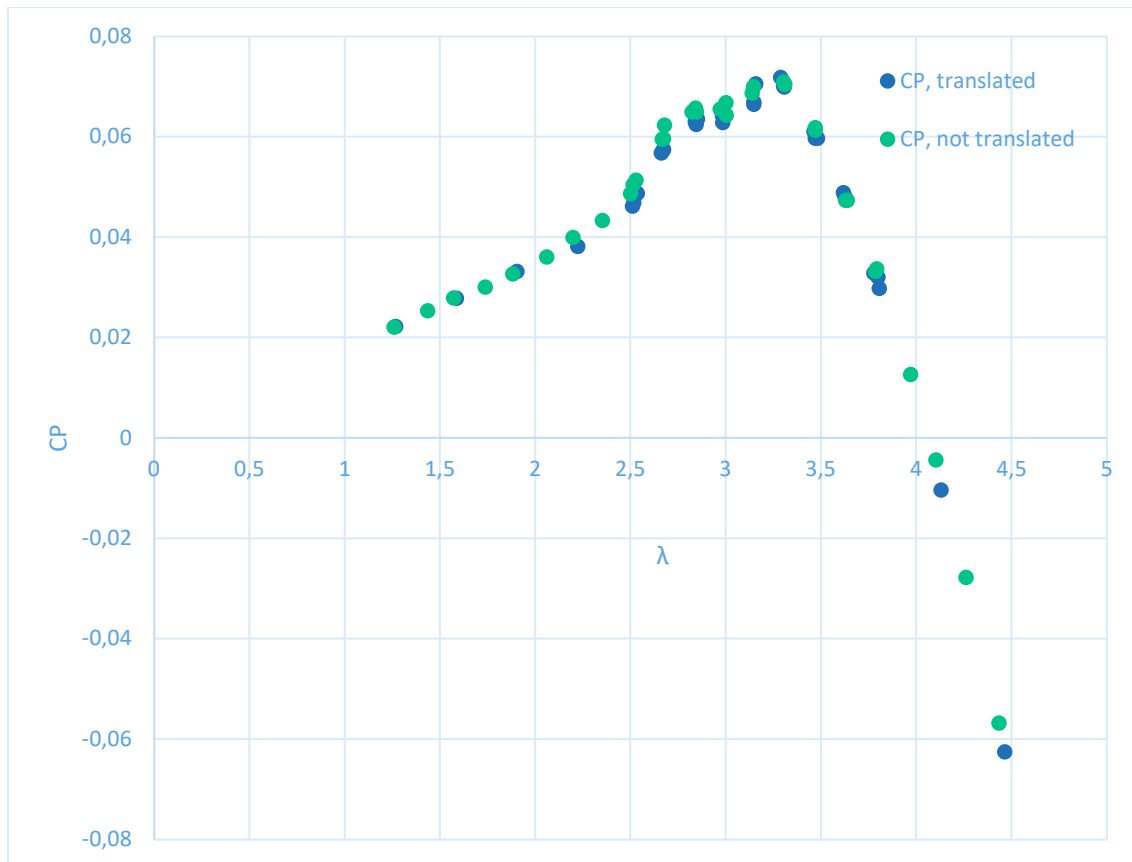


Figure 28: Translation of turbine compared to no translation

Results

The following figures show the results according to the test matrix,

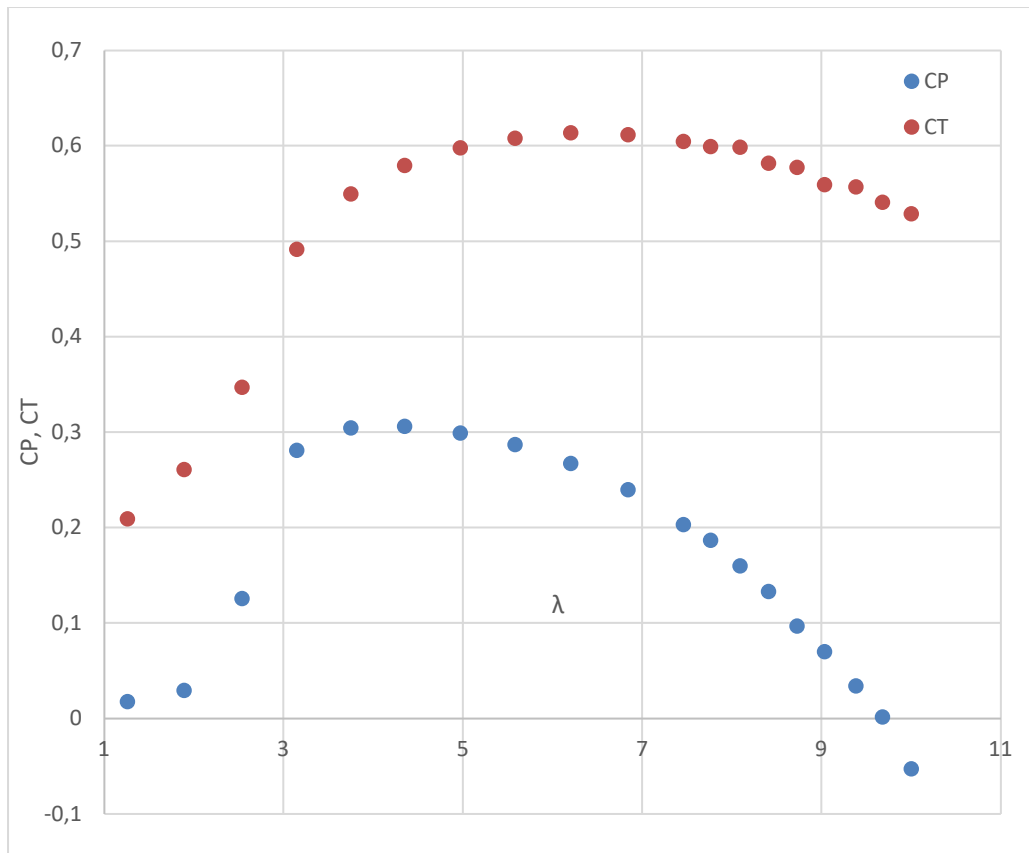


Figure 29: $\alpha = 0$, $\beta = 0$, $P_0 = 220 \text{ kPa}$

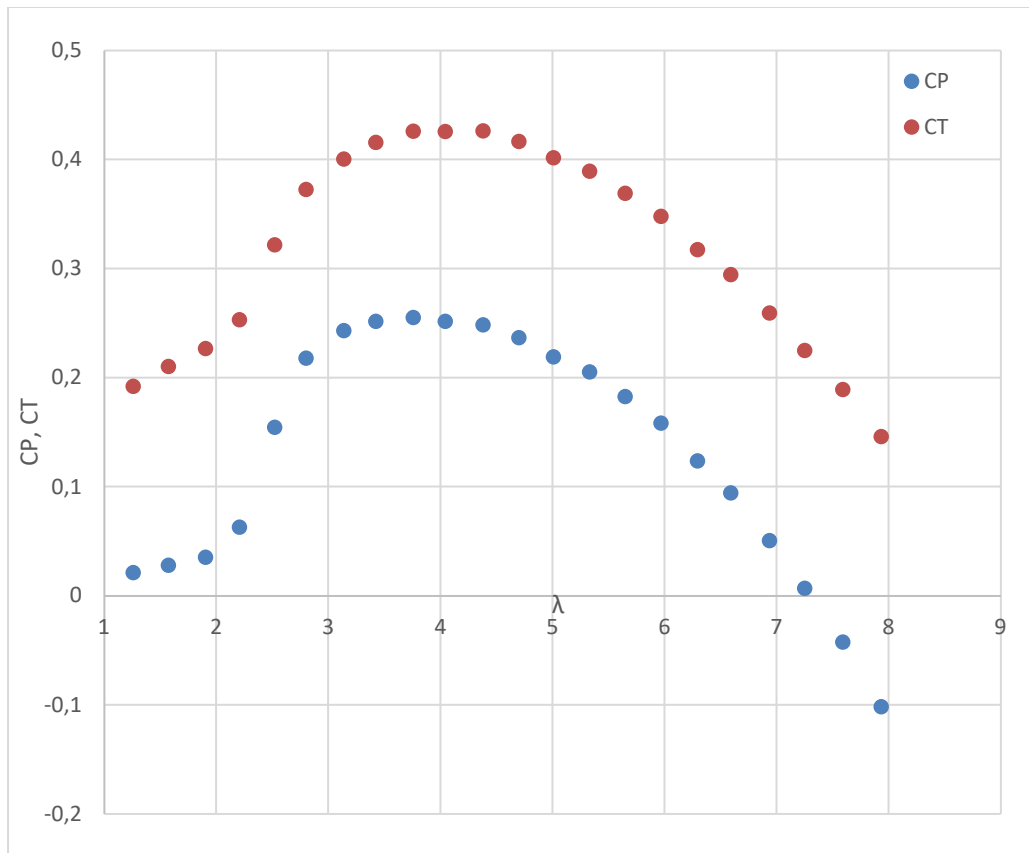


Figure 30: $\alpha=4$, $\beta=0$, $P_0=220kPa$

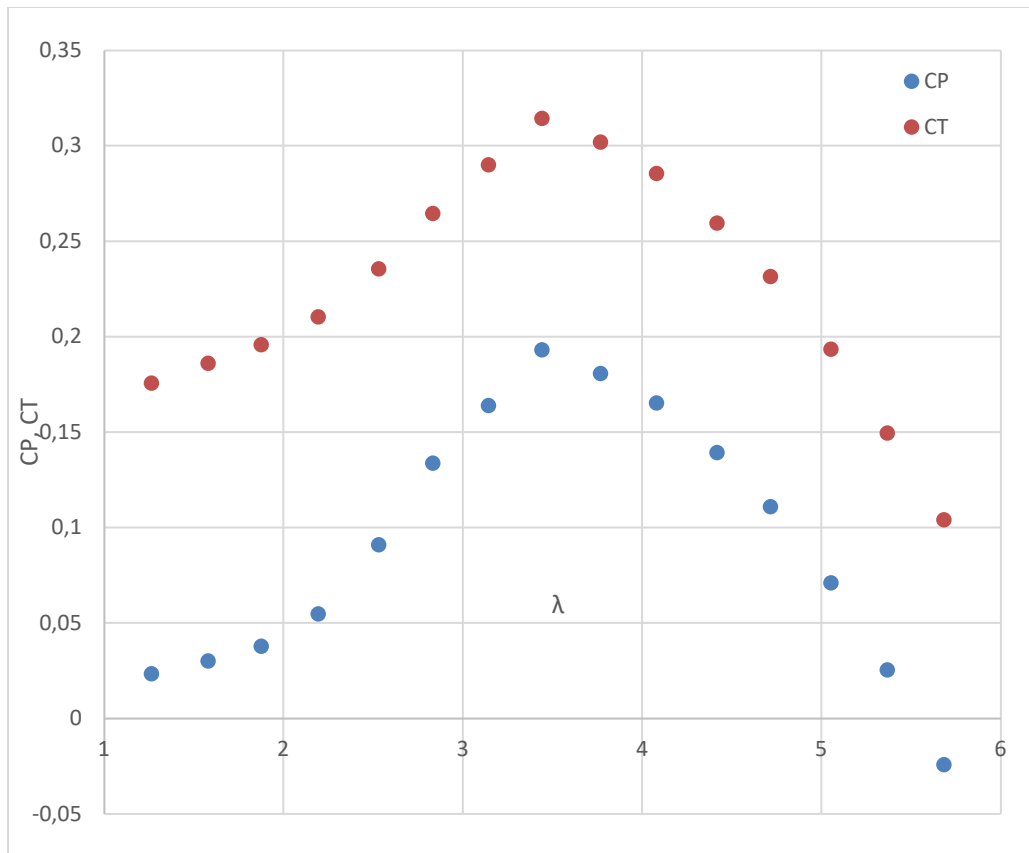


Figure 31: $\alpha=8, \beta=0, P_0=220kPa$

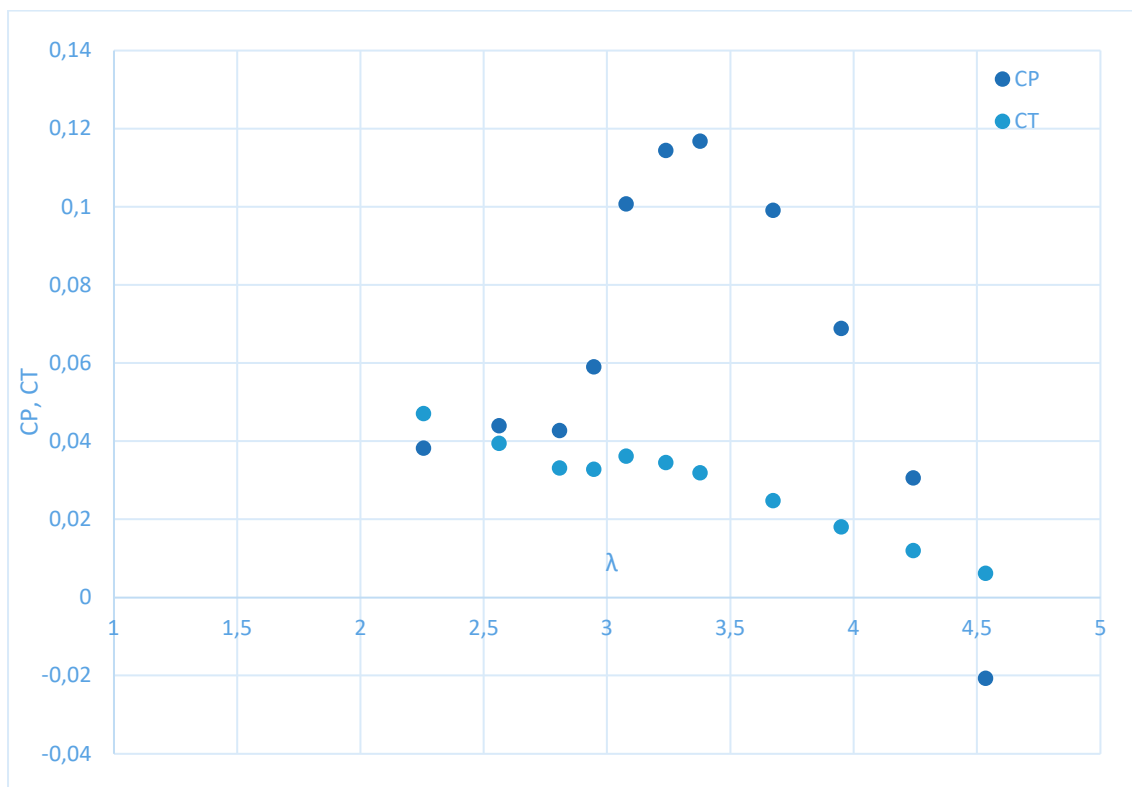


Figure 32: $\alpha=12, \beta=0, P_0=220kPa$

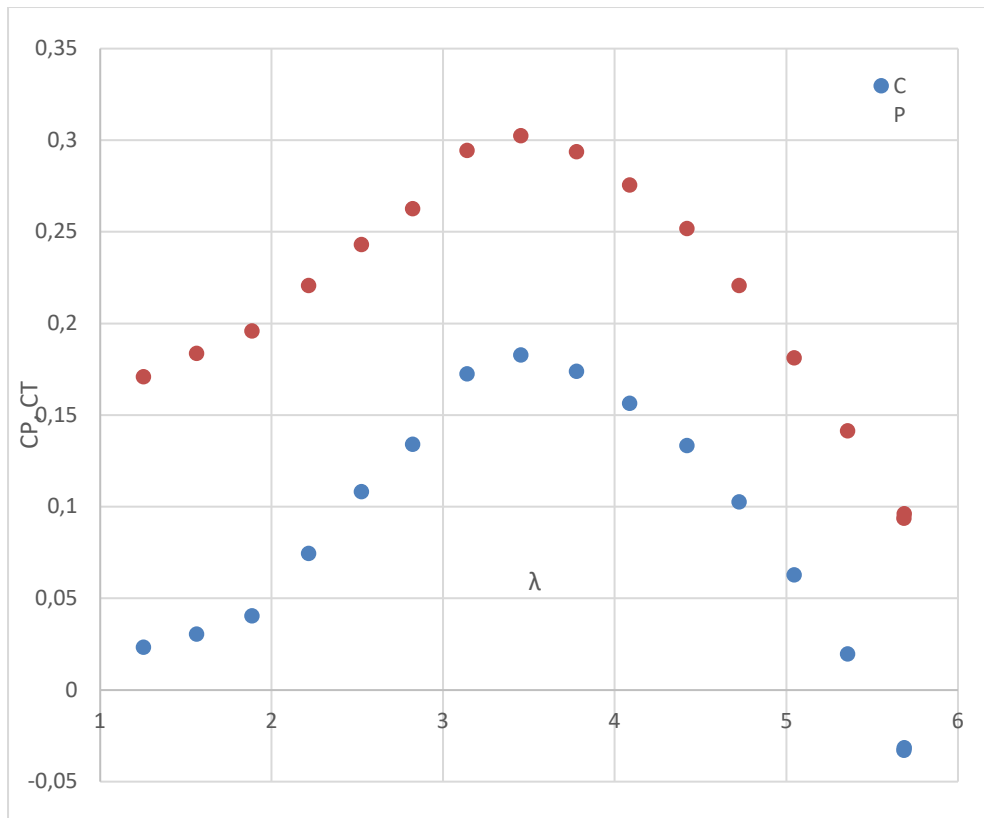


Figure 33: $\alpha = 8, \beta = 7, P_0 = 220 \text{ kPa}$

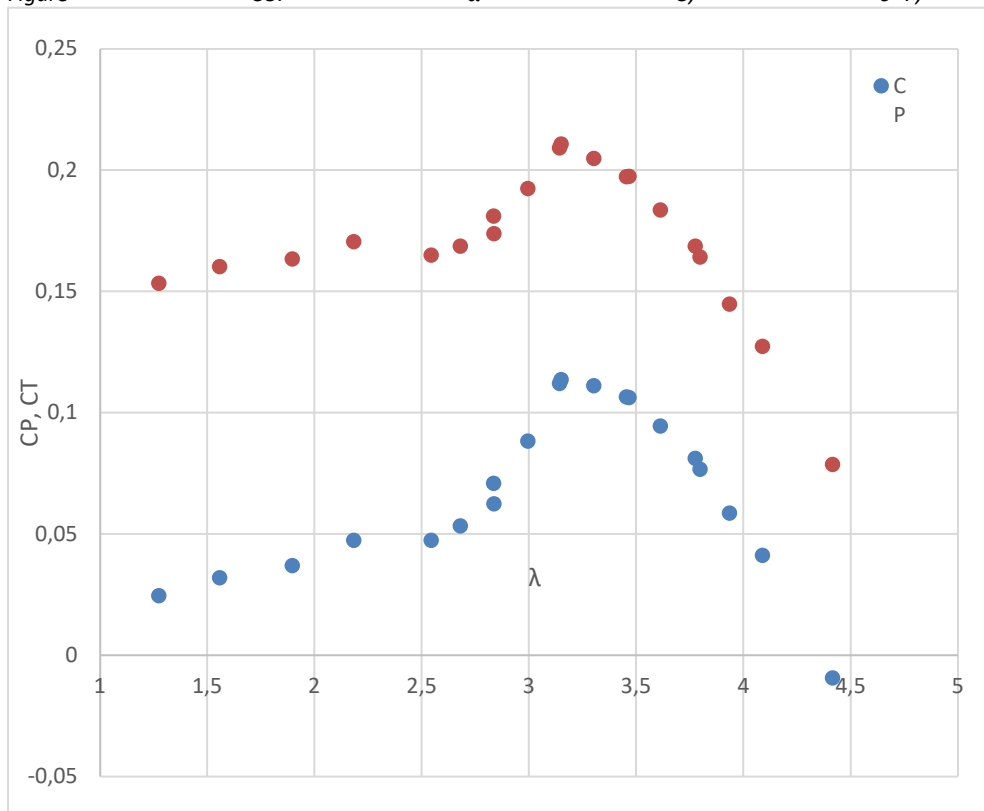


Figure 34: $\alpha = 12, \beta = 7, P_0 = \text{Atm}$

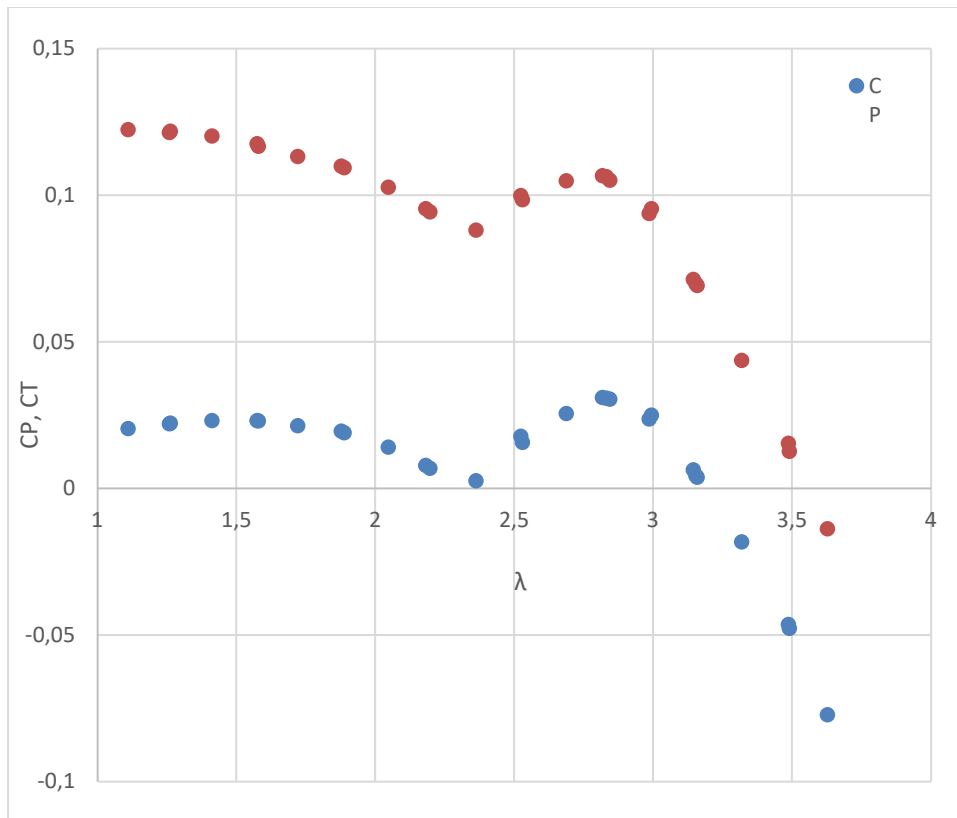


Figure 35: $\alpha = 18, \beta = 7, P_0 = \text{Atm}$

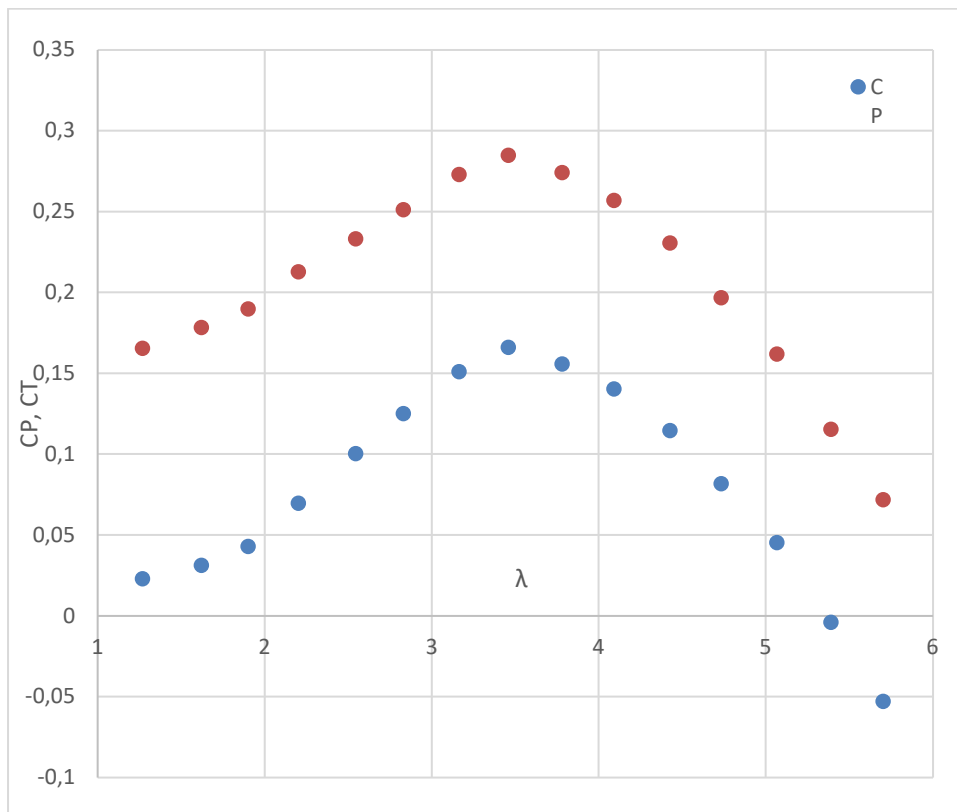


Figure 36: $\alpha = 8, \beta = 13, P_0 = 220\text{kPa}$

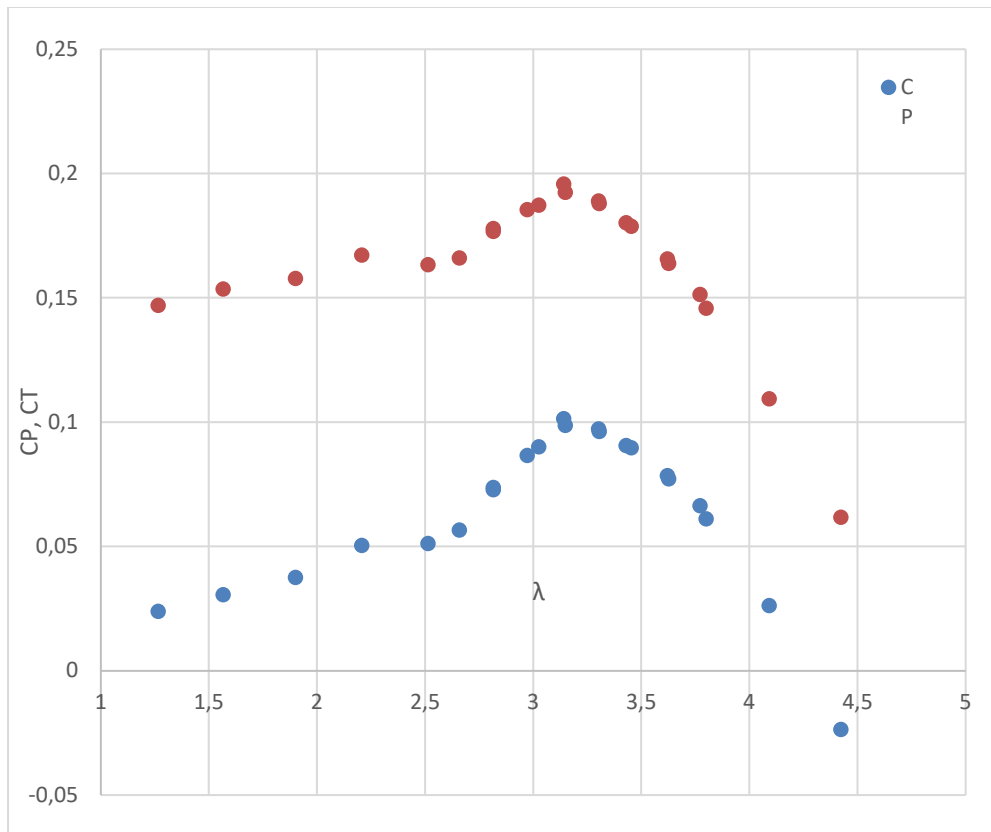


Figure 37: $\alpha = 12, \beta = 13, P_0 = \text{Atm}$

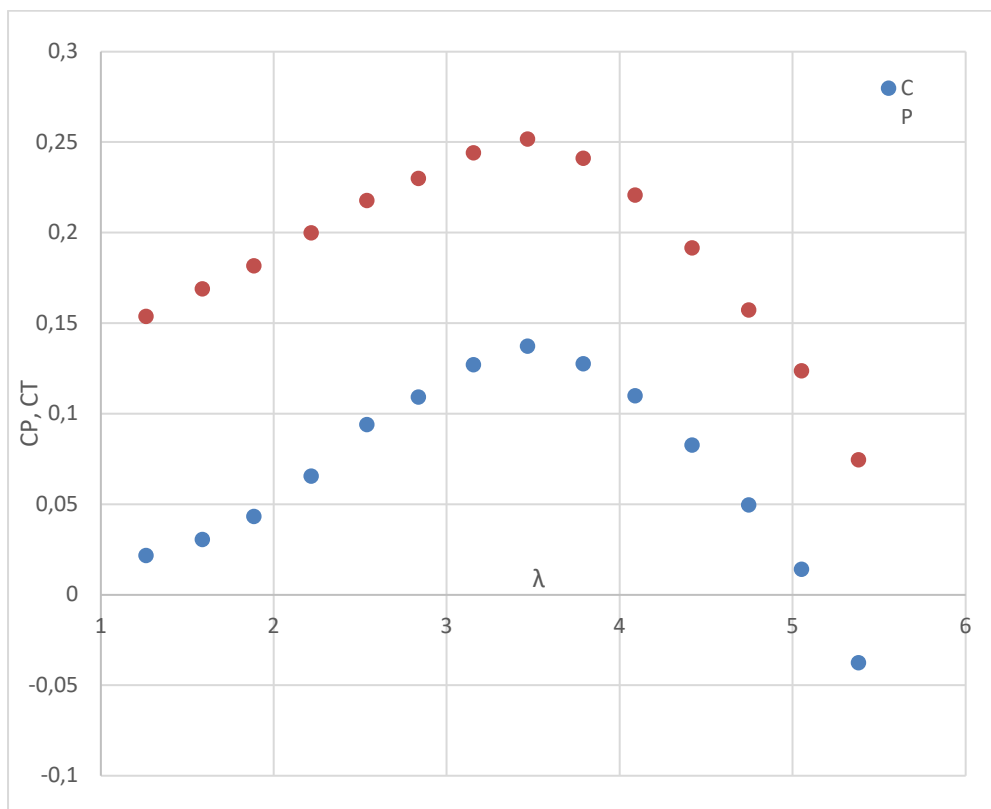


Figure 38: $\alpha = 8, \beta = 19,5, P_0 = 220\text{kPa}$

LDV measurements on Blade 1

Turbine's torque and thrust were measured in SSPA cavitation tunnel. To improve the turbine performance and interaction between two turbines in different yaw angles, flow velocity measurement in different positions in upstream and downstream of the turbine is needed.

LDV (Laser Doppler Velocimetry) measurement is a non-intrusive method to measure velocity components of a position inside the flow by focusing two laser beams through the test section's window. In Figure 39, laser beams are focusing on a position behind the turbine to measure water velocity in that position.

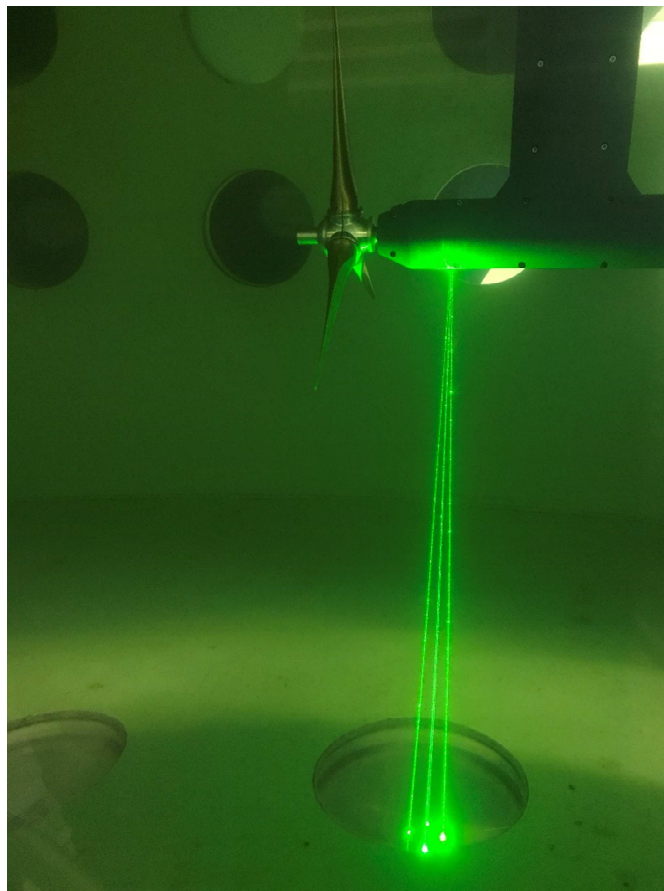


Figure 39 - LDV measurement inside SSPA Cavitation tunnel.

We used Dantec dynamics's solid state Laser which generates two laser beams in different wavelengths to measure two components of the velocity simultaneously. Beams are focused using a lens located under the test section (see Figure 40). Laser and lens were mounted on a 3D traverse system to allow the point measurement movement in the volume in the flow field visible through the access window. To measure more points in the flow, traverse system moved between two windows under the test section as shown in Figure 39. The direction of two velocity components measured simultaneously by LDV setup is shown on the laser system in Figure 41. These two components were streamwise velocity and crossflow

component, perpendicular to the first component, parallel to the measurement window and with the positive direction towards starboard of the turbine.

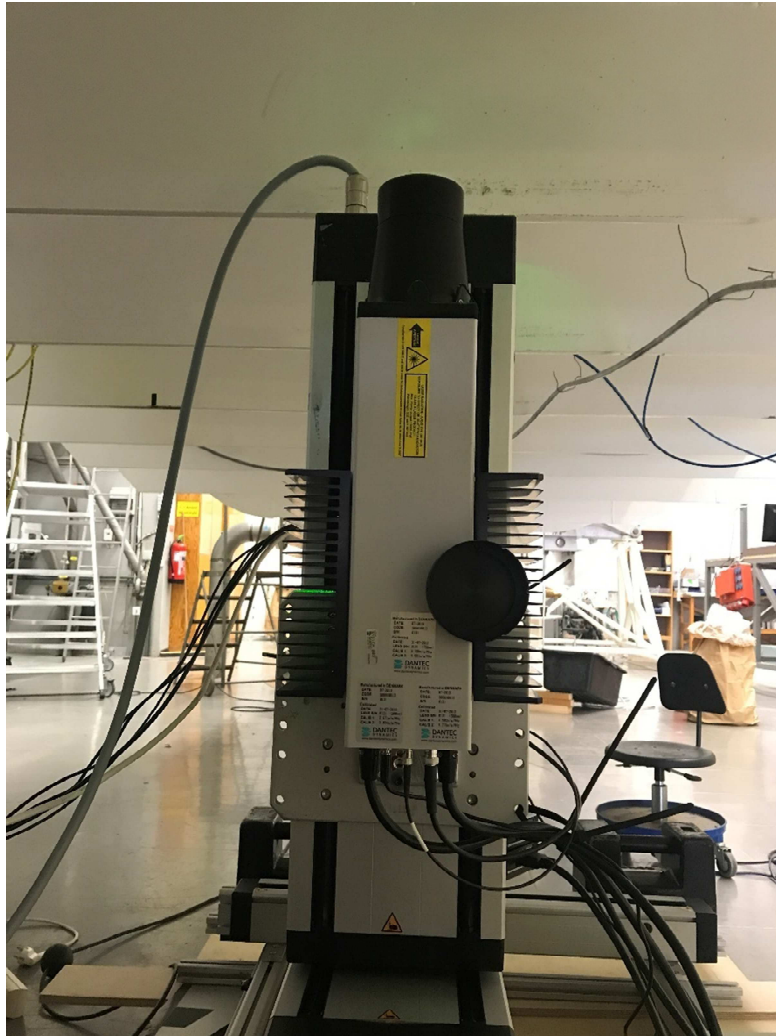


Figure 40 – Solid-state laser and LDV lens.



Figure 41 - Direction of two measured velocity components.

Velocity measurements were performed in 3 planes. Plane 1 was positioned 0.75R upstream of turbine blades, Plane 2 was 0.75 downstream of turbine blades and Plane 3 at the position of the downstream turbine blades. Figure 42 shows the turbine at 19.5 degrees yaw angle with the windows in the bottom of the section illustrated by circles. As the size of windows did not allow the entire plane to be measured in a single run, planes were divided into two sections (starboard side and port side) and measured separately. This way by moving the turbine position inside the test section we made the desired plane section visible through respective window.

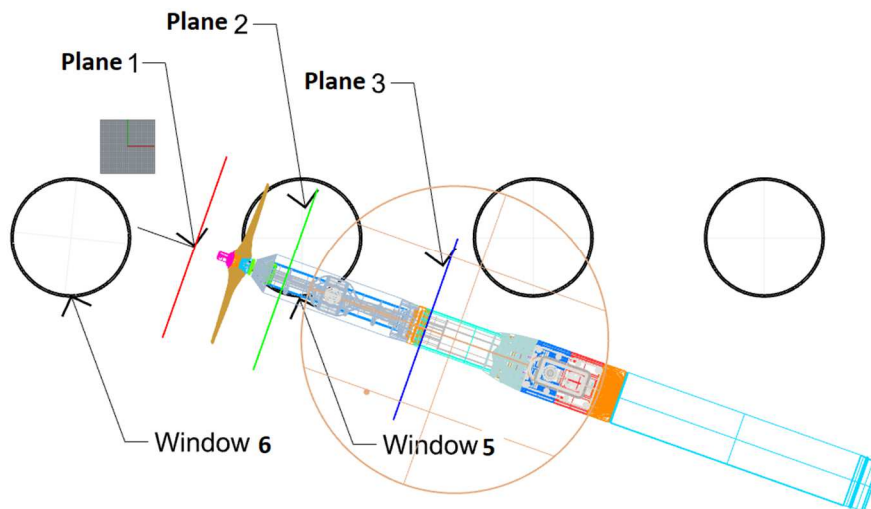


Figure 42- Positions for LDV measurement planes through tunnel windows for the turbine with 19.5 degree Yaw angle.



Figure 43 - Turbine model mounted inside the cavitation tunnel. Measurement windows are visible at the bottom of the test section.

Table 9 lists the measurement runs for different planes. Runs were performed for two sets of turbine alignments: with zero yaw angle and with 19.5 degree yaw angle. In the result of measurement two sides of each plane are combined and presented. Average water speed in the tunnel was 2.5 m/s for all runs and shaft rotational speed was 10 rps.

Table 9- LDV measurement runs.

Run #	Measurement Plane	Test section window #	Turbine Yaw Angle	Turbine side
Run 1	Plane 1	window 6	0	Port side
Run 2	Plane 3	window 5	0	Port side
Run 3	Plane 3	window 5	0	starboard side
Run 4	Plane 1	window 6	0	starboard side
Run 5	Plane 2	window 6	0	starboard side
Run 6	Plane 2	window 5	0	Port side
Run 7	Upstream	window 6	Freestream	-
Run 8	Plane 1	window 6	19.5	Port side
Run 9	Plane 3	window 5	19.5	starboard side

Run 10	Plane 3	window 5	19.5	Port side
Run 11	Plane 2	window 5	19.5	Port side
Run 12	Plane 2	window 5	-19.5	starboard side
Run 13	Plane 3	window 5	-19.5	Port side

Measurement points were placed in different radii around the turbine shaft. Figure 44 shows distribution of the points inside each plane. In every run some of the points were not accessible, as they were blocked by the hub or turbine body.

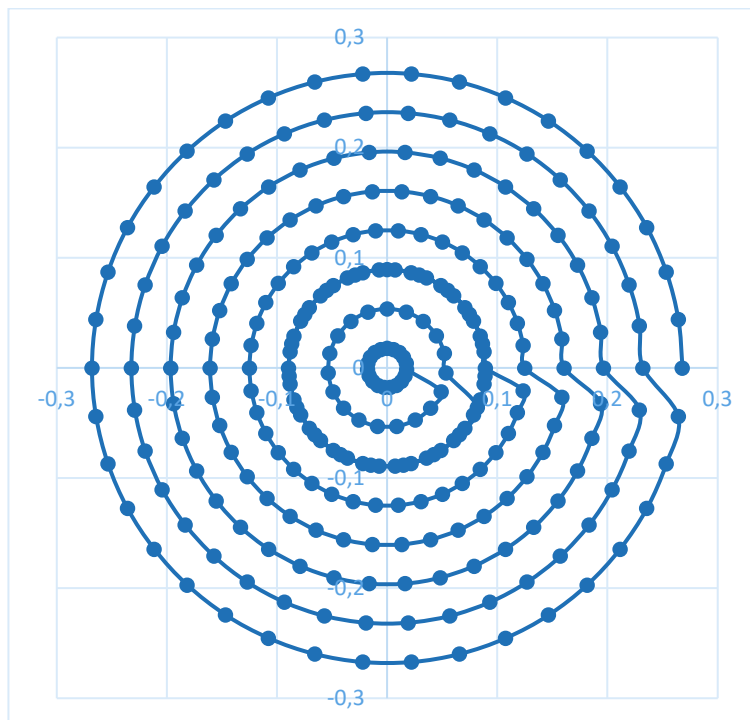


Figure 44- measurement points distributed in each plane.

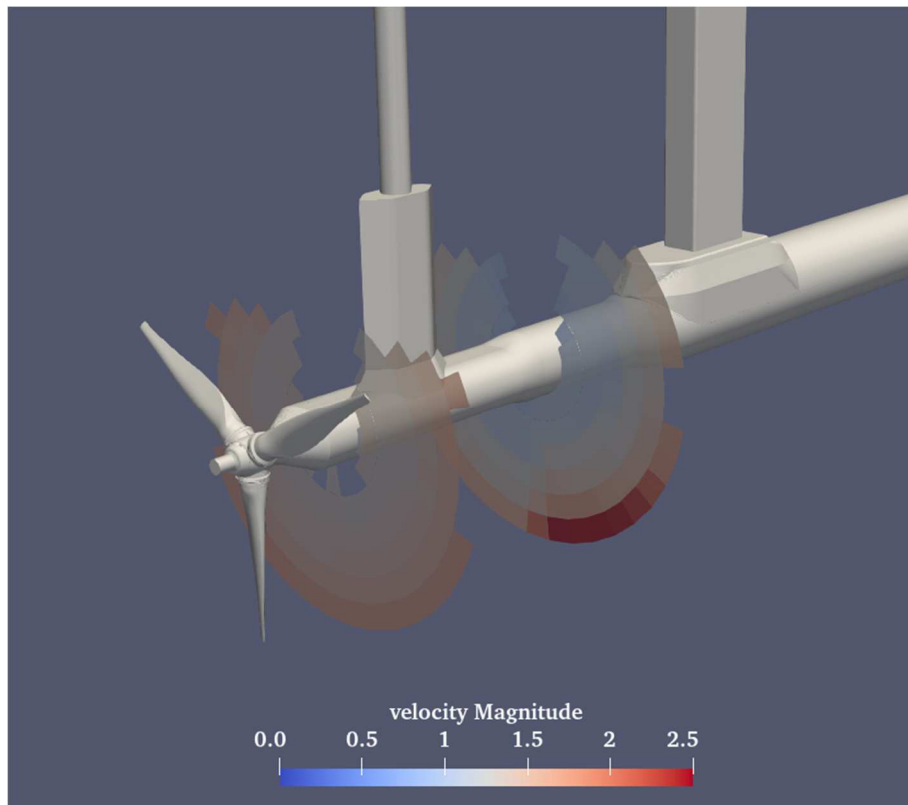


Figure 45- Measurement result for two planes downstream of the turbine.

Figure 45 presents the results of the velocity magnitude in two planes. The upper section of planes was not visible through the bottom window and was not measured. The data for measurement is converted into VTK format, a text file readable by many post-processing software including ParaView. Data is in form of velocity vector for the points in each plane. To convert the data into VTK format, each measurement point is represented by a cell with the average velocity vector at the center of the cell. Measurement results are presented in Figure 46 - Figure 63.

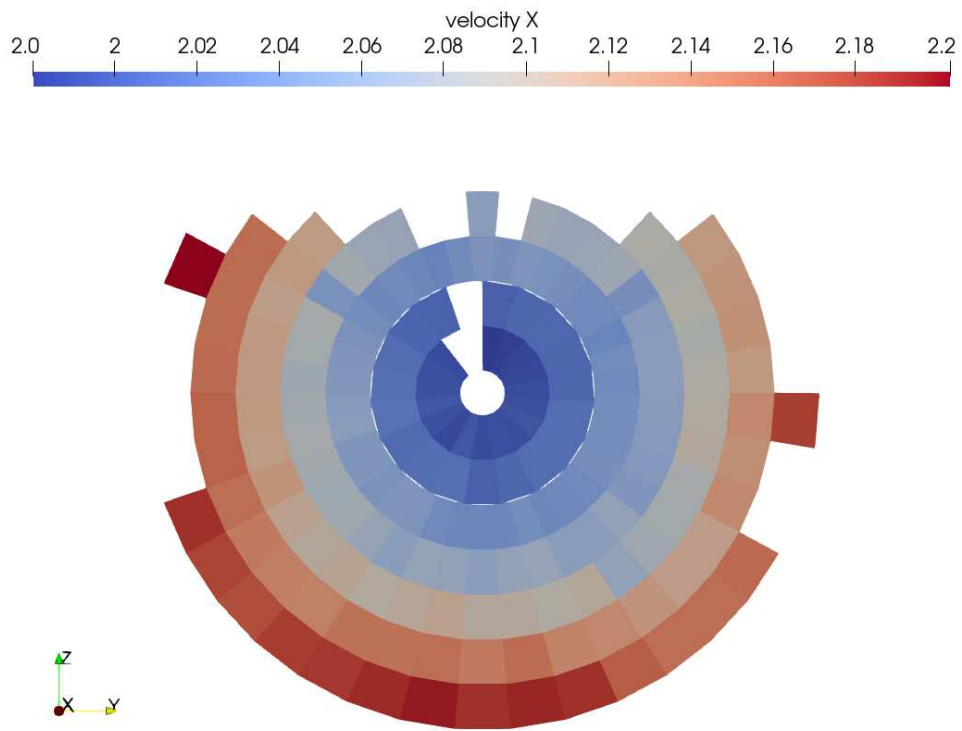


Figure 46- Plane 1, Yaw angle 0, streamwise velocity component V_x .

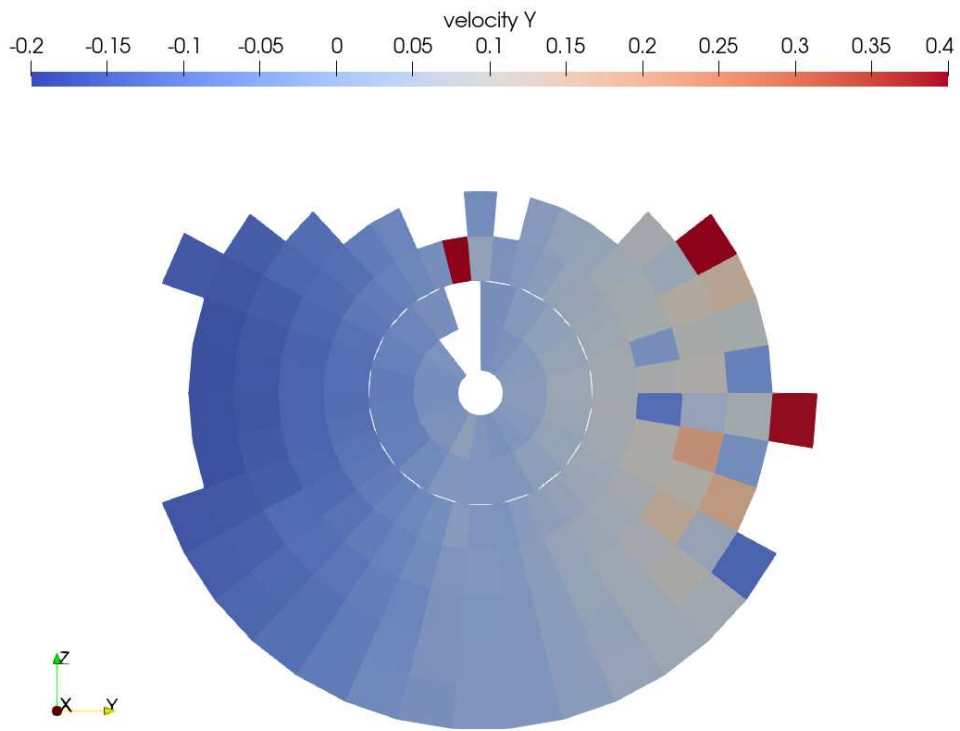


Figure 47- Plane1, Yaw angle 0, cross flow velocity component V_y .

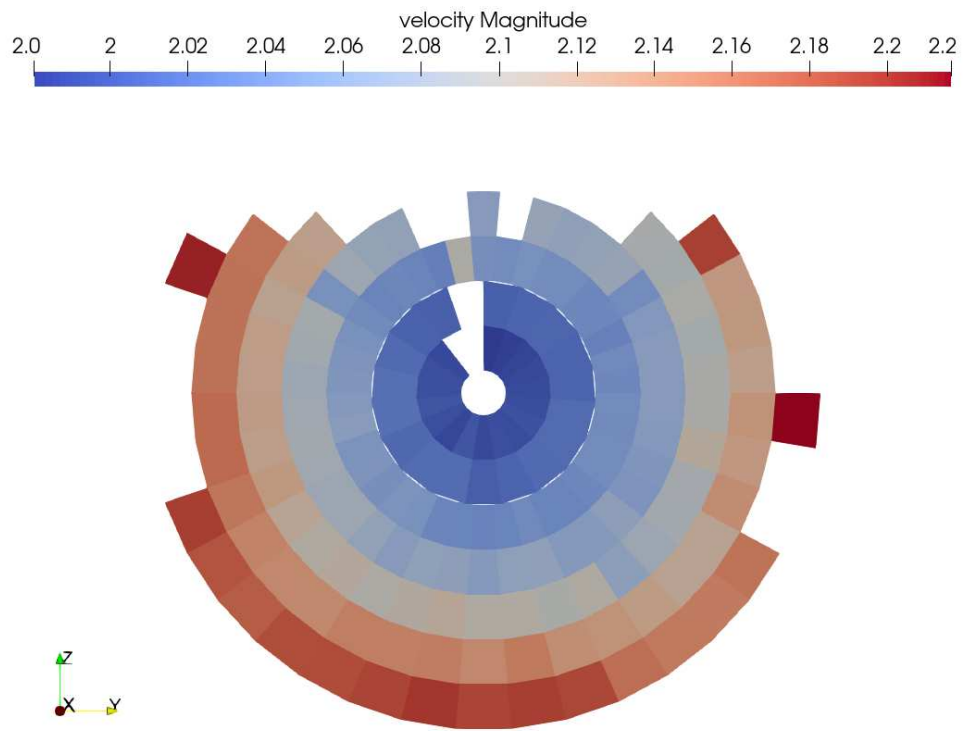


Figure 48- Plane 1, Yaw angle 0, average velocity magnitude.

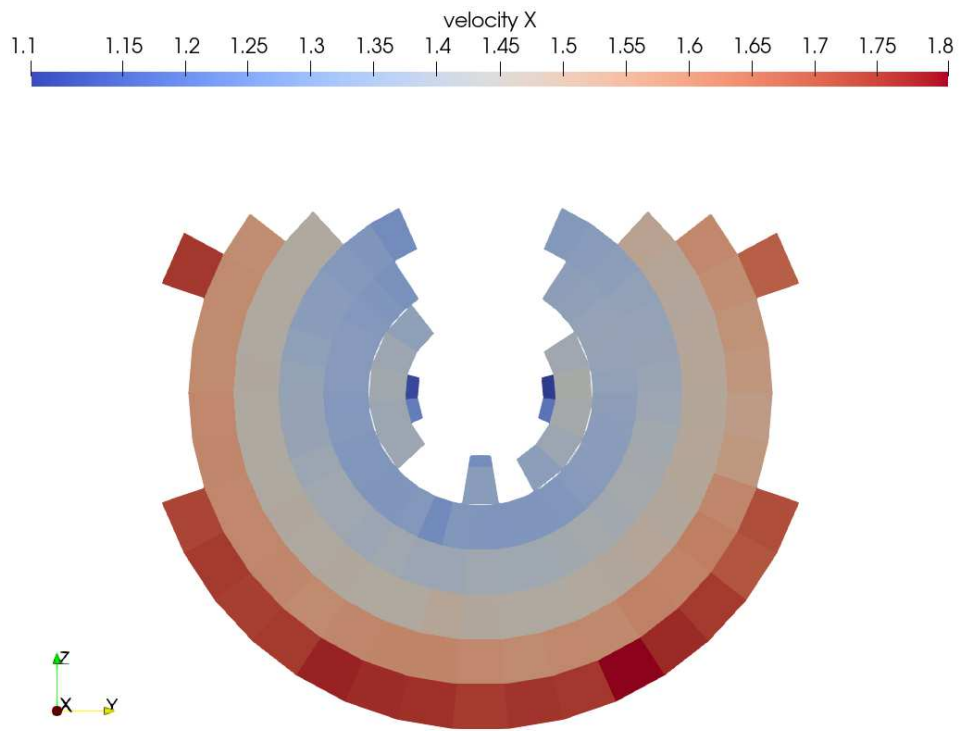


Figure 49- Plane2, Yaw angle 0, streamwise velocity component V_x .

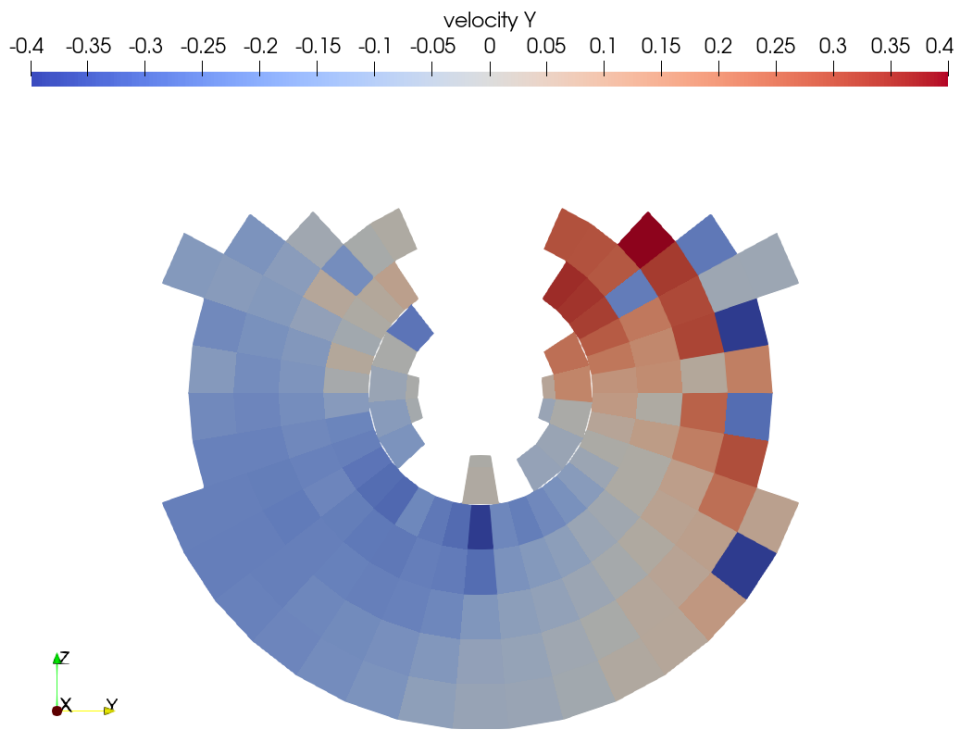


Figure 50- Plane 2, Yaw angle 0, cross flow velocity component V_y .

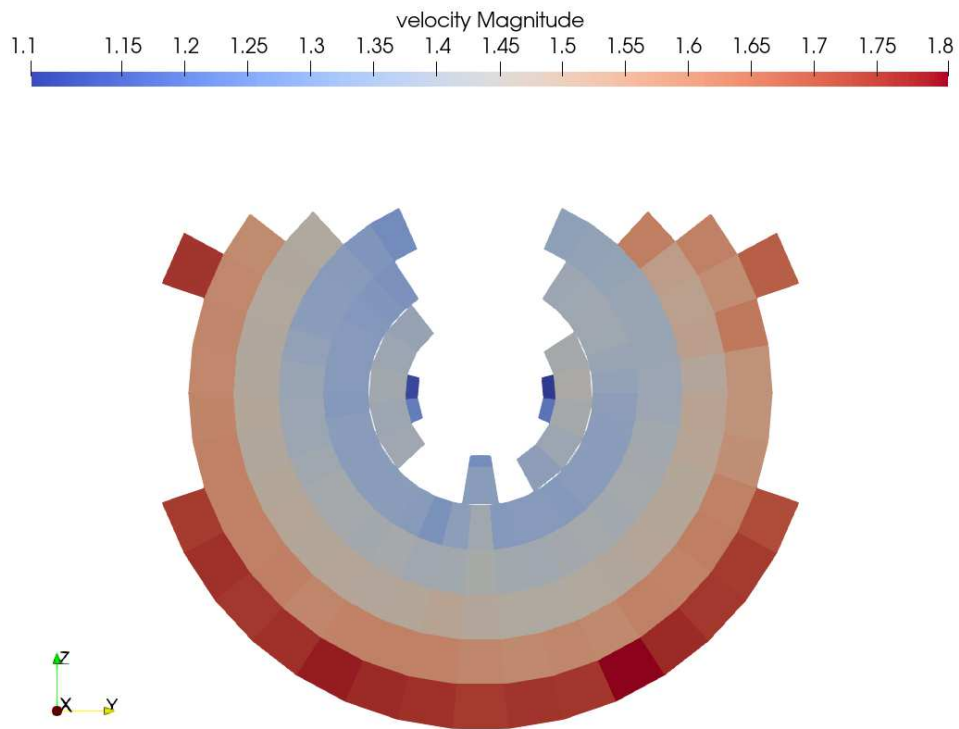


Figure 51- Plane 2, Yaw angle 0, average velocity magnitude.

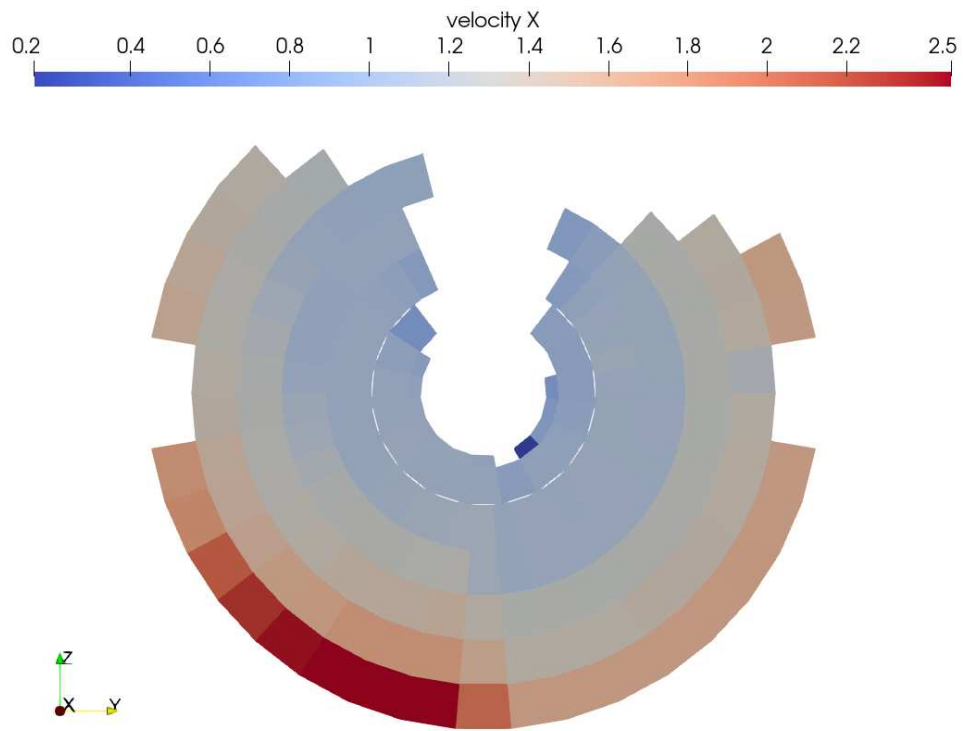


Figure 52- Plane 3, Yaw angle 0, streamwise velocity component V_x .

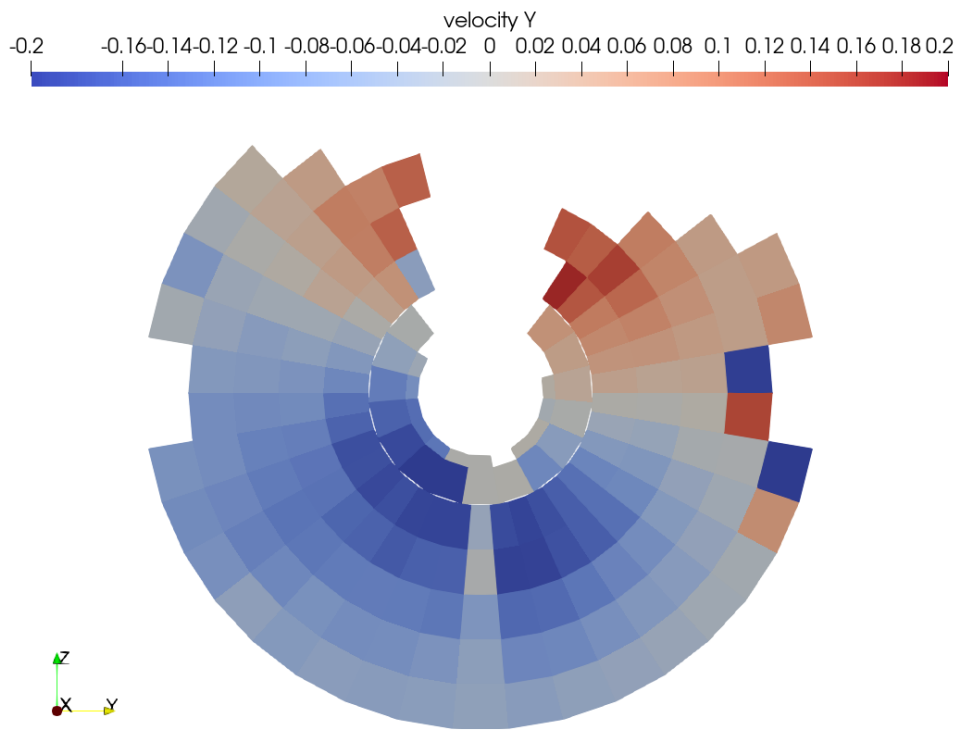


Figure 53- Plane 3, Yaw angle 0, cross flow velocity component V_y .

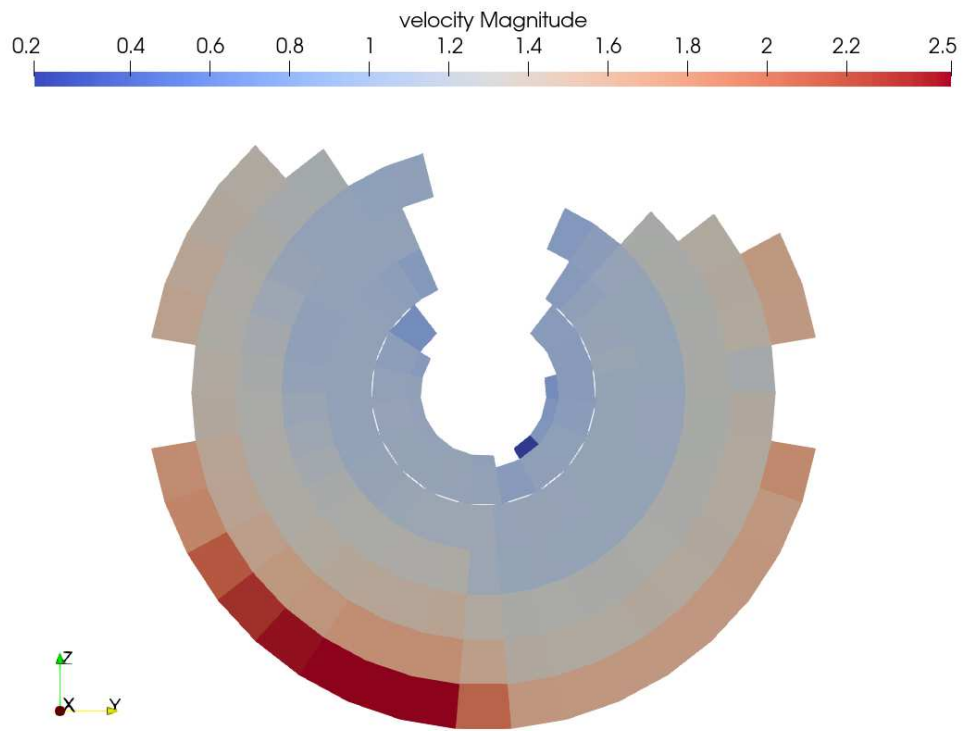


Figure 54- Plane 3, Yaw angle 0, average velocity magnitude.

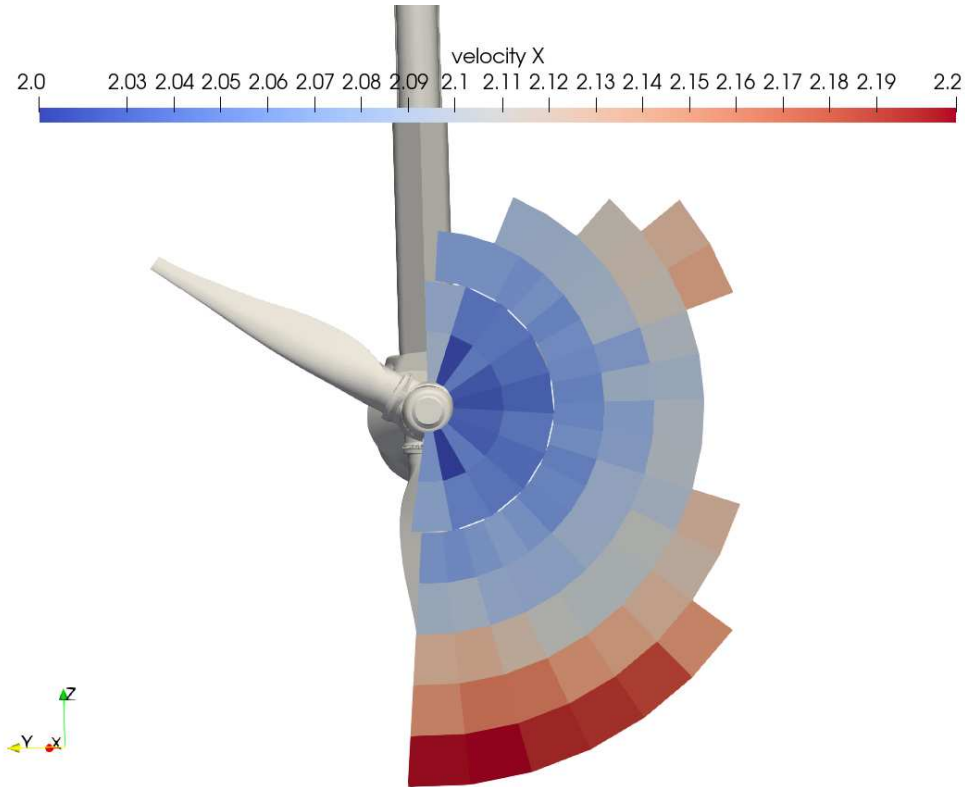


Figure 55- Plane 1, Yaw angle 19.5, streamwise velocity component V_x .

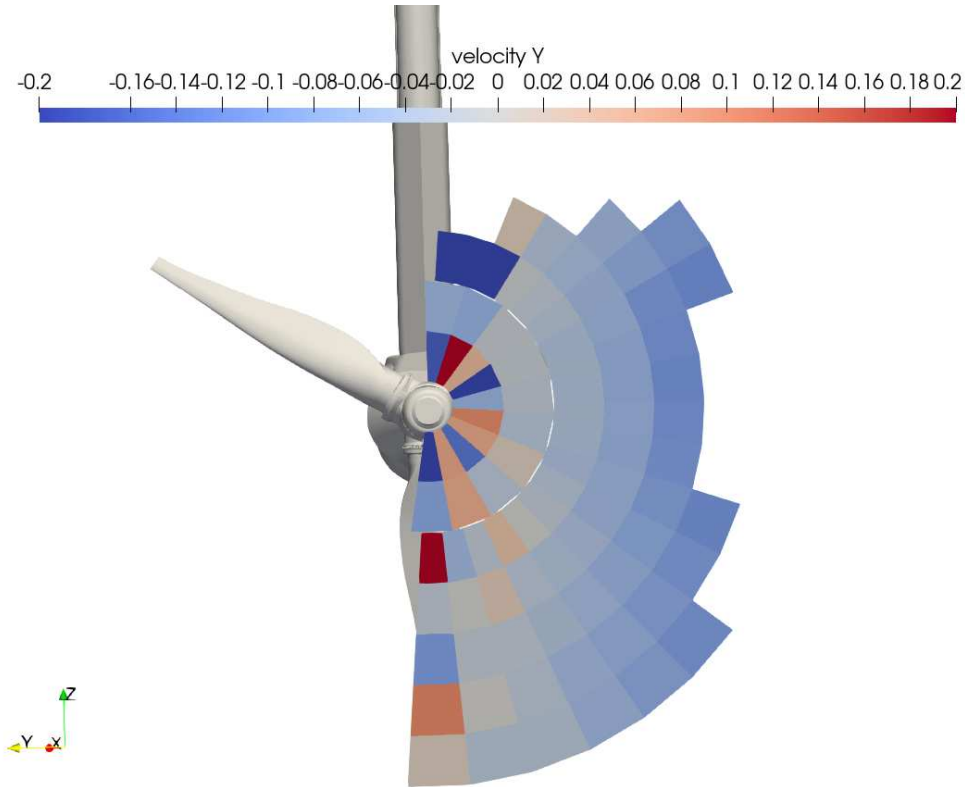


Figure 56- Plane1, Yaw angle 19.5, cross flow velocity component V_y .

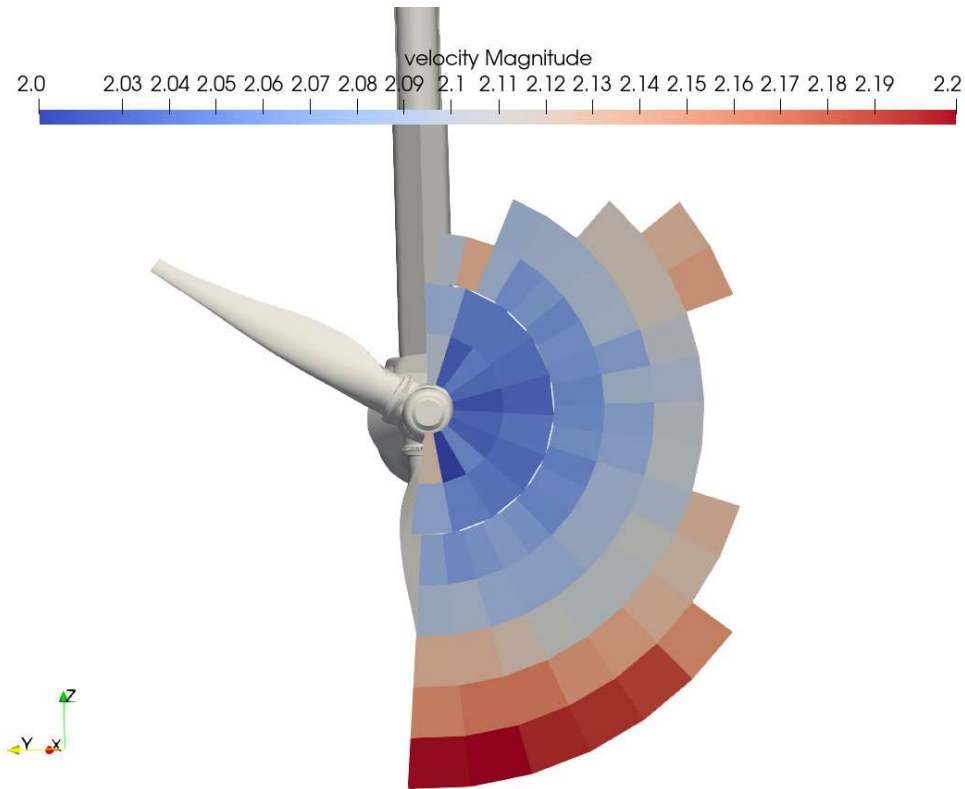


Figure 57- Plane 1, Yaw angle 19.5, average velocity magnitude.

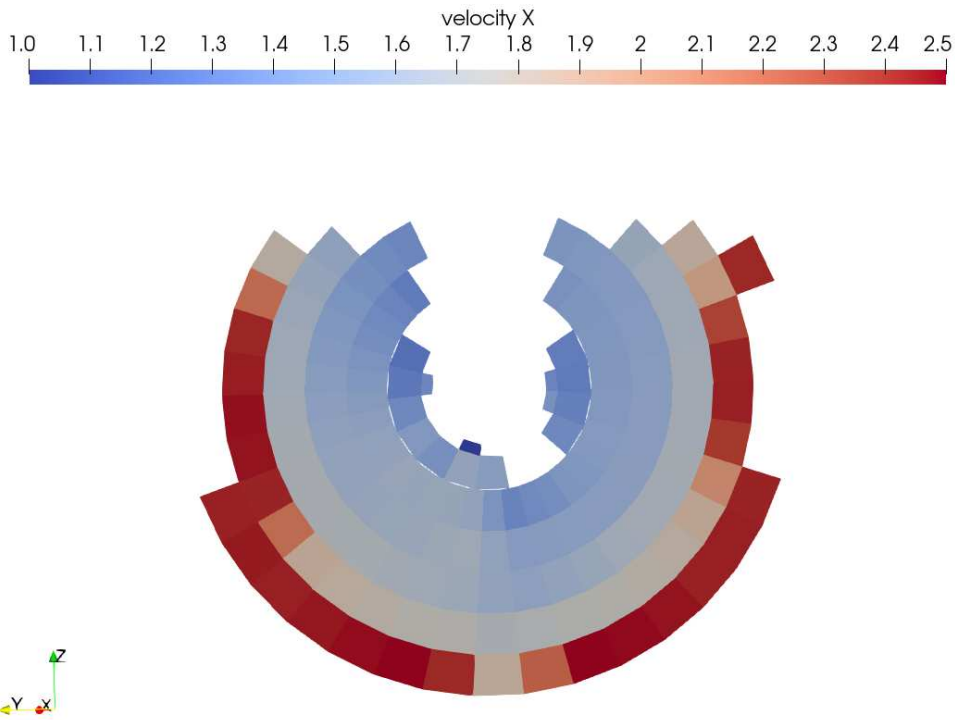


Figure 58- Plane2, Yaw angle 19.5, streamwise velocity component V_x .

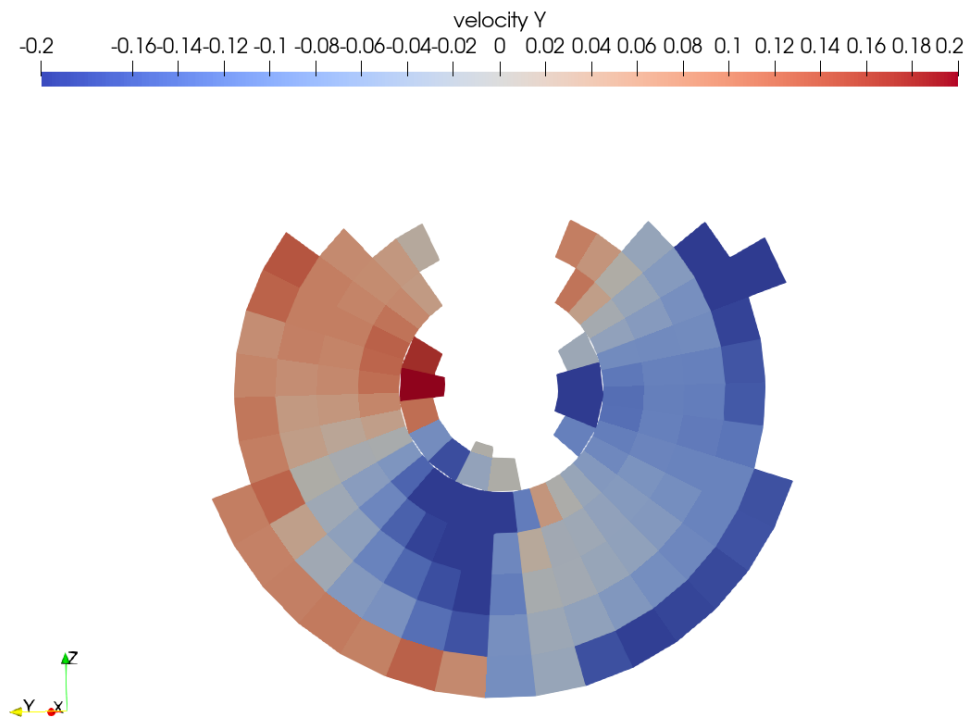


Figure 59- Plane 2, Yaw angle 19.5, cross flow velocity component V_y .

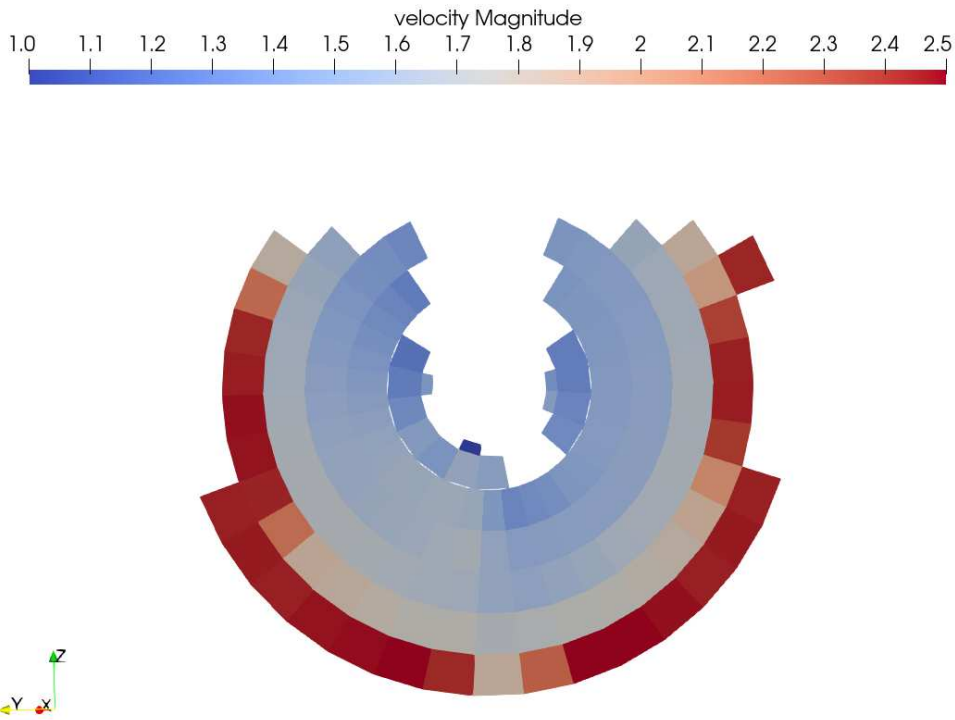


Figure 60- Plane 2, Yaw angle 19.5, average velocity magnitude.

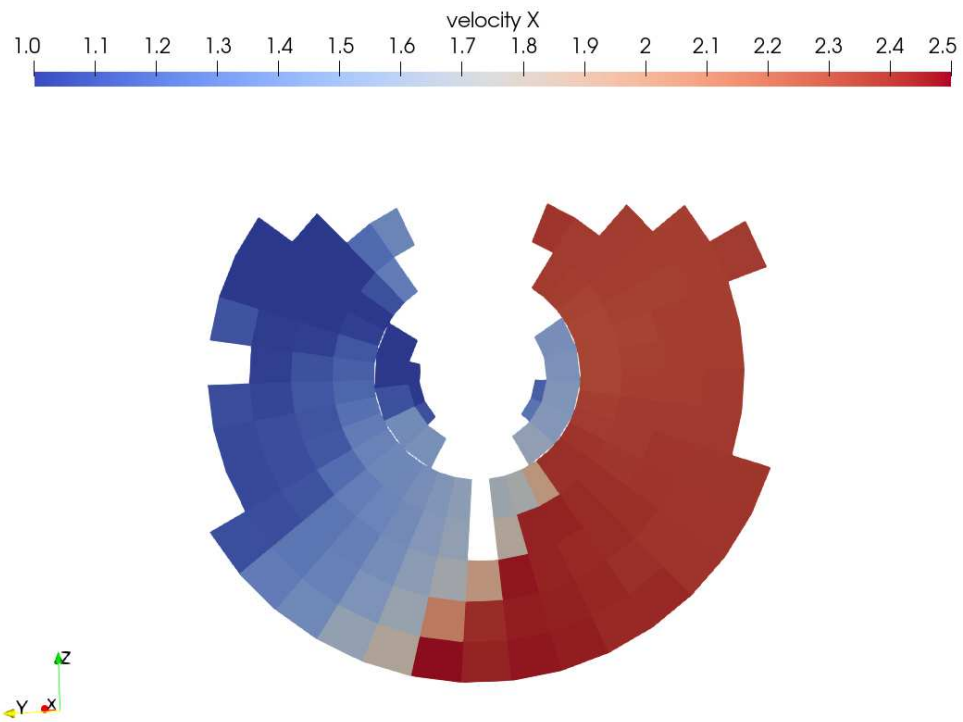


Figure 61- Plane 3, Yaw angle 19.5, streamwise velocity component V_x .

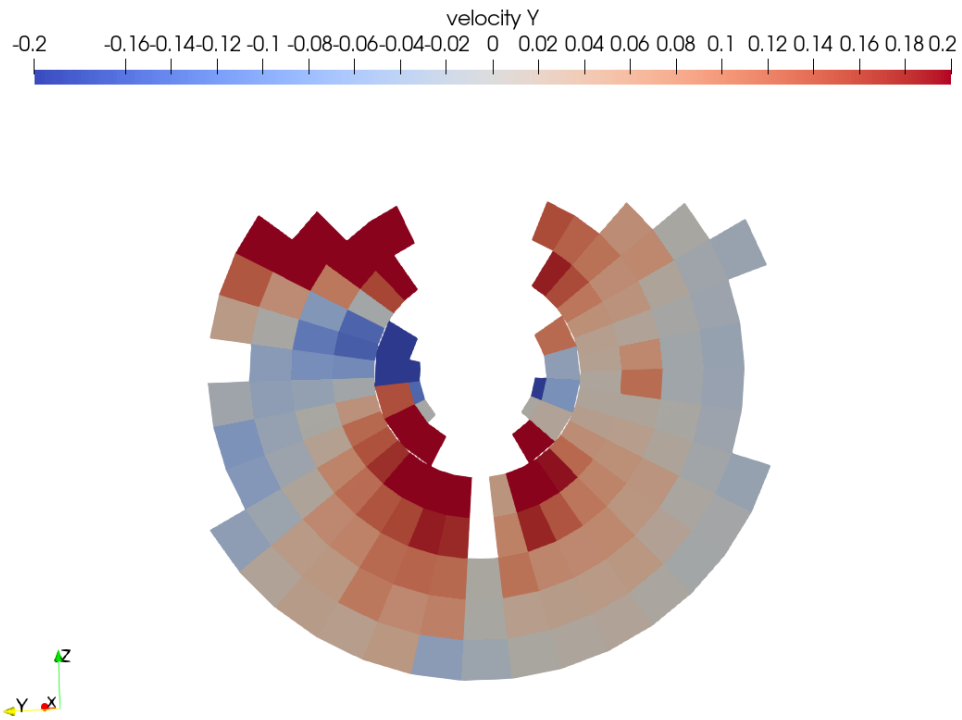


Figure 62- Plane 3, Yaw angle 19.5, cross flow velocity component V_y .

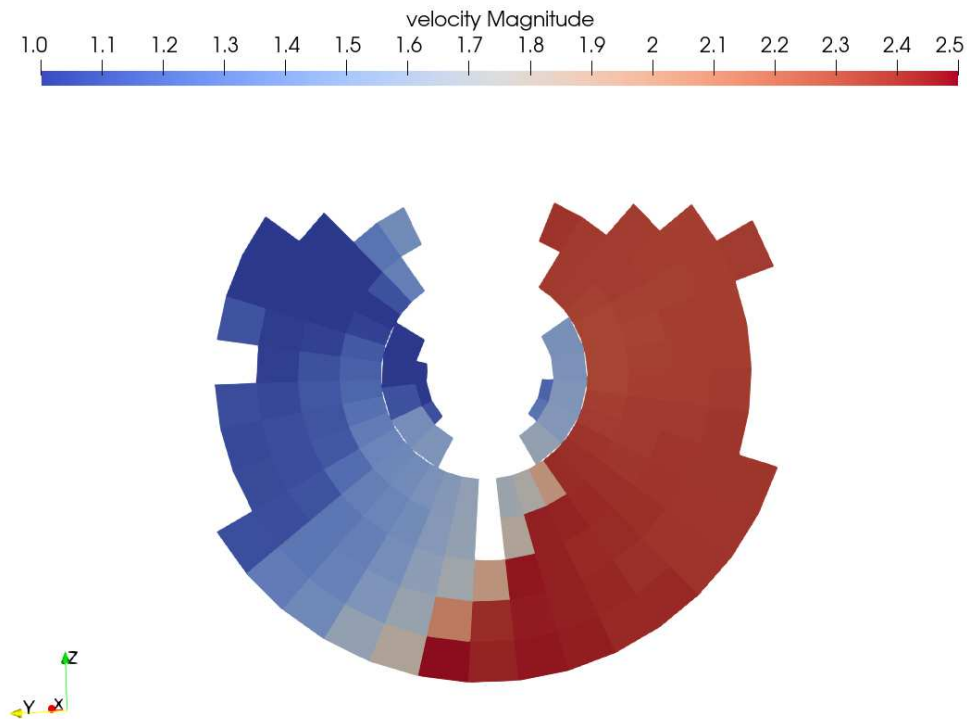


Figure 63- Plane 3, Yaw angle 19.5, average velocity magnitude.

Blade geometry 2

The second blade geometry explores a symmetrical profile (symmetrical between leading and trailing edge). The reason for this choice of geometry is that the turbine will work with flow in both directions, therefore losing some efficiency with a less efficient profile, it could be beneficial when the flow direction is reversed. The profiles installed in the cavitation tunnel can be seen in Figure 65 and Figure 66.

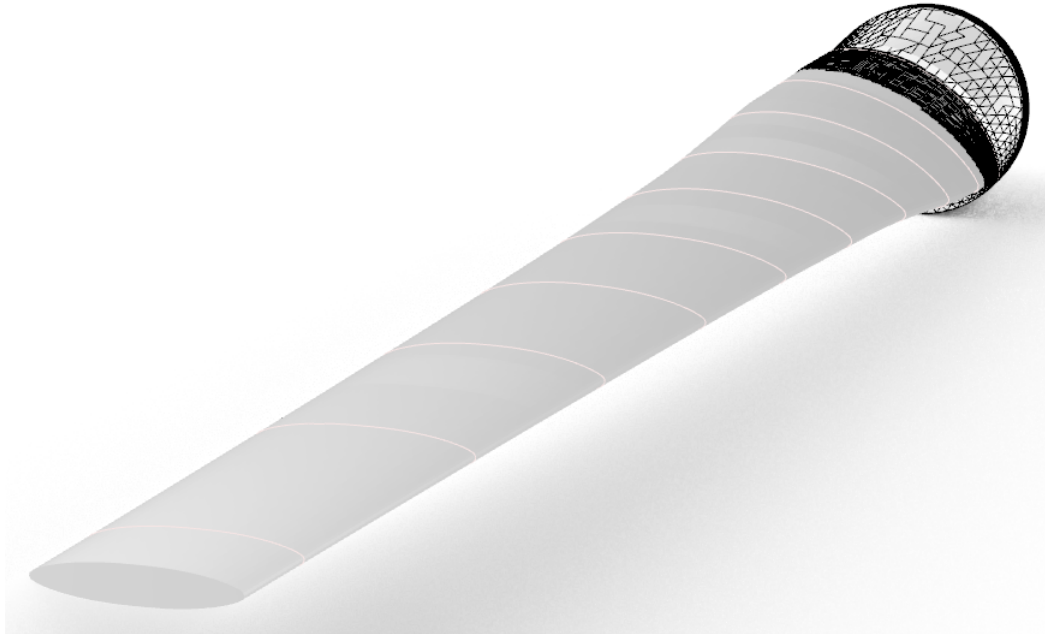


Figure 64: 3D representation of blade



Figure 65: Symmetrical blades



Figure 66: Symmetrical blades

The test programme is described in the table below. No yaw angles were run for these tests

Table 10: Test matrix for blade 2 geometry

Serie	Test	α	B	P_0	Comment
2	1	0	0	220	
3	1	2	0	220	
4	1	6	0	220	
5	1	-2	0	220	
6	2	10	0	220	
7	3	4	0	220	
8	4	8	0	220	

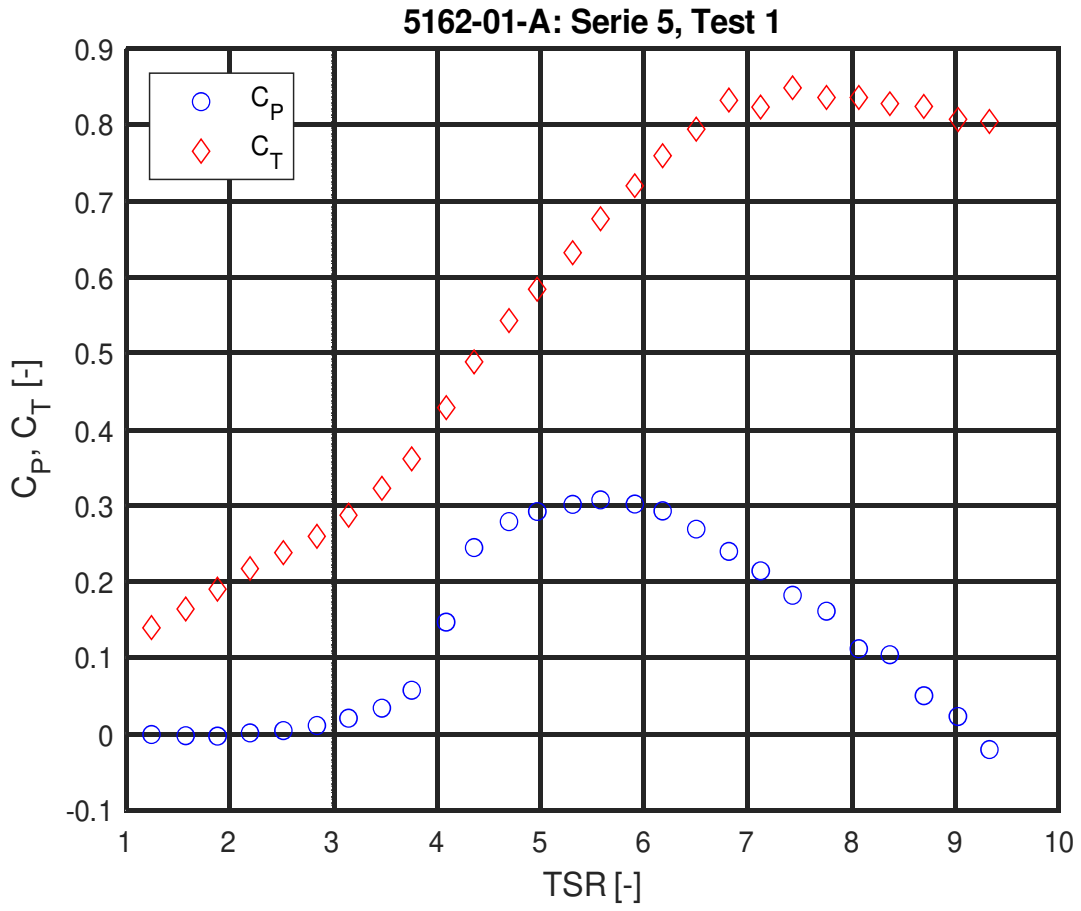


Figure 67: $\alpha = -2$, $\theta = 0$, $P_0 = 220 \text{ kPa}$

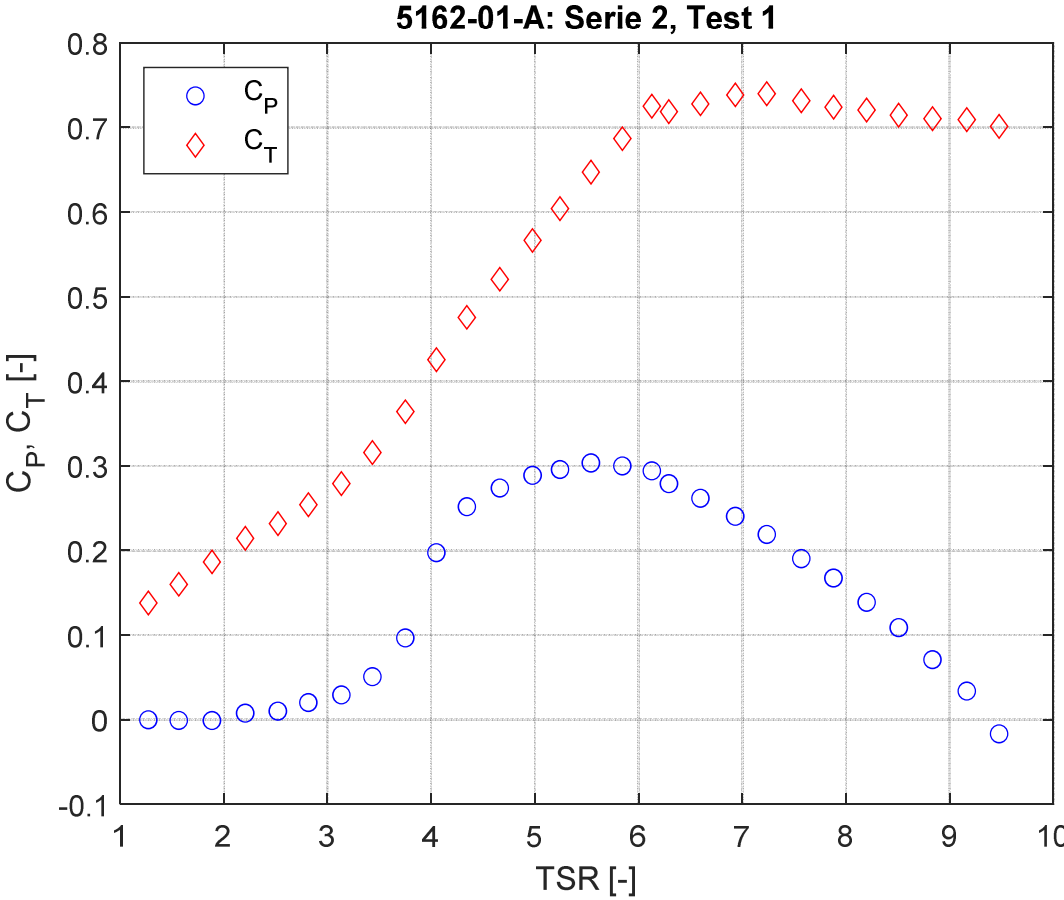


Figure 68: $\alpha=0, \beta=0, P_0=220kPa$

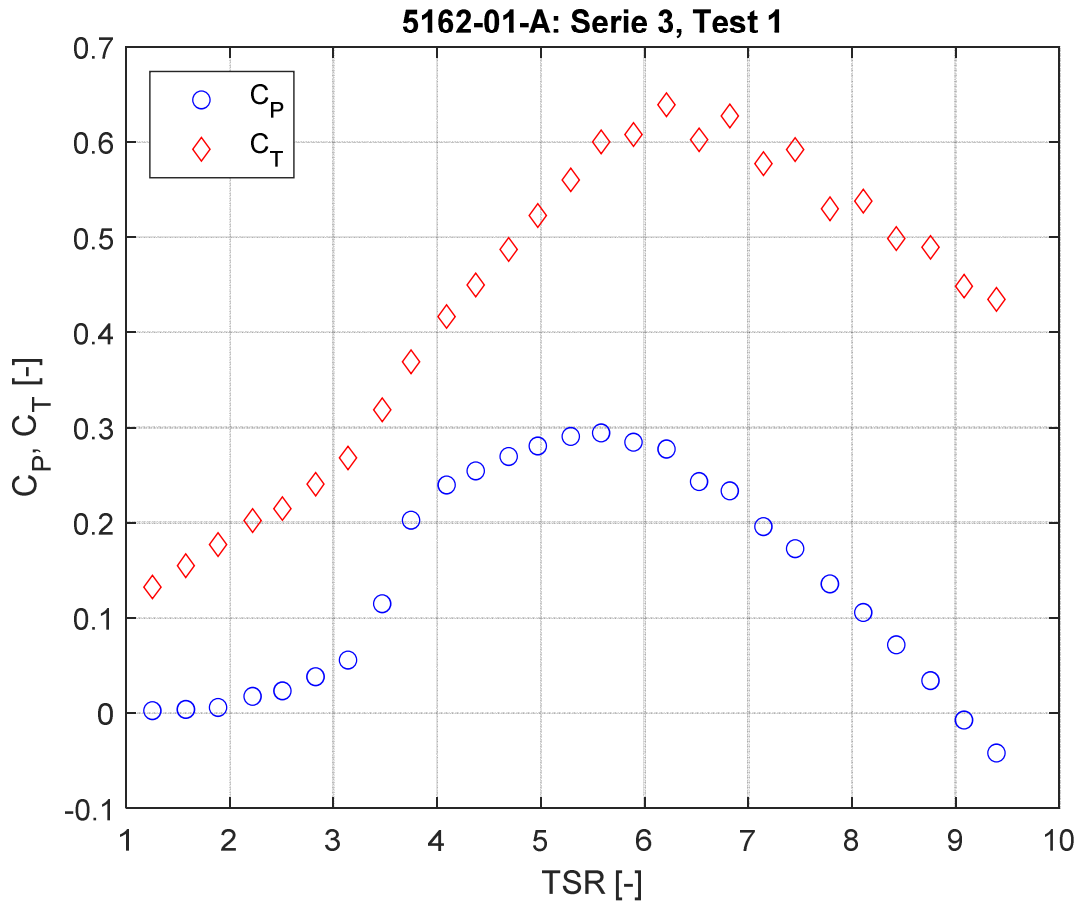


Figure 69: $\alpha=2, \beta=0, P_0=220kP$

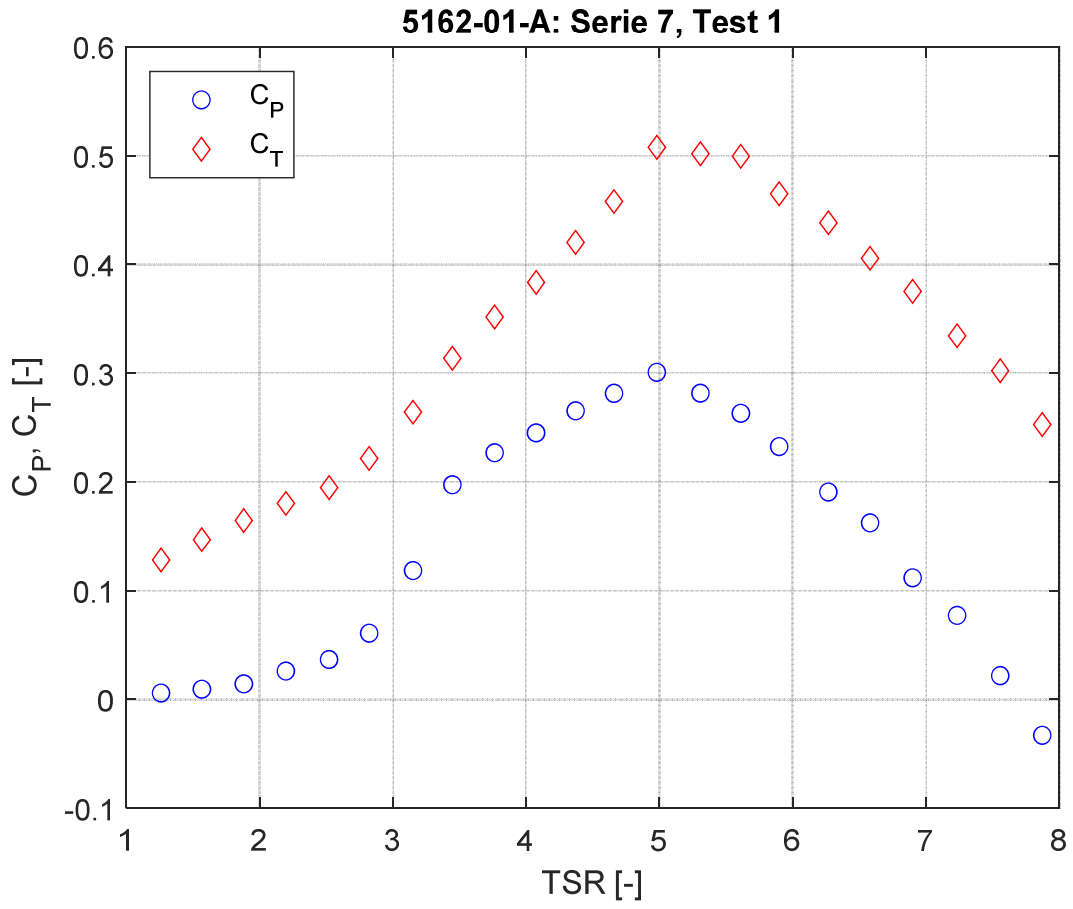


Figure 70: $\alpha=4$, $\beta=0$, $P_0=220kPa$

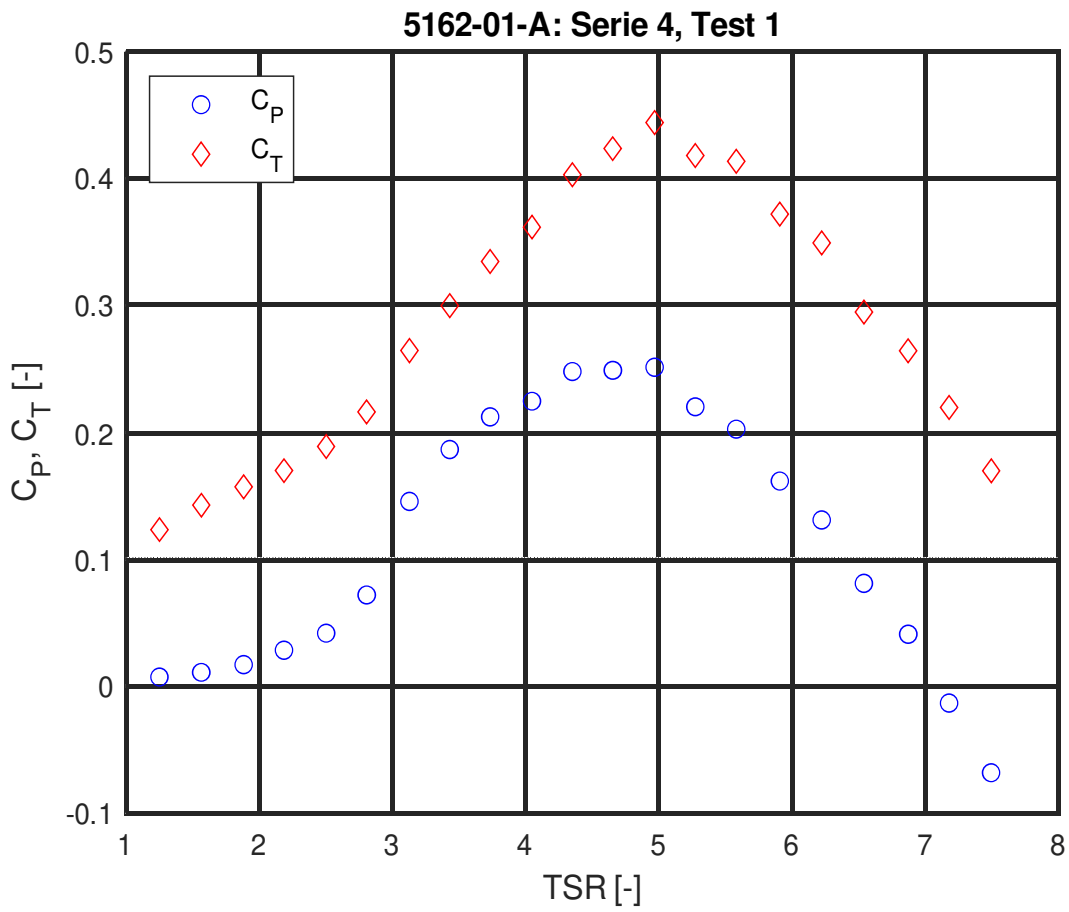


Figure 71: $\alpha = 6, \beta = 0, P_0 = 220 \text{ kPa}$

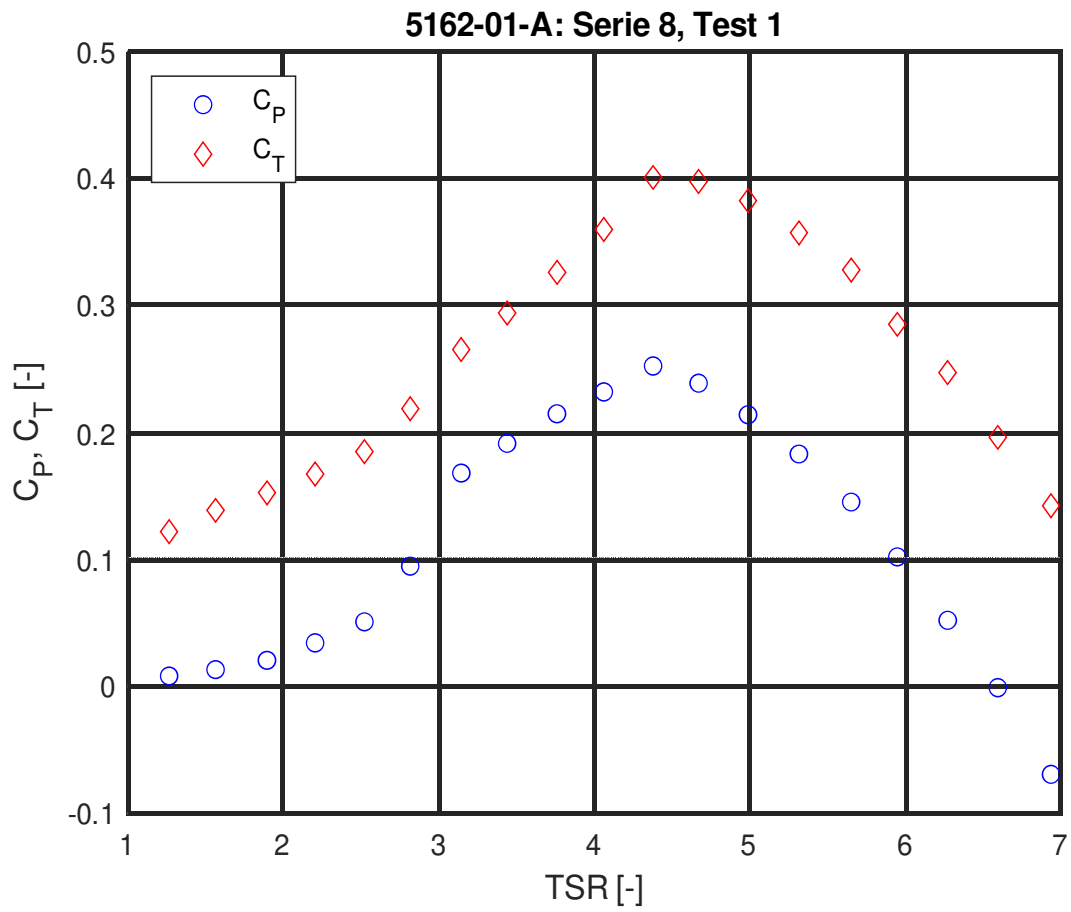


Figure 72: $\alpha = 8$, $\beta = 0$, $P_0 = 220 \text{ kPa}$

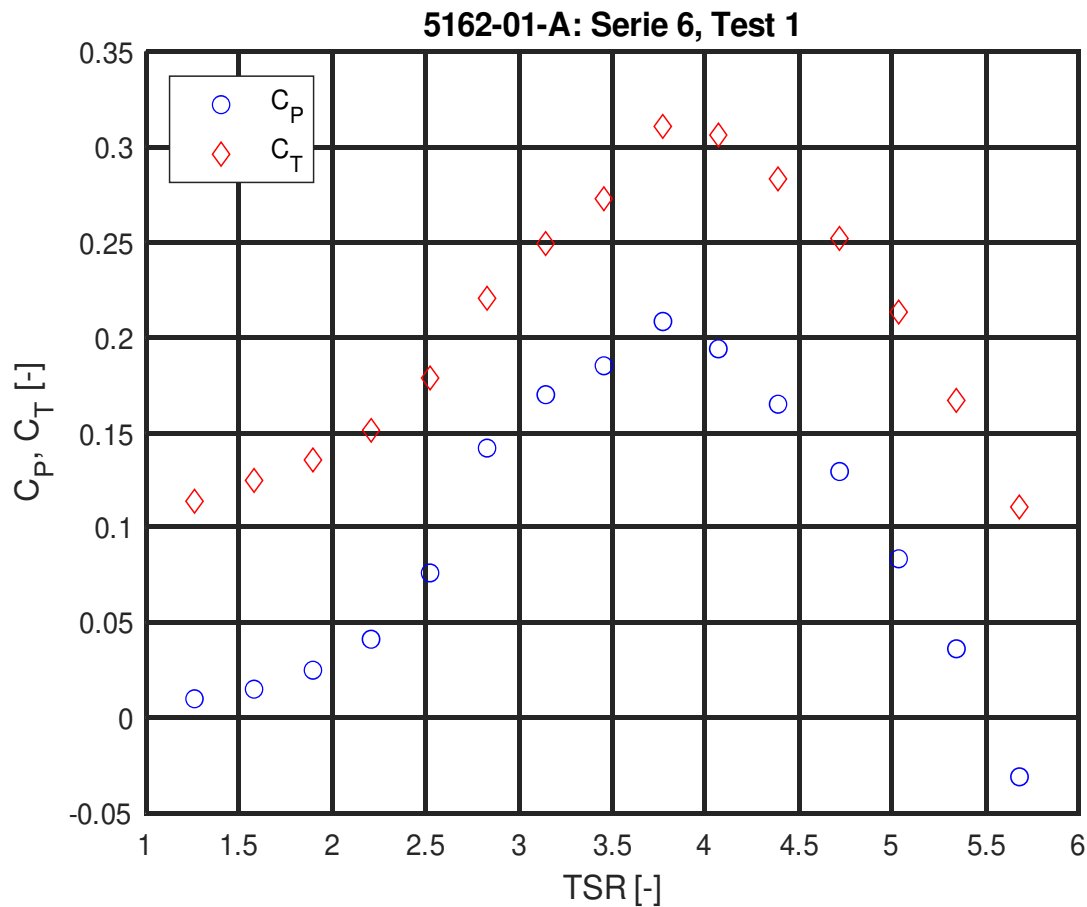


Figure 73: $\alpha = 10$, $\beta = 0$, $P_0 = 220 \text{ kPa}$

Surface roughness modelling

The analysis reported in this section aims to (i) assess the impact of blade surface micro-texturing on the airfoil hydrodynamic characteristics, (ii) determine whether the high fidelity LES strategy should be adapted to account for surface roughness and (ii) determine how this should be done if relevant.

Methodology

The assessment is based on a two dimensional (2D) computational analysis of turbulent flow over a single blade section. The section selected is slice S9 of chord length $C = 0.72 \text{ m}$. It is located at 8 m radial position that is at 84% of the turbine radius where a significant part of the useful torque is generated but sufficiently far from the blade tip to limit three dimensional flow structure. The airfoil

was simulated at a tidal stream velocity of 2.5 m/s and a turbine rotational speed of 16.8 rad/s , giving a tip speed ratio of 6.7 and an Angle of Attack $AOA = 5.46^\circ$. The flow characteristic Reynolds number evaluated at the airfoil trailing edge is $Re = 8.88 \times 10^6$. The computed wall unit ranges from a minimum of $1 \mu\text{m}$ after transition on the suction side to $4.8 \mu\text{m}$ near the trailing edge again on the suction side and the turbulent Reynolds number Re_τ measured in terms of the chord length varies from 5×10^4 to 3.5×10^5 . The wall boundary is meshed to resolve the viscous sublayer with a maximum cell to wall distance in wall units y^+ less than 1 while keeping the streamwise cell length uniform and equal to 1 mm . The resulting mesh is shown in Figure 74 with the insert focusing on the wall region near the leading edge.

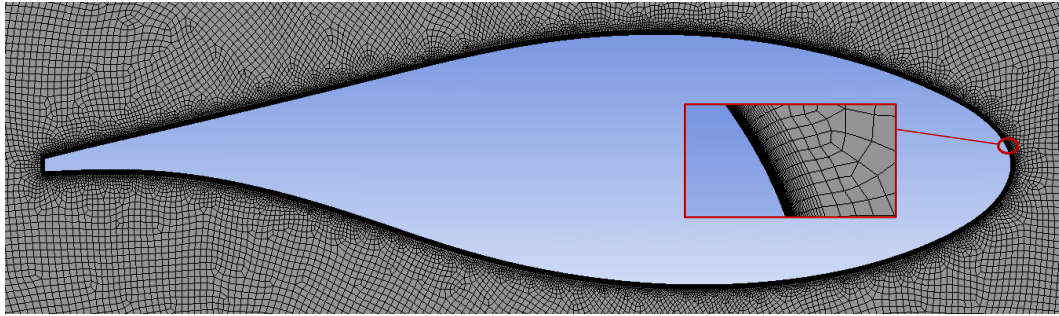


Figure 74 Quad dominant mesh of 2D turbine blade section at radial position of **8m**

The blade is embedded in a circular domain with a diameter to chord ratio of 80. The four equation transitional $k-\omega$ SST model (Menter, Menter, Langtry, & Volker, 2006) of ANSYS Fluent version 2019 (ANSYS, 2019) was used for turbulence modelling and account for boundary layer transition.

Surface roughness is known to alter the turbulent energy production cycle when the roughness height is greater than a few wall units. This wall unit δ_v is the length scale which characterizes flow in the inner part of the wall boundary layer. It is defined from the fluid molecular kinematic viscosity ν and the velocity scale $u_\tau = \sqrt{\tau_w/\rho}$, where τ_w is the wall shear stress and ρ the fluid density, with $\delta_v = \nu/u_\tau$. Normalization with this wall unit is denoted with the superscript $+$. When $k^+ > 3.5 - 4$, the roughness structure protrudes into the buffer layer above the viscous sub-layer. This region extending into the so-called logarithmic layer at $y^+ \approx 100$ is known to sustain most of the turbulent cycle. It has been shown from pipe flow experiments by Nikuradse (Nikuradse, 1933), that surface roughness preserves this logarithmic part of the law for smooth walls. The main effect of increased roughness is an increase in wall shear stress and a corresponding increase in the friction velocity u_τ along with a downward shift in the logarithmic law of the wall. This shift can be accounted for with a velocity deficit ΔU^+ . The resulting modified log-law defines the mean flow velocity in the streamwise direction U^+ as a function of the wall normal position y^+ :

$$U^+(y^+) = \frac{1}{\kappa} \ln y^+ + B - \Delta U^+(k^+) \quad (1)$$

where the von Kármán constant $\kappa = 0.42$ and the additive constant $B = 5.2$ are unchanged from the smooth wall log-law. In the fully rough regime ($k^+ > 70$), the velocity deficit can be shown to correlate to the sand roughness k_s^+ of Nikuradse's experiments but also to a so-called equivalent sand

roughness height $k_{s,eq}^+$ for a range of geometrical or irregular roughness types. $k_{s,eq}$ is not known a priori. It may be determined from Direct Numerical Simulation of the turbulent flow or experiments by scaling the surface roughness expressed in wall units k^+ . The scaling factor is determined so that the velocity deficit ΔU^+ fits the Colebrook correlation in the fully rough region. Measurements must be performed at high roughness Reynolds number $k_{s,eq}^+$ over a range of values to confirm the asymptotic fit. The correlation is defined by Eq. 2 and illustrated in Figure 75.

$$\Delta U^+ = \frac{1}{\kappa} \ln (1 + 0.26 k_{s,eq}^+) \quad (2)$$

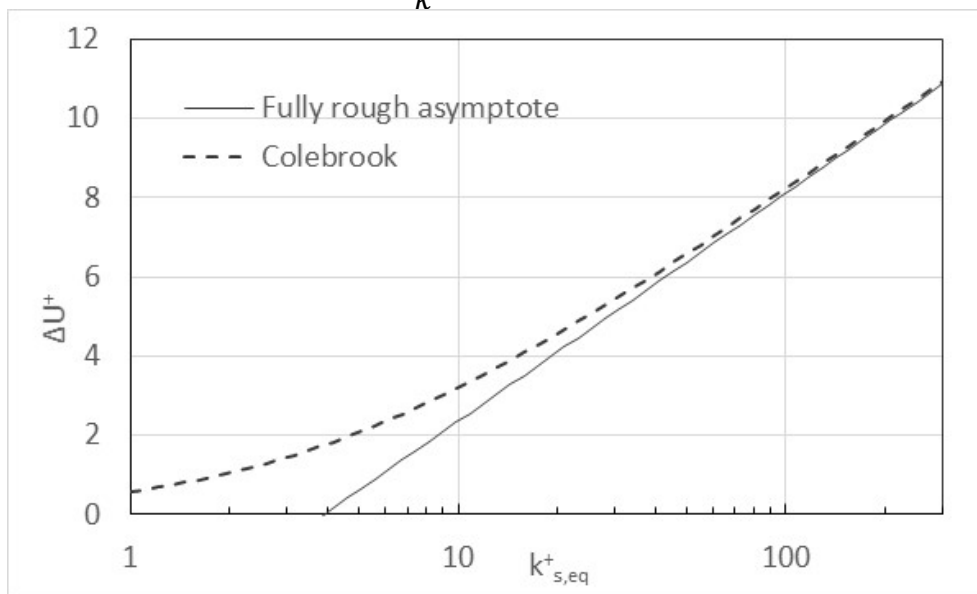


Figure 75 Velocity deficit correction to account for surface roughness as a function of the equivalent sand roughness height in viscous units.

This approach assumes that k_s is indeed proportional to the dimensions of the roughness element k . This is the case for the so-called k -rough surfaces for which k_s/k correlates to the solidity λ defined as the total projected frontal roughness area per wall-parallel area of the smooth surface. Not surprisingly k_s/k increases with the solidity when distributed sufficiently sparsely for the roughness elements to induce form drag in proportion to the height. When the solidity increases beyond approximately 0.15, the trend is inverted as roughness elements shelter each other (Jiménez, 2004).

When the roughness involves narrow spanwise grooves, the surface is categorized as a d -rough surface, for which k_s is no longer proportional to k . If the groove width (length in the streamwise direction) is larger than $3 - 4k$, k -roughness is recovered otherwise the roughness elements isolate stable recirculating flow in the grooves. The groove depth, that is the roughness element height no longer influences the outer flow and k_s no longer scales with k . It has been proposed that k_s could be proportional to the boundary layer thickness δ for zero pressure gradient flow. It was suggested that this could be explained by the occasional ejection of vorticity from the grooves into the outer flow triggered by large scale sweeps from the outer flow but (Jiménez, 2004) provides evidence that a scaling with this outer unit is not generally verified.

Several correlations have been proposed to determine the equivalent sand roughness taking into account the roughness element geometrical characteristics and density. There is evidence however

that these produce significant variability. All correlations are based on composite functions determined to cover the different flow regimes (smooth, transitional and fully rough). A key uncertainty relates to the threshold which determine transitional roughness. Many engineering surfaces are considered smooth up to $k^+ \approx 3.5 - 4$, but significant variability has been reported. This figure may be smaller as predicted by Eq. 2 or larger for example with streamwise aligned triangular riblets (Bechert, Bruse, & Hage, 2000). Most important for the current study is the fact that no correlation covers the three dimensional roughness types considered.

The roughness structures proposed in WP 3 as an antifouling strategy, are based on arrays of elongated rectangular bars or cavities as illustrated in Figure 76. Although seemingly similar, the roughness type may be very different:

- The cavity design, is made of rectangular constant depth grooves etched into a flat surface. The groove width as defined in the context of d -roughness refers here to the length of the cavity in the streamwise direction noted L_x . The cavity depth L_y is the roughness height. The width of the ridges between successive cavities is $w = 10\mu m$ and is unchanged in the spanwise and streamwise directions. The proposed dimensions are determined by a mixture of factors related to biofouling, structural rigidity and wear. The ridge width must be as close as practically possible to $10\mu m$ or lower to effectively disrupt the settlement and growth of micro-organisms. It is desirable to increase the streamwise length L_x to improve structural rigidity of the ridges and reduce machining requirements. At the same time a longer cavity, increases the likelihood of recovering a k -roughness when $L_x > 3L_y$ which could result in an increase in form drag due to the transverse ridges. For the proposed length of $L_x = 85\mu m$, a height of at least $L_y = 30\mu m$ would preserve d -roughness if the groove was two dimensional. An alternative to avoid any significant impact of the roughness on surface induced drag would be to reduce the texture height as close as possible to the smooth regime threshold. At the tip of the NEMMO blade a strict application of the threshold would require a texture height below $4\mu m$ everywhere, a value which is too close to the natural variations of the smooth surface. Surface height measurement of 12 samples indicated a maximum peak to mean difference of $4.8\mu m$.
- The raised rectangular bars are based on the same individual roughness element size and geometry but the elements are added to the smooth surface rather than being recessed. This creates fundamentally different flow as the groove width as defined in the k -roughness terminology is the gap width $w = 10\mu m$ rather than L_x . Strictly speaking the texture cannot be considered a d -roughness due to the intrinsically three dimensional arrangement. If the elements are aligned with the streamwise direction, the texture is made up of continuous streamwise channels interspaced with finite pseudo d -roughness structures with small groove width to depth ratios in the range $w/L_y = [10/30, 10/10]$.

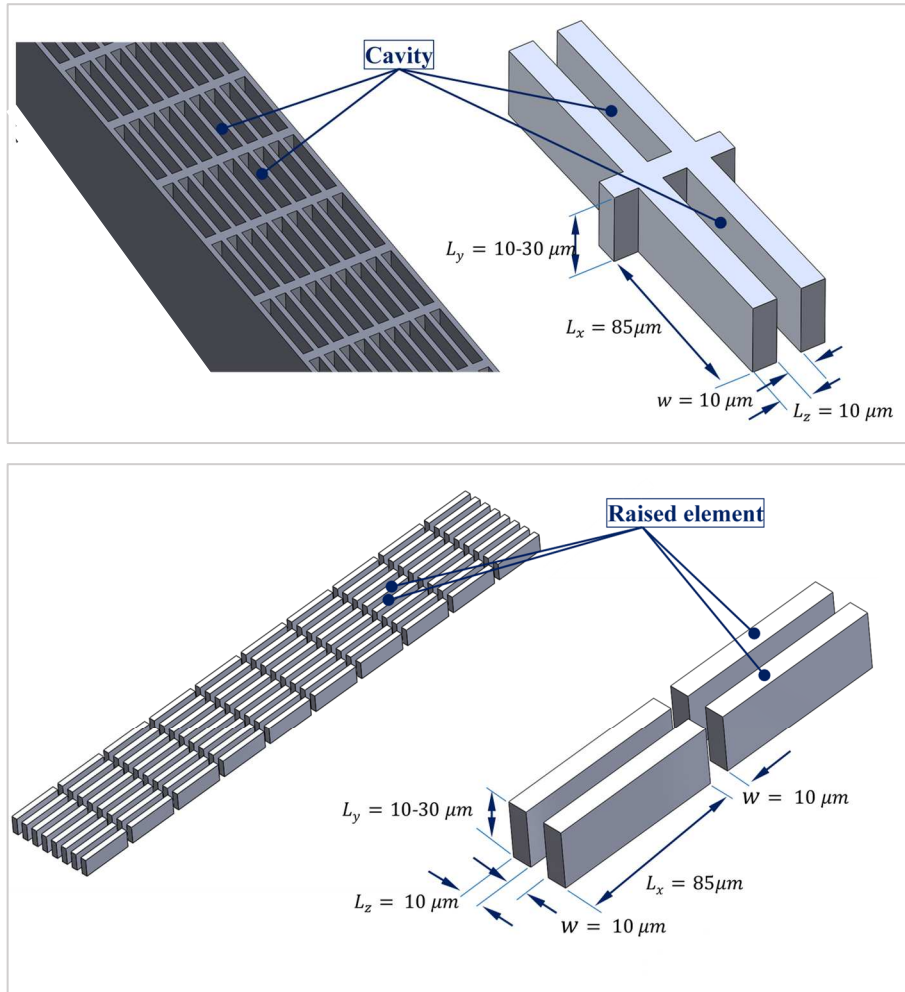


Figure 76 Outline sample micro-textures. [Top] Recessed cavity design. (L_x , L_y , L_z) refer to the cavity size while w is the ridge width. [Right]: Raised rectangular bar. (L_x , L_y , L_z) refer to the bar size while w is the groove width in both spanwise and streamwise directions. Dimensions are indicated with reference to the streamwise, spanwise and wall normal coordinates, written (x , y , z) respectively.

Four alternative antifouling designs will be considered in this study. L_x and L_z are prescribed as per Figure 76 but two alternative cavity depths or raised element heights of $L_{y_1} = 10 \mu\text{m}$ and $L_{y_2} = 28 \mu\text{m}$ will be studied for each design as part of the antifouling performance analysis of WP3. L_{y_1} and L_{y_2} define the geometric roughness height k and the two heights considered correspond to $L_{y_1}^+ = 7$ and $L_{y_2}^+ = 20$ at the wall stress $\tau_w = 500 \text{Pa}$ predicted at the mid-cord on the suction side of the NEMMO airfoil Section S9 under nominal operating conditions. The correlation proposed by Sigal and Danberg (Sigal & Danberg, 1990) and defined by Eq. 3 for 3D roughness estimates the equivalent roughness written hereafter as k_s as $k_s = 2.6 \times 10^{-2} \mu\text{m}$ and $k_s = 0.46 \mu\text{m}$ for the raised structure with heights $k = 10 \mu\text{m}$ and $k = 28 \mu\text{m}$ respectively. These low values place the roughness well within the viscous sub-layer. It should be noted however that the two roughness elements are outside the range of applicability as measured by the roughness parameter Λ which must be in the range $[16, 200]$. $\Lambda = (S/S_f)(A_f/A)^{-1.6}$ accounts for roughness density (S/S_f) and shape (A_f/A) where S is smooth surface area, S_f is the total frontal area of all roughness elements, A_f is the frontal area of a single element and A is the wetted area of a single element.

$$k_s/k = 160.77\Lambda^{-1.3376}, 16 \leq \Lambda \leq 200 \quad (3)$$

The correlation is not directly applicable to the cavity design but if the cavity end wall are considered as the roughness element, the corresponding equivalent roughness would be $k_s = 1.6 \mu m$ and $k_s = 55 \mu m$. A more suitable alternative may be to consider the cavity as a 2D transverse series of grooves by neglecting the effect of longitudinal ridges, in which case the 2D roughness correlation due to Sigal and Danberg and given by Eq. 4 predicts the equivalent roughness $k_s = 9.4 \mu m$ and $k_s = 172 \mu m$ for the cavity depth $k = 10 \mu m$ and $k = 28 \mu m$. Both approaches suggest moderate impact from the shallower textures but very significance increase in the equivalent roughness for the deeper grooves. If verified this would have a significant impact on performance and cannot be justified.

$$k_s/k = \begin{cases} 0.003215\Lambda^{-4.925} & , 1.4 \leq \Lambda \leq 4.89 \\ 8 & , 4.89 \leq \Lambda \leq 13.25 \\ 151.71\Lambda^{-1.1379} & , 13.25 \leq \Lambda \leq 100 \end{cases} \quad (4)$$

Estimates of the equivalent roughness height from correlations alone cannot provide any degree of certainty on appropriate values of the equivalent sand roughness to modify wall boundary conditions. A two-step strategy is adopted to address this.

First a k_s sensitivity analysis is performed with a view to:

- better understand the effect of the micro-textures on the wall mean flow conditions,
- quantify the impact of the micro-texture on the turbine blade performance measured in terms the lift and drag coefficients for the turbine blade at section S9,
- estimate the equivalent sand roughness which will produce the best fit with experimental data from 2D blade section testing.

Second, high fidelity LES simulations of channel flow with textured surface will be performed to evaluate k_s .

Results

k_s sensitivity analysis

The rough wall treatment implemented with the transitional turbulence model involves two modifications to traditional wall modelling. Roughness is accounted for in terms of its effect on transition and through boundary conditions for the turbulent kinetic energy k , the specific dissipation rate ω and the wall shear stress. The former relies on a correlation for a modified rough transition momentum thickness Reynolds number $R\bar{\epsilon}_{\theta_t}$ which requires the geometric roughness height (ANSYS, 2019) while the latter is defined from an equivalent sand roughness height. With these rough wall modifications to the boundary conditions for the turbulent quantities k and ω , hydraulically smooth regime is recovered below $k_s^+ = 2.25$.

The equivalent sand roughness heights considered in this sensitivity analysis covers a range starting at and just above this hydraulically smooth threshold that is $0 \mu m$ and $3 \mu m$ and extending to the larger micro-texture proposed $28 \mu m$. The intention was to cover the range predicted by the Sigal and Danberg correlations. Estimates place k_s well below the transitional threshold for the raised micro-textures. The cavity design on the other hand shows large variability with values of k_s as low as the geometric cavity height of $10 \mu m$ to much larger values. The largest equivalent roughness considered was effectively capped at the actual geometric roughness height of $28 \mu m$. The set of values tested is compared to correlation estimates in Table 11.

Table 11 Estimates and tested equivalent roughness heights included in sensitivity analysis.

		k_s [Eq. 3]	k_s [Eq.4]	k_s
Cavity Design	$k = 10 \mu m$	$k_s = 1.6 \mu m$	$k_s = 9.4 \mu m$	$\{0,3,5,10,20,28\} \mu m$
	$k = 28 \mu m$	$k_s = 55 \mu m$	$k_s = 172 \mu m$	
Raised Design	$k = 10 \mu m$	$k_s = 0.026 \mu m$	–	$\{0,3,5,10,20,28\} \mu m$
	$k = 28 \mu m$	$k_s = 0.46 \mu m$	–	

All simulations were performed with inlet turbulent conditions defined in terms of the Turbulent Intensity (TI) and Integral Length scale of turbulence (L_t). Conditions tested ranged from relatively low level turbulence with $(TI, L_t) = \{ (5\%, 0.1m), (5\%, 2.5m) \}$ to more realistic conditions based on measurements taken at a proposed tidal energy site at the Sound of Islay, Scotland, in $55m$ water depth and at a location $5m$ from the sea bed (Milne, Sharma, Flay, & Bickerton, 2013). The maximum tidal stream velocity at spring tide for that location is $2.5 m/s$. Measurements from two complete tidal cycle near spring tide gave streamwise Turbulence Intensity during non-slack flow in the range $[12 - 13\%]$. At maximum flow the Length scale L_t was in the range $[11,14m]$. The reference conditions considered in the study reported here are $TI = 12\%$ and $L_t = 15m$. The low turbulence conditions were included to test the impact of micro-textures under more sensitive conditions where small changes in roughness can induce larger variations in the transition to turbulence.

Not surprisingly, the inlet turbulence can have a significant impact on the wall shear stress distributions in part through its impact on boundary layer transition. The initial laminar boundary layer growth contributes to a decrease in wall stress in the vicinity of the airfoil leading edge. Transition to turbulence is associated to a sharp rise in wall shear stresses. The stress distributions of Figure 77 shows how the laminar region rapidly reduces with increased inlet turbulence. This affects both suction (side with higher stresses) and pressure sides. At the higher free stream turbulence of the reference state, the laminar part vanishes entirely. The effect is associated to higher pressure on both sides of the airfoil but the effect is most pronounced on the suction side.

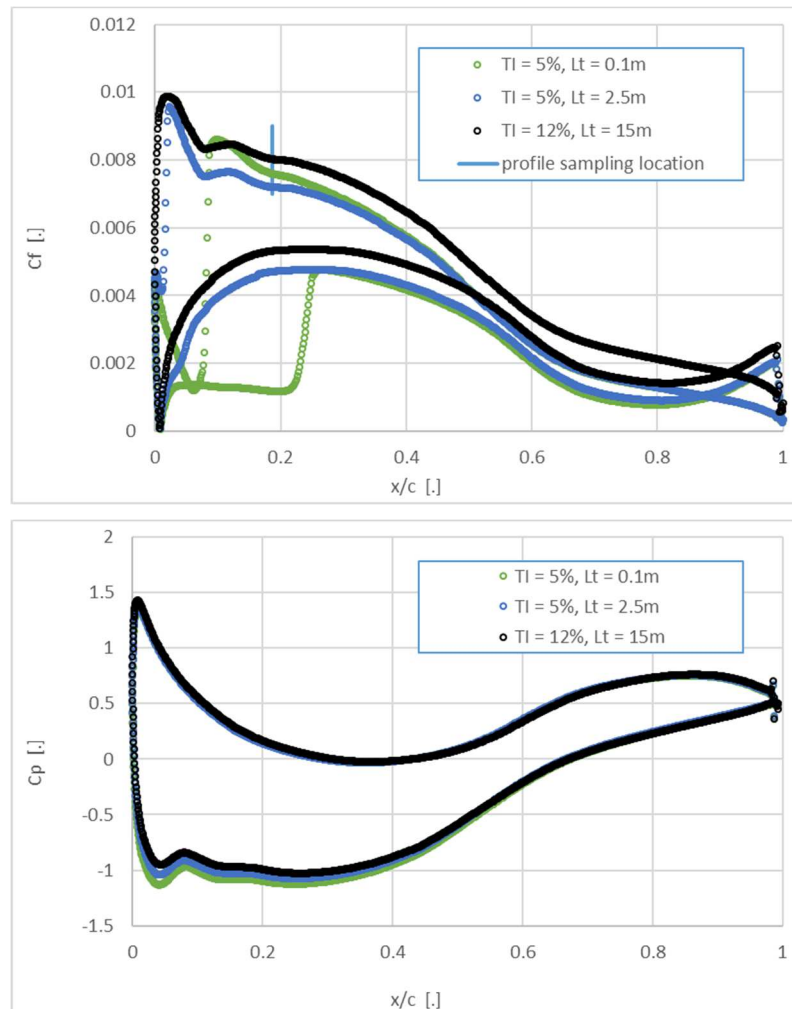


Figure 77 Stress distribution over airfoil blade section S9 modelled with smooth wall boundaries for three inlet turbulent conditions. [Top] Coefficient of wall friction. The vertical blue line indicates the location of the line used to sample the inner boundary in Figure 78. [Bottom] Coefficient of pressure

A sample boundary layer velocity profile taken on the suction side after transition at $x/c = 0.1875$ is shown in Figure 78. At that point, the flow experiences a favorable pressure gradient due to surface curvature. The velocity profile is nonetheless shown to follow largely the law of the wall covering the viscous, buffer and inertial layers, confirming the suitability of the mesh and turbulence model to resolve the boundary layer.

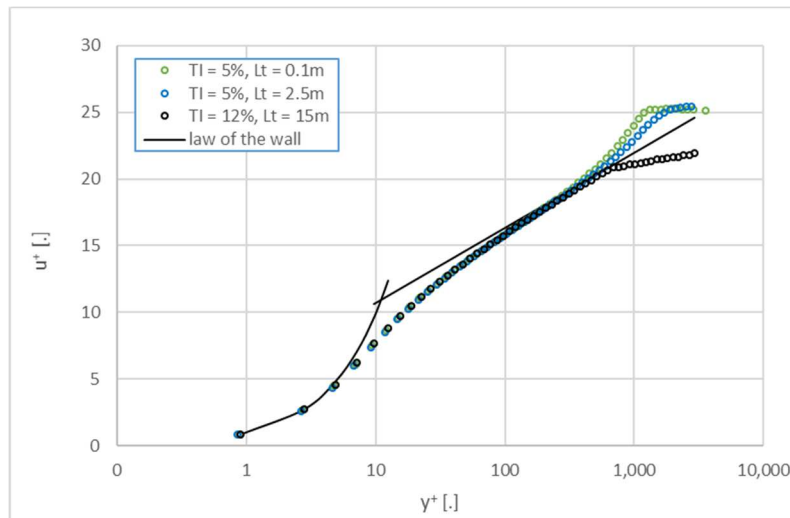


Figure 78 Velocity profile in inner part of the boundary layer along sampling line defined in Figure 77

One of the most significant effects of the increase in free stream turbulence is a significant drop in pressure gradients on the suction side near the region of highest acceleration towards the leading edge. This is then followed by a drop in the strength of the suction effect over much of the active part of the airfoil. A similar effect is observed with the addition of surface roughness models. Higher equivalent sand roughness k_s and geometric roughness k are typically found to both reduce the overall lift which is due mostly to pressure. This again is not surprising given the impact of roughness on turbulent energy production.

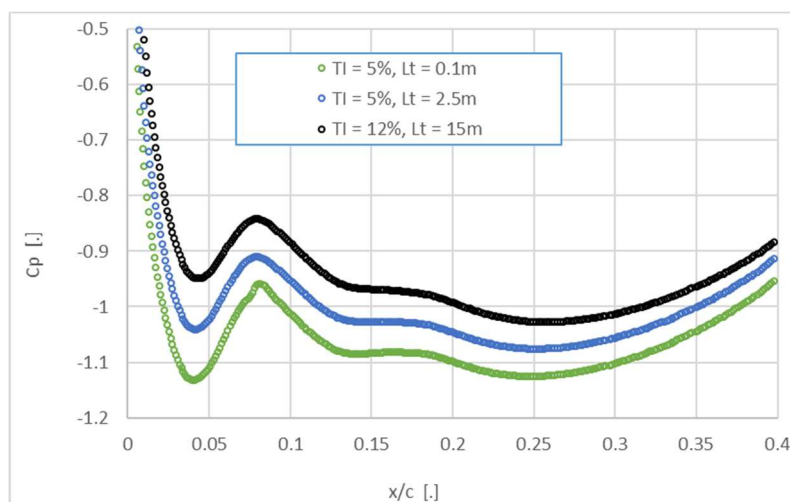


Figure 79 Close up view of pressure coefficient on suction side of the airfoil towards the leading edge.

The effect of surface roughness on the inner velocity profile is illustrated in Figure 80. These results refer to the freestream turbulence from the reference case which produces fully turbulent boundary layer flow over the full surface of the airfoil. A single geometric roughness height $k = 28 \mu m$ is shown here but broadly similar results are obtained with other conditions tested. The expected downward velocity shift associated with increased wall stress is clearly reproduced in the non-dimensional profile. The profiles from the three lower values of k_s collapse on a single curve. It should be noted that this is not the case with the smaller geometric roughness $k = 10 \mu m$ for which a higher sensitivity to k_s is observed over the full range studied. The boundary layer is shown in Figure 81 to

thicken with the equivalent roughness which may explain the reduction in pressure gradients if it results in lower effective curvature of the edge of the outer boundary layer.

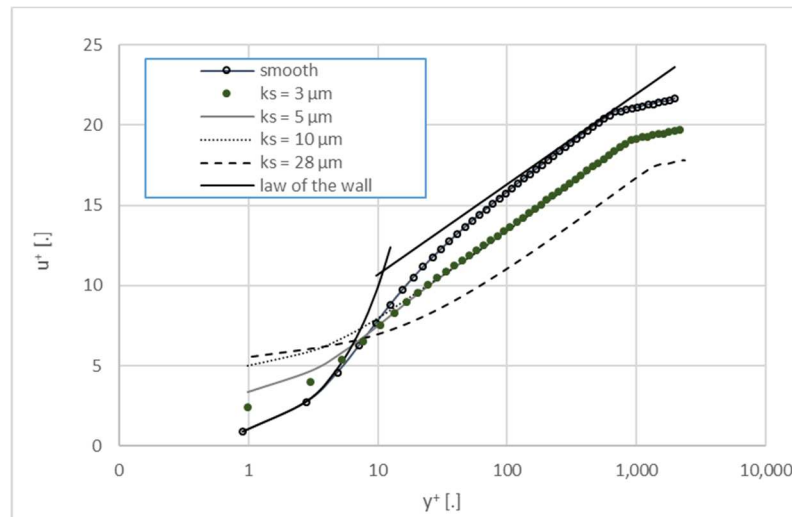


Figure 80 Boundary layer velocity profile viscous units along sample line on suction side for reference turbulence conditions $TI = 12\%$ and $L_t = 15m$ with a geometric roughness $k = 28 \mu m$.

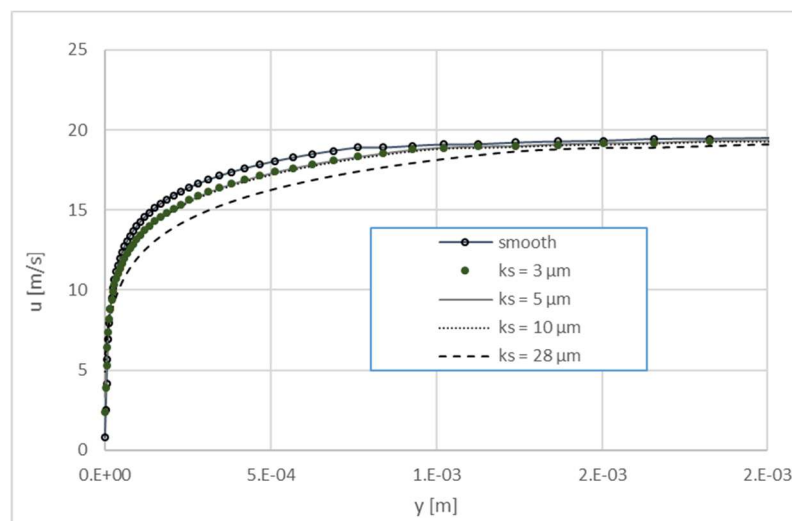


Figure 81 Dimensional boundary layer velocity profile along sample line on suction side for reference turbulence conditions $TI = 12\%$ and $L_t = 15m$ with a geometric roughness $k = 28 \mu m$.

An overview of the roughness effects is now presented in terms of changes to the coefficients of lift and drag, both important hydrodynamic performance indicators for the turbine. The results are shown with respect to the smooth wall predictions at the reference turbulence in Figure 82 and with respect to the smooth wall conditions for each turbulent conditions in Figure 83. In all cases higher equivalent roughness and geometric roughness increases drag and reduces lift. The effects are gradual in all cases except one with the medium turbulence ($TI = 5\%$, $L_t = 2.5m$), $k = 10 \mu m$ and $k_s = 28 \mu m$ when the increased roughness triggers an early transition to turbulence in the boundary layer.

From Figure 83, the roughness settings are clearly shown to have an important effect for any of the turbulence conditions tested. At artificially low turbulence, the effect is exacerbated but remains

moderate at the reference conditions with single digit percentage increase in drag with a maximum of 8% at the larger $(k, k_s) = 28 \mu m$. The corresponding increase in lift compared to the smooth results is smaller at approximately 3.4%. These results suggest that a shallower texture would not be expected to decrease lift by more than 1-2%. From Figure 82, it is also evident that the free stream turbulence has a major bearing on the impact of texturing. It should however be noted once again that the low turbulence results are provided for comparison purposes and are not expected to be representative of real sea conditions.

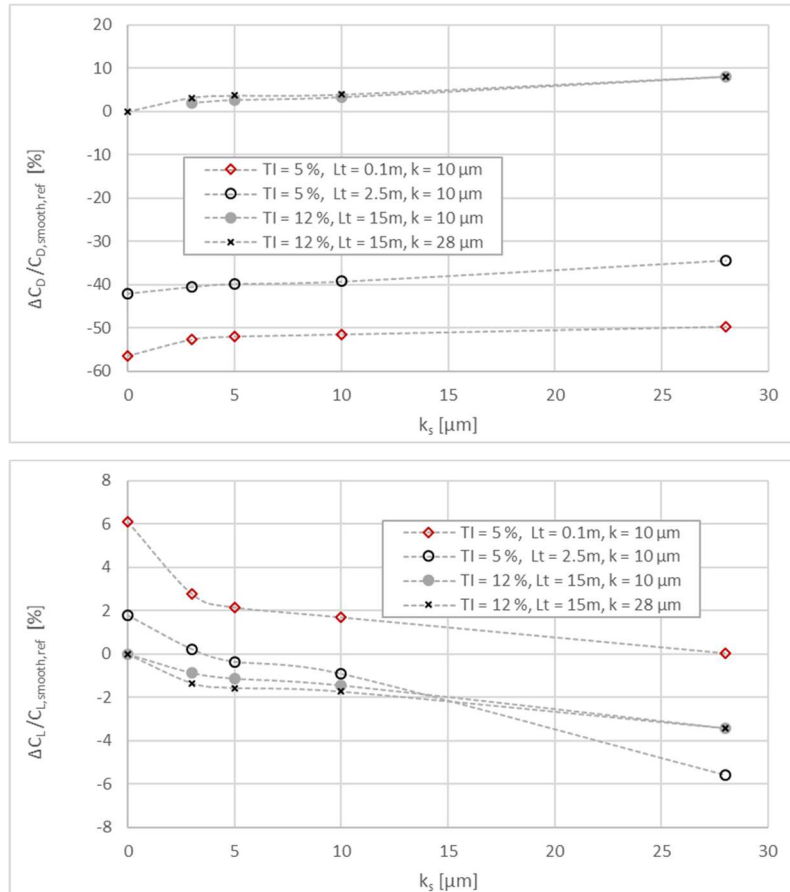


Figure 82 Relative change in the hydrodynamic coefficients with respect to the reference turbulence conditions and the smooth wall ($k_s = 0$). [Top] Coefficient of drag. [Bottom] Coefficient of lift.

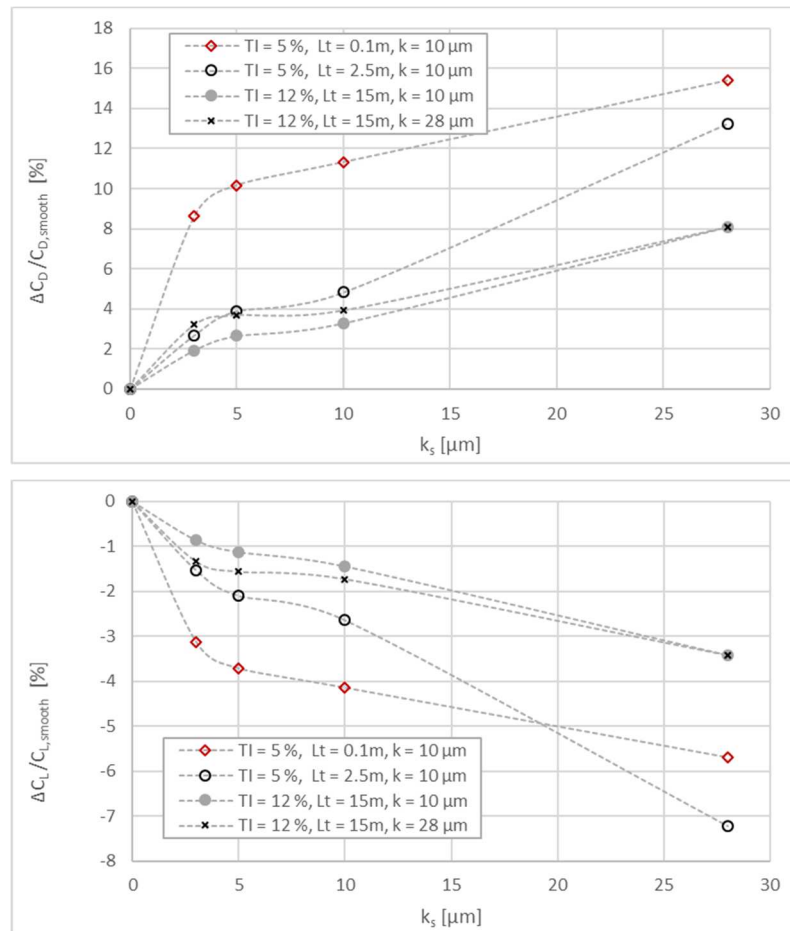


Figure 83 Relative change in the hydrodynamic coefficients with respect to the smooth wall ($k_s = 0$) only. [Top] Coefficient of drag. [Bottom] Coefficient of lift.

It is worth noting that the geometric roughness height used in the correlation for the modified rough transition momentum thickness Reynolds number $R\tilde{e}_{\theta_t}$ in the transitional model has a more moderate effect on drag and lift once the inlet turbulence is sufficiently high to produce fully turbulent boundary layers over the full airfoil. This indicates that the primary concerns in realistic flow condition is to determine the appropriate equivalent sand roughness height k_s .

LES estimates of effect of texture on wall shear stress

The analysis reported in this section aimed to estimate the equivalent surface roughness for the two structure types presented in Figure 76. A simulation based approach has been adopted. This required resolving the micro-textures and their impact on the turbulent flow. The task is particularly challenging due to the relatively high Reynolds number flow studied. The main difficulty relates not just to the mesh size but also to long averaging period needed to accurately capture higher order moments of turbulence.

Methodology

The solution presented relies on LES simulations of turbulent channel flow following the methodology presented in Deliverable D3.2. The key steps are summarized below:

- Simulate the unsteady channel flow until turbulence properties reach a steady state. The coarser mesh M1 defined and assessed in section 3.2.3 of Deliverable D3.2 is used to produce these precursor fully turbulent channel flow.
- Modify the bottom surface of the periodic channel to incorporate the textures over its full surface as illustrated in Figure 84 with the recessed cavity and raised structures.
- Restart the LES simulations after mapping of all flow variables from the smooth channel flow simulations and continue until steady state.
- Perform a time averaging to provide the turbulent first order moments and determine the roughness function ΔB which characterises the downward shift in the law of the wall and is needed to estimate the equivalent non-dimensional sand roughness $k_{s,eq}^+$ from Eq. (1).

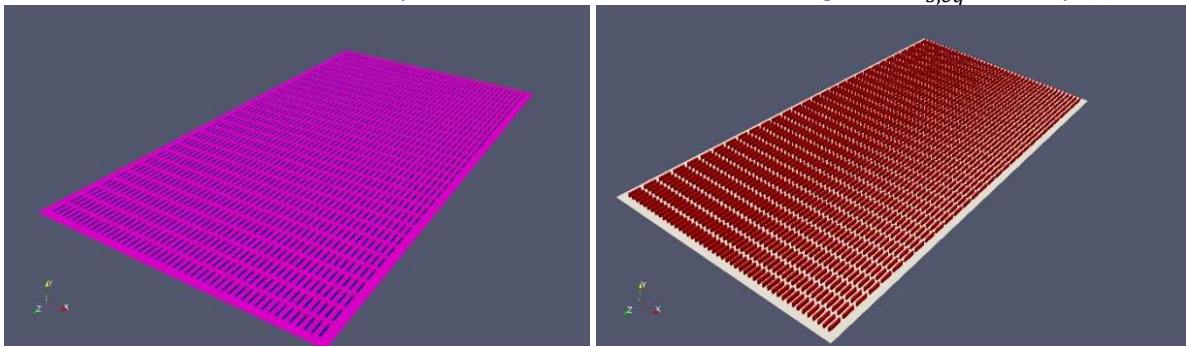


Figure 84 geometry of full surface covered with the [Left] recessed cavities and [Right] Raised textures

Recessed cavities

The mesh refinement required to capture the vortical flow structures between features were established by reference to a published study of span-wise 2D rib like features (Cui, Patel, & Lin, 2003). The present recessed cavities are made of rectangular grooves with the same geometric features in the stream-wise direction but extending only over a limited length in the span-wise direction. These interrupted grooves will partially suppress the cavity flow but similar flow features can nonetheless be expected. For the pitch to height ratio considered here (where the pitch is distance between two consecutive roughness to include the length of roughness in stream-wise direction), the roughness can be categorized as a intermediate k-type with two main vortices forming in the cavity as illustrated in Figure 86. A minimum of 20 cells would be required in stream-wise and span-wise directions to resolve these flow features (Leonardi, Orlandi, Smalley, Djenidi, & Antonia, 2003). For the textures considered here this was shown to generate in the region of five million cells in the cavities alone and a minimum of 15.5 million cells in the overall domain. In addition the use of cubic cells lead to a significant reduction in the stream-wise length of mesh cells and a corresponding increase in Courant number (Co) necessitating smaller time steps. Increased mesh and reduced time step combined with the need for a long averaging period to achieve statistically steady turbulence, create a load task which is well beyond the capability of the High Performance Computing resource currently allocated to the project. Instead meshing in the cavity was based on 8, 2 and 5 cells in the stream-wise, span-wise and wall normal directions respectively. In addition the gap between the cavities has been increased to $\Delta z^+ \cong 17.6$ instead of the target $\Delta z^+ \cong 7$ to reduce the number of textures. The rest of the domain is meshed so that y^+ is less than 2 at the top of the texture generating 4.1 million cells overall. A time step equal to 0.01s was chosen to keep the $Co < 1$. The non-dimensional velocity profile obtained with the textured surface is compared to the equivalent smooth wall solution in Figure 87.

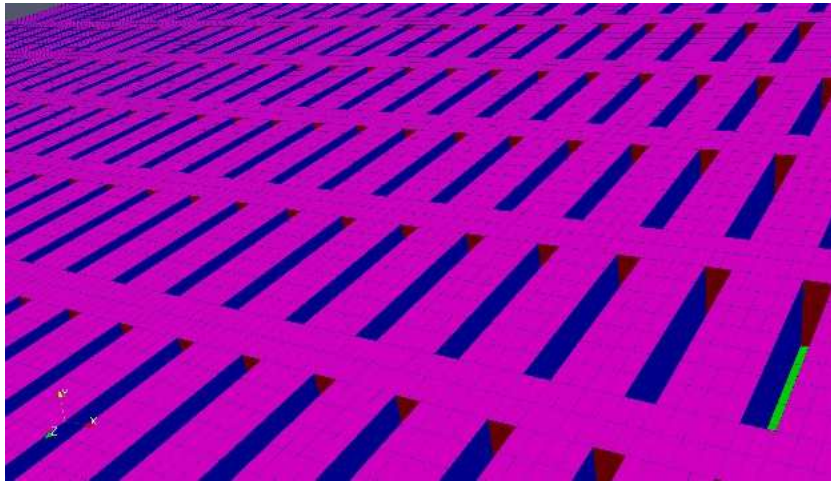


Figure 85 Surface mesh above the recessed cavity.

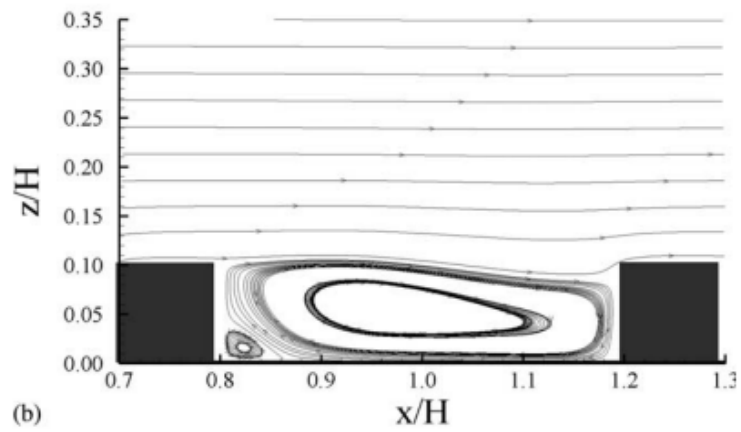


Figure 86 streamline patterns for a semi k-type 2D roughness. (Leonardi, Orlandi, Smalley, Djenidi, & Antonia, 2003)

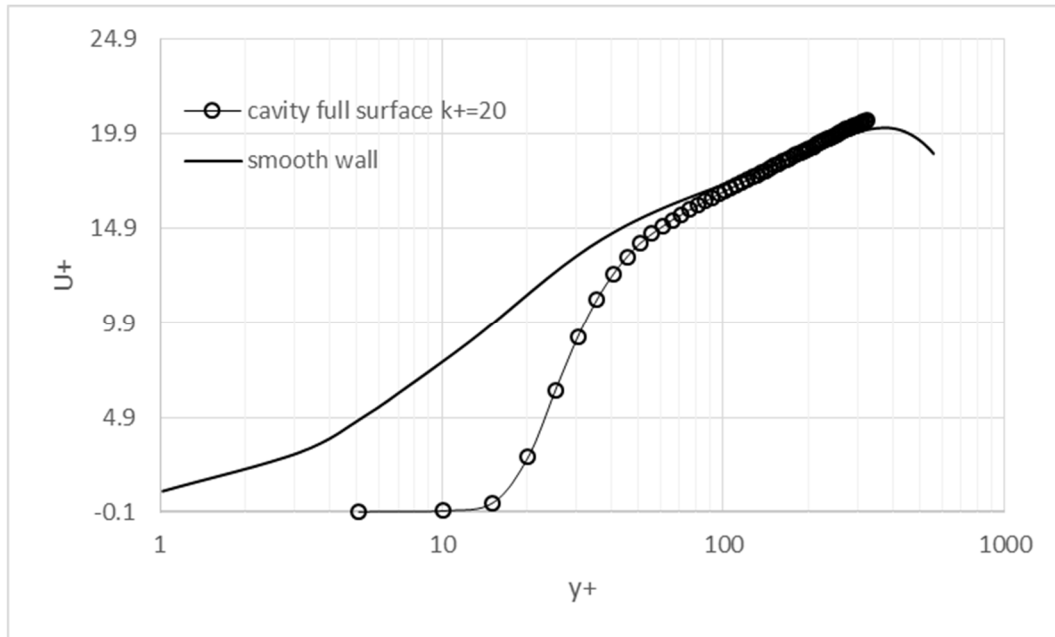


Figure 87 Non-dimensional velocity profile of full cavity vs smooth wall solution. The textures considered here are the recessed cavity with cavity depth $k^+ = 20$ which corresponds to approximately $28\mu\text{m}$ at the flow conditions expected over Section 9 of the NEMMO turbine blade.

These results indicate a minimal impact of the textures on the shear stress at the wall. The roughness function is determined from the correlation by Cebeci and Bradshaw (1977) (Cui, Patel, & Lin, 2003) :

$$\Delta B = \Delta U^+ = (B - 8.5 + \kappa^{-1} \ln k_{s,eq}^+) \times \sin[0.4825(\ln k_{s,eq}^+ - 0.811)] \quad (5)$$

Where, $2.25 < k_{s,eq}^+ < 90$. If ΔB is evaluated at the lower limit of $k_{s,eq}^+ = 2.25$, the downward shift should be $\Delta B = -3.3$. The velocity profile given in Figure 87, suggest a shift that could be smaller in which case the textures can be ignored in terms of their impact on flow. This is an unexpected result if compared with the profile the intermediate k-type texture profile shown in Figure 88. It is undeniable however that the three dimensional nature of the textures could also explain the results. The actual coverage ratio by the gap is much smaller than would be the case with a 2D texture which may explain the much smaller impact.

It must also be stated that the results were obtained with a relatively coarse mesh. Although the mesh resolution outside of the cavity did resolve key trends and features for both the first and second moments of turbulence it was not sufficient to predict the wall stress accurately (Mesh M1). The cavities are also poorly resolved.

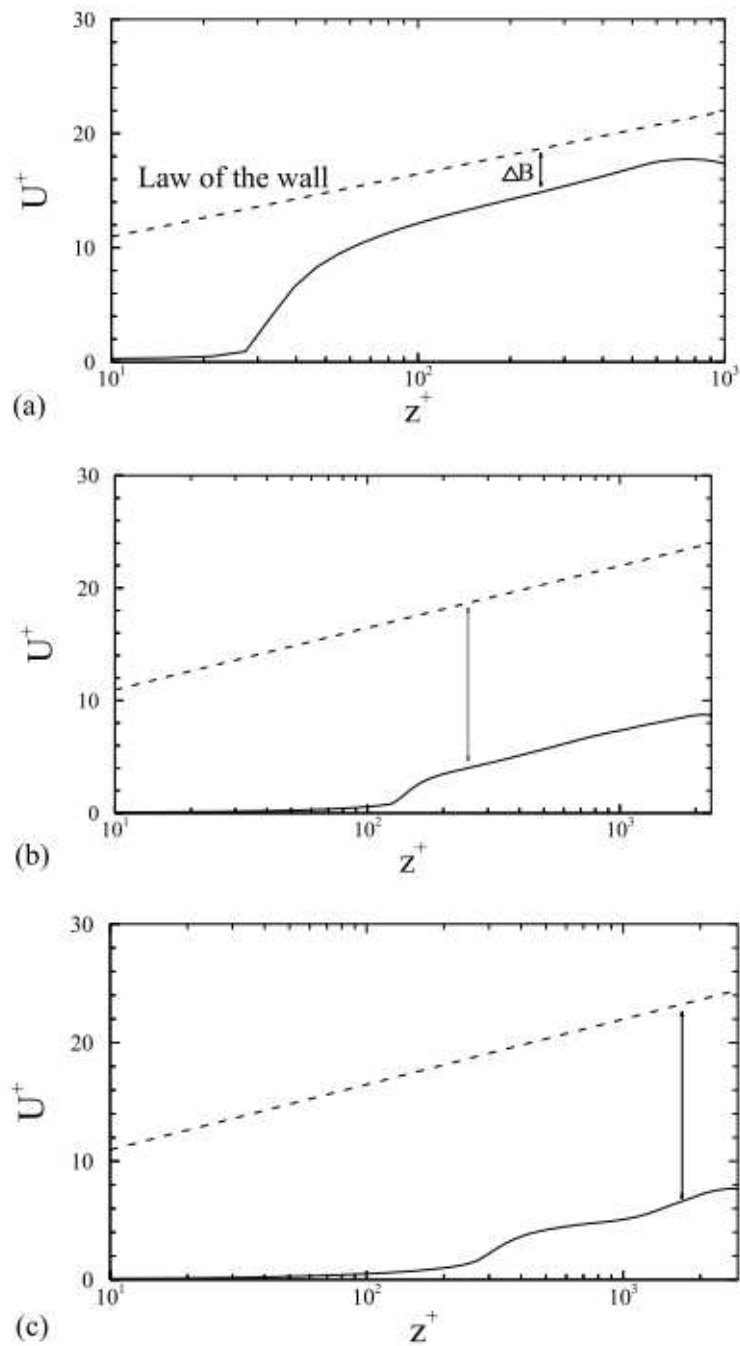


Figure 88 Non-dimensional velocity profile over rough surface compared to the smooth law of the wall to illustrate the downward shift ΔU^+ for (a) d-type b) intermediate k-type and c) k-type roughness from (Leonardi, Orlandi, Smalley, Djenidi, & Antonia, 2003).

Raised structures

The same meshing strategy as discussed for the recessed cavities has been adopted in this case leading to a similar mesh count as illustrated in Figure 89. For flow aligned with the texture length two effects can be expected: (i) an upward shift of the quasi-stream-wise vortices leading to effective thickening of the viscous sub-layer (Jiménez, 2004) and (ii) the formation of trapped vortices in the cavity between successive protrusion in the stream-wise direction. While the latter is known to induce a moderate increase in the wall shear stress associated to so called d-type roughness shown in Figure 90, the former is associated to the drag reduction effects. The downward shift in the log profile is shown in Figure 91 for a range of k-type roughness as a function of k^+ . A negative shift corresponds to drag reduction which is observed in this figure with triangular riblets in their hydraulic transitional state between the smooth and fully rough regimes that is for $2 < k^+ < 8$.



Figure 89 Surface mesh over the raised textures.

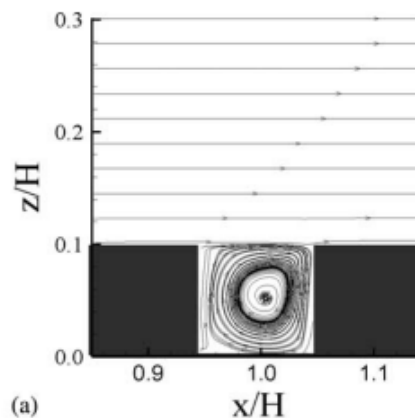


Figure 90. Streamline patterns for a d-type 2D roughness. (Leonardi, Orlandi, Smalley, Djenidi, & Antonia, 2003)

The velocity profile obtained in the present simulation does suggest some form of drag reduction with an upward shift ΔU^+ in the log profile which would be consistent with a 2D riblet. It should be noted however that the strength of the effect seems unlikely given previous observation (Jiménez, 2004) and given the presence of d-type roughness. It is likely that the low mesh resolution adopted in the present study does contribute to this likely over-prediction of the strength of drag reduction.

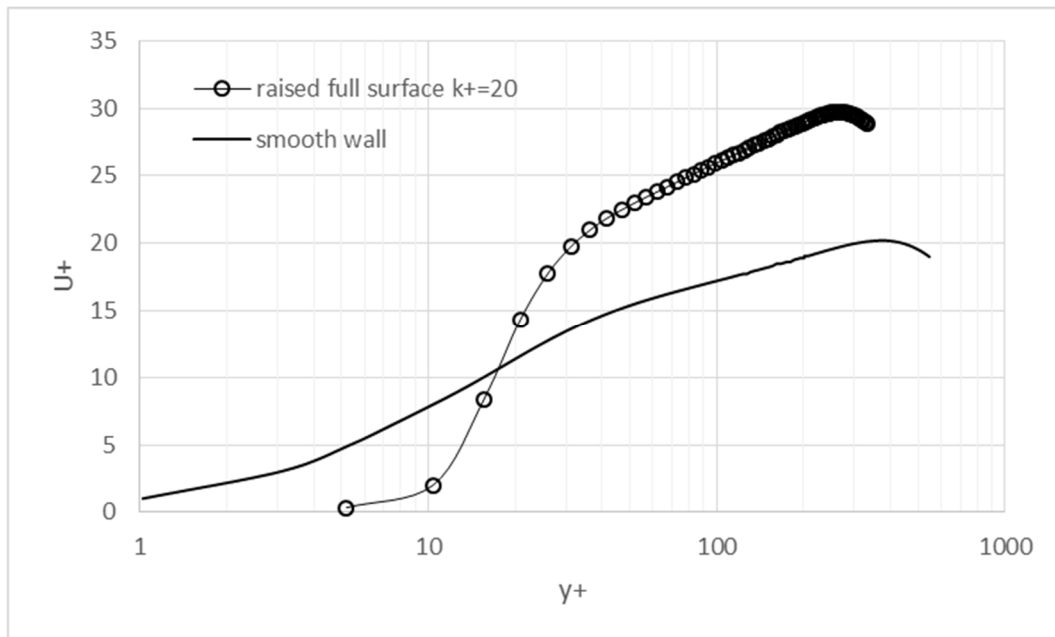


Figure 91 Non-dimensional velocity profile of full cavity vs smooth wall solution. The textures considered here are the raised bars of height $k^+ = 20$ which corresponds to approximately $28 \mu\text{m}$ at the flow conditions expected over Section 9 of the NEMMO turbine blade.

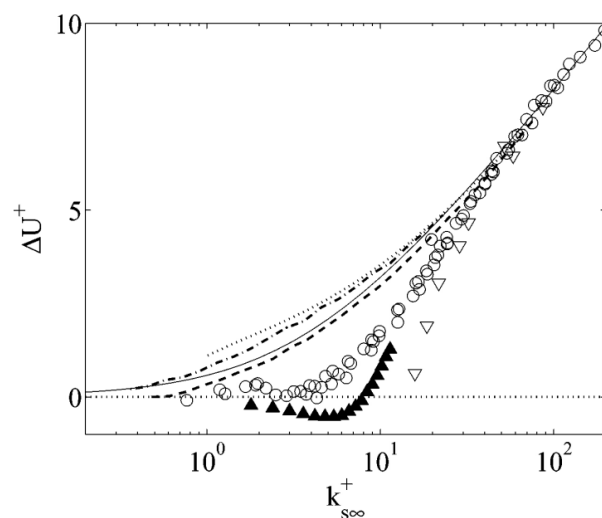


Figure 92 Roughness function vs k_s^+ from different geometries (solid triangular are for triangular riblets. (Jiménez, 2004)

Resolved LES simulation for characterisation of roughness elements

Results presented in the previous section highlighted the need for a higher resolution of the boundary layer including in gaps between roughness elements. Dedicated computational resource for 1 million CPU hours from the Irish Centre for High End Computing (ICHEC) was secured through a funding support application (grant number dcen013b). Results from these additional simulations are presented in this section. A similar domain and geometry is considered with wider roughness element to minimize the increase in the mesh count. The purpose of the simulation is to assess whether the impact of the antifouling textures studied is

similar to that reported in the literature for continuous streamwise rectangular riblets. In particular it is known that for spanwise riblet spacing lower than $S^+ = \Delta z^+ = 20$ some form of drag reduction can be expected. The question is whether the finite length roughness elements will also prevent streamwise vortices from penetrating the inner part the boundary layer. The study has considered two spanwise roughness spacing $S^+ = 20$ and $S^+ = 40$. The simulations are carried out in $Re_\tau = 395$, with $k^+ = 40$ for both the recessed and raised roughnesses. The mesh resolution in the core of the flow domain is $240 \times 286 \times 120$ in the stream-wise, span-wise and normal directions respectively. Near and between roughness elements the non-dimensional cell size is taken close to one: $\Delta x^+, \Delta z^+, \Delta y^+ \cong 1$. The geometry creates four different areas which are the roughness crest plane, the stream-wise valley, the span-wise valley and the intersection of the stream-wise and span-wise valleys.

1.1.1.1 Results for roughness $S^+ = 40$

The non-dimensional velocity profile is shown in Figure 93. The roughness is shown to cause a shift in the logarithmic layer while a total drag increase of nearly 7% is calculated. This is close to the 6% increase reported by Elsamni et al (O.A. El-Samni, 2007) for continuous riblets with a gap of $S^+ = 40$. The roughness layer has been extended by nearly as much as the roughness height itself which shows that roughness type can be considered as a d type roughness.

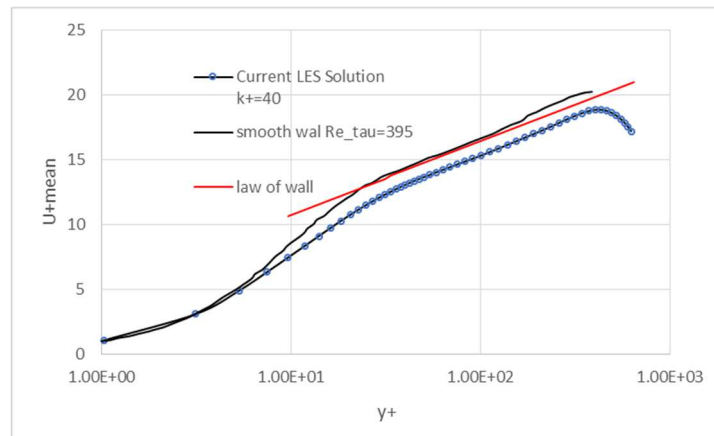


Figure 93 Non-dimensional velocity profile on top of the roughness (crest plane) for $S^+ = 40$

The normal and shear Reynolds stresses are shown against y/δ where δ is half the height of the channel in Figure 94 and Figure 95. These results show that the streamwise turbulent kinetic energy decreases while the spanwise kinetic energy increases. This means that the turbulent structures have become shorter in the streamwise direction and have lengthened in the spanwise. This is compatible with findings from (Leonardi et al (2003) (S. Leonardi, 2004) and Elsamni et al(2007) (O.A. El-Samni, 2007)). The turbulent kinetic energy normal to the wall has also decreased. In addition, Figure 95 right, shows an increase in the Reynolds shear stresses normal to the wall. This effect has previously been associated to the ejection of vorticity from the roughness valleys from the inner part of the boundary layer. This can be expected to contribute to an increase in turbulent stresses and mixing inside the outer layer.

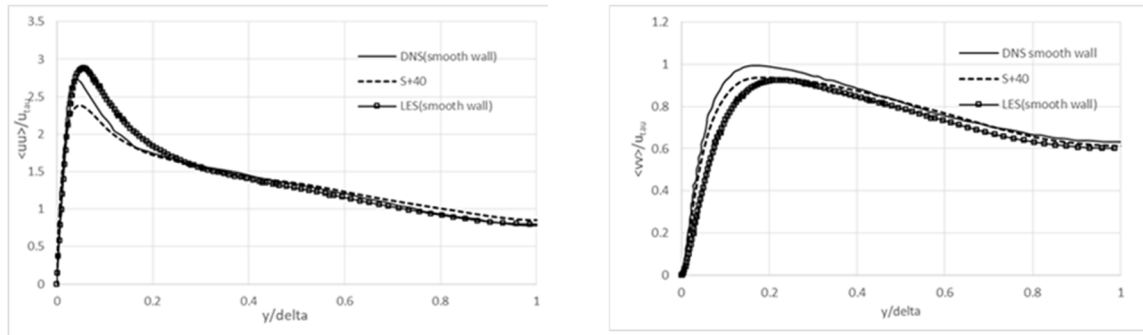


Figure 94 [left] non-dimensional root mean square of $\langle uu \rangle$ versus y/δ for $S^+ = 40$ and [right] non-dimensional root mean square of $\langle vv \rangle$ versus y/δ for $S^+ = 40$; both are measured above the roughness crest plane.

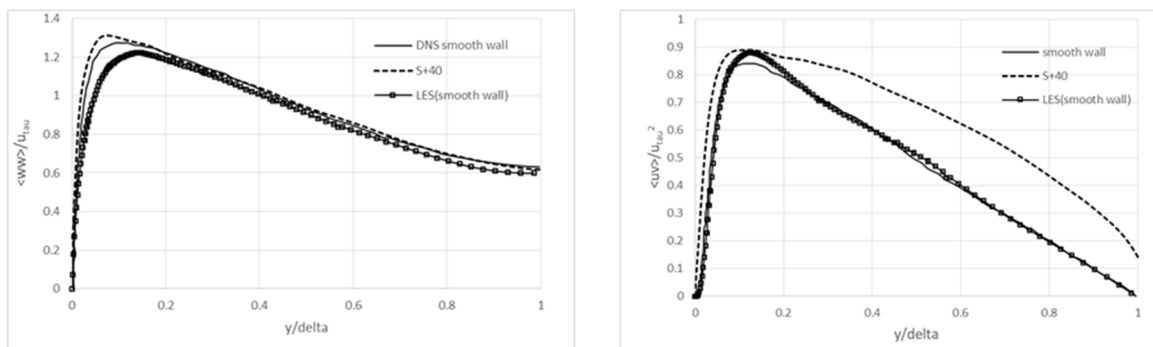


Figure 95 [left] non-dimensional root mean square of $\langle ww \rangle$ versus y/δ for $S^+ = 40$ and [right] non-dimensional Reynolds shear stress versus y/δ for $S^+ = 40$; both are measured above the roughness crest plane.

Roughness with $S^+ = 20$

The non-dimensional velocity profile is shown in Figure 96. The roughness in this case causes a very slight upward shift in the logarithmic layer which indicates a minor drag reduction. This suggests that the discontinuous riblets exhibit the same drag reduction properties reported in the literature for full riblets. The effect has been explained by the role that narrow streamwise gaps ($S^+ \leq 20$) play on the disruption of streamwise vortices which are prevented from penetrating in the gap between roughness elements. This is again agrees with observations made by Elsamni et al (2007) (O.A. El-Samni, 2007) with continuous riblets. Published research on riblets indicates that maximum drag reduction is achieved by reducing the ratio of roughness height to spanwise distance between elements (Bechert et al(2000) (Bechert, Bruse, & Hage, 2000), Elsamni et al(2007) (O.A. El-Samni, 2007)). This can explain the small effect observed here since a reasonably large roughness height has been considered.

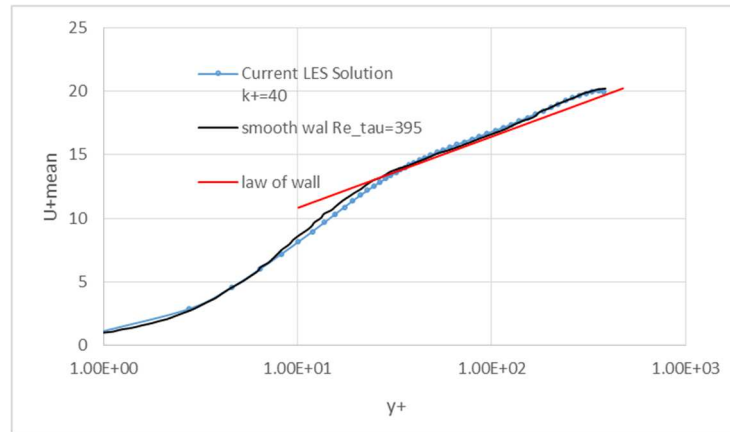


Figure 96 Non-dimensional velocity profile on top of the roughness (crest plane) for $S^+ = 20$

The normal and shear Reynolds stresses are shown against y/δ in Figure 97 and Figure 98. Comparing the stream-wise turbulent kinetic energy distribution against that obtained with $S^+ = 40$ (Figure 94 and Figure 98), shows that the peak value is closer to that of the smooth wall case but a significant reduction is also observed over the outer part of the boundary layer. The spanwise and wall turbulent kinetic energy show minimal changes over most of the boundary layer. Overall the effect of surface texturing on the normal Reynolds stresses is shown to be smaller than with $S^+ = 40$. The Reynolds shear stress is similar in the inner layer but there is increase in outer-layer in compare to $S^+ = 20$. This is in accordance with observation from Orlandi et al (2006) (LEONARDI, 2006) which shows that there is less outward ejection with $S^+ = 20$ since stream-wise vortices cannot penetrate into the gaps. The overall effect is that Reynolds stresses with $S^+ = 20$ shows limited changes compared to the smooth wall results but total drag is reduced as stresses act almost exclusively on the smaller area of the texture crest planes with little activity taking place inside the grooves.

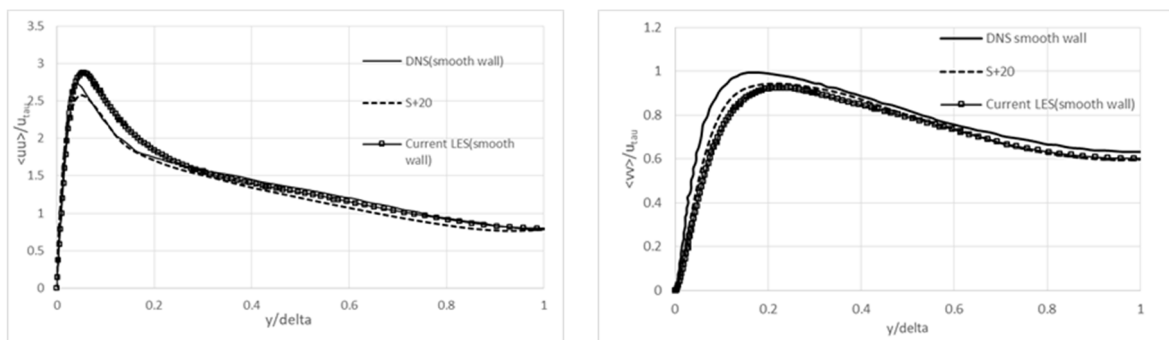


Figure 97 [left] non-dimensional root mean square of $\langle uu \rangle$ versus y/δ for $S^+ = 20$ and [right] non-dimensional root mean square of $\langle vv \rangle$ versus y/δ for $S^+ = 20$; both are measured above the roughness crest plane.

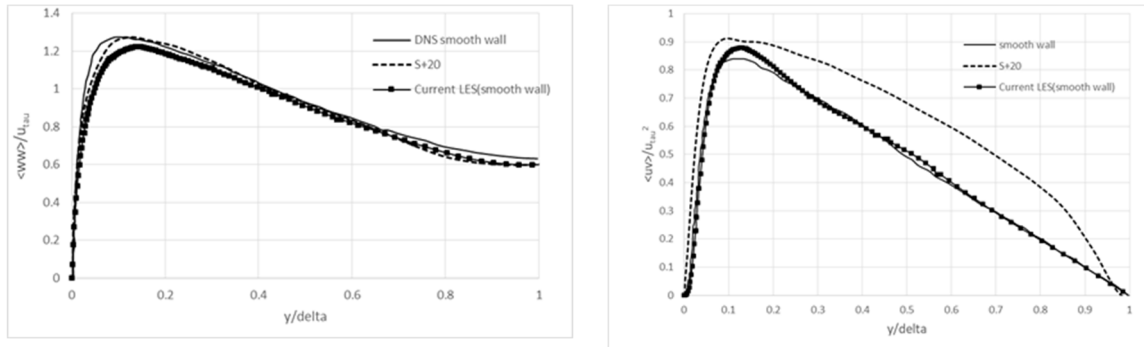


Figure 98 [left] non-dimensional root mean square of $\langle ww \rangle$ versus y/δ for $S^+ = 20$ and [right] non-dimensional Reynolds shear stress versus y/δ for $S^+ = 20$; both are measured above the roughness crest plane.

Stream-wise vortex penetration in side valley

The streamwise turbulent kinetic energy profiles starting at the bottom wall within the roughness gap and extending throughout the boundary layer are shown in Figure 99 for both $S^+ = 20$ and $S^+ = 40$. The measurements are made at the mid-point along the streamwise length of the roughness element. This clearly confirms the lack of turbulent kinetic energy in the valley as the gap is reduced.

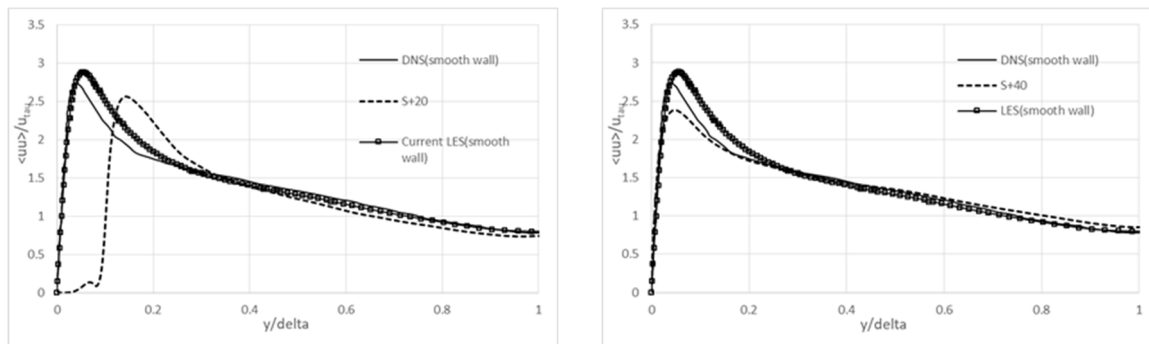


Figure 99 non-dimensional root mean square of $\langle uu \rangle$ versus y/δ ; [left] $S^+ = 20$ and [right] $S^+ = 40$; both are measured above the bottom wall within the roughness valley.

The contours of streamwise vorticity are shown in Figure 100 and Figure 101. These also clearly show the difference in penetration of streamwise vortices toward the gaps while in $S^+ = 20$, this is not the case.

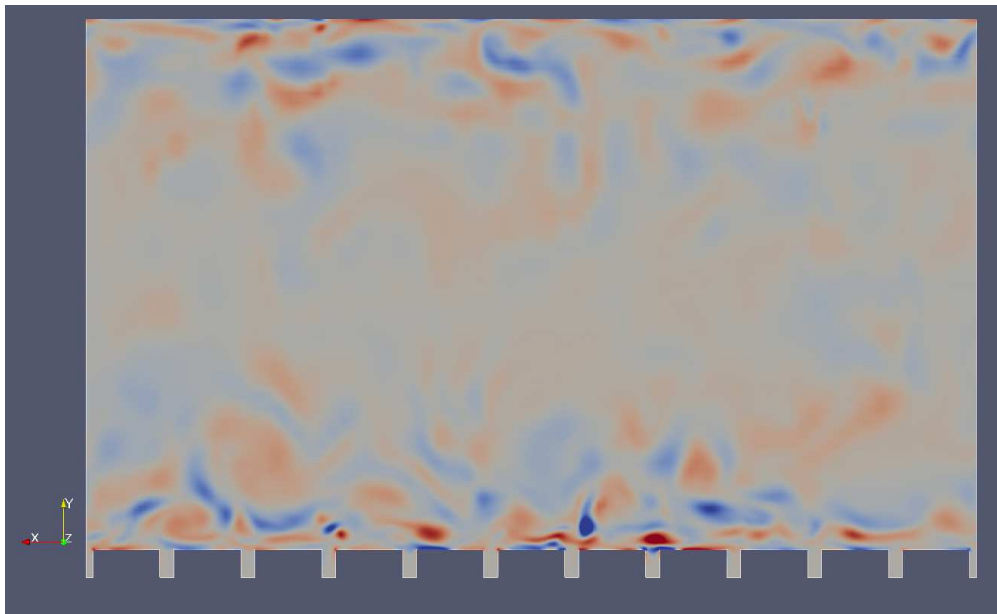


Figure 100 $S^+ = 20$. Upper image: contour of stream-wise vorticity for $-1 \leq \omega_x \leq 1$. Lower image: contour of $\omega_x = 0.1$ vortex

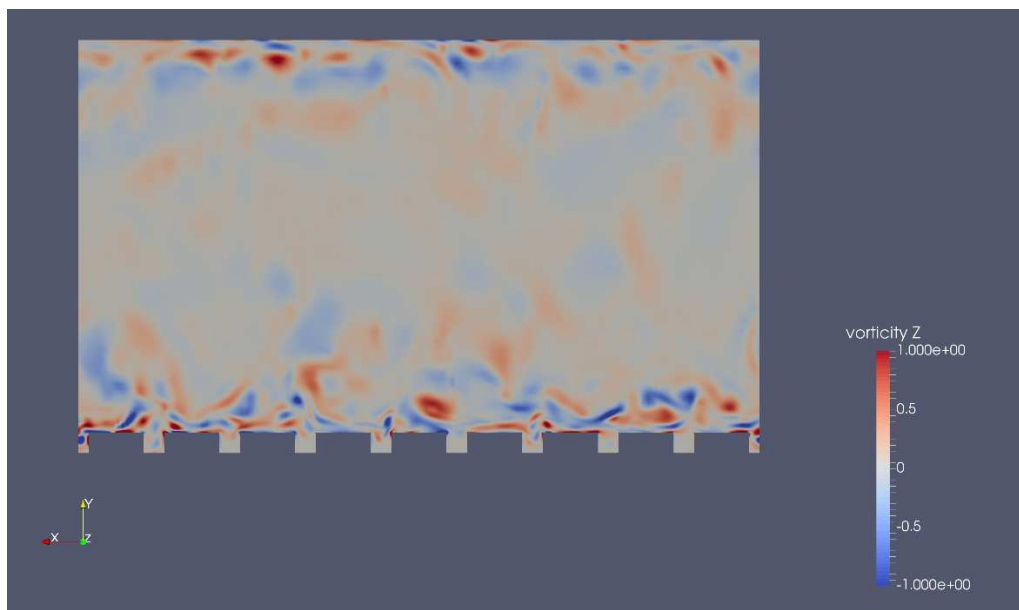


Figure 101 $S^+ = 40$. Upper image: contour of stream-wise vorticity for $-1 \leq \omega_x \leq 1$.

Concluding remarks on surface roughness modelling

The results presented in this section indicate that both types of textures proposed as an anti-fouling strategy are expected to have a minimal effect on the turbulent flow profiles in the overlap region of the boundary layer over the turbine blade surface. It is possible however that an earlier transition to turbulence can result from the increased roughness. Simulations of the transitional flow with wall resolved transitional RANS model indicate that this can cause a moderate decrease in the drag and lift coefficients. Under the high inlet turbulence conditions expected in the field, the blade airfoil is shown

to experience an increase between 2 and 3% in the drag coefficient and a decrease of between 1 and 1.5% in the lift coefficient. The larger impact being caused by larger texture height/depth where two height have been considered ($k^+ = 7$ and $k^+ = 20$). The impact of these changes on the turbine performance can be assessed by reducing the input C_l and C_d curves in the ALM-LES model.

Conclusion: the effect of surface texturing of blade on performance coefficient of Magallanes turbine

The ALM-LES model was used to simulate the full-scale Magallanes turbine accounting for the effect of surface texturing as proposed in Section 0. For modeling the effects of blades, lift and drag coefficients are used, and the coefficients are extracted from the Xfoil-Qblade software. It was concluded that with the inclusion of surface texturing, the coefficient of lift (C_l) value could be expected to decrease by a maximum of 1.5% while the drag coefficient (C_d) would increase by 3% at most. To understand this effect on the performance of the turbines, the full-scale Magallanes turbine was modelled using the ALM-LES method with the modified coefficients (of lift and drag.) at the standard tip speed ratio ($TSR = 6.01$) and inlet flow velocity ($u_\infty = 2.5 \text{ m/s}$). The comparison of the performance with and without texturing is shown in Table 12.

Table 12. Effect of surface texturing on power and thrust

Sr No	Case	Coefficient of power (C_P)	Coefficient of thrust (C_T)
1	Without blade surface texturing	0.49	0.78
2	With blade surface texturing	0.49	0.77

It can be concluded that the effect of the proposed surface texturing of blade on the performance characteristics of the Magallanes turbine can be neglected.

References

- [1] H. C. H. Y. O.A. El-Samni, "Drag reduction of turbulent flow over thin rectangular riblets," *International Journal of Engineering Science*, 2007.
- [2] P. O. a. S. LEONARDI, "DNS of turbulent channel flows with two- and three-dimensional roughness," *Journal of Turbulence*, 2006.
- [3] P. O. L. D. ,. R. A. S. Leonardi, "Structure of turbulent channel flow with square bars on one wall," *International Journal of Heat and Fluid Flow*, 2004.
- [4] Menter, F. R. Menter, R. Langtry and S. Volker, "Transition Modelling for General Purpose CFD Codes," *Flow, Turbulence and Combustion*, vol. 77, no. 1, pp. 277-303, 2006.
- [5] ANSYS, *Fluent Theory Guide*, Release 2019 R2, 275 Technology Drive Canonsburg: ANSYS, Inc., 275 Technology Drive Canonsburg,, 2019.
- [6] J. Nikuradse, "Laws of flow in rough pipes," *VDI-Forschungsheft 361, Series B*, vol. 4, 1933.
- [7] J. Jiménez, "Turbulent flows over rough walls," *Annu. Rev. Fluid Mech.*, vol. 36, pp. 173-96, 2004.
- [8] D. W. Bechert, M. Bruse and W. Hage, "Experiments with three-dimensional riblets as an idealized model of shark skin.," *Exp. Fluids*, vol. 28, pp. 403-412, 2000.
- [9] A. Sigal and J. E. Danberg, "New correlation of roughness density effects on the turbulent boundary layer," *AIAA Journal*, vol. 28, no. 3, pp. 554-556, 1990.
- [10] I. A. Milne, R. N. Sharma, R. G. Flay and S. Bickerton, "Characteristics of the turbulence in the flow at a tidal stream power site," *Philosophical Transactions of the Royal Society A - Mathematical Physical and Engineering Sciences*, vol. 371, no. 1985, 2013.
- [11] J. Cui, V. Patel and C. Lin, "Large-eddy simulation of turbulent flow in a channel with rib roughness," *Int. J. Heat Fluid Flow*, vol. 24, no. 3, pp. 372-388, 2003.
- [12] S. Leonardi, P. Orlandi, R. Smalley, L. Djenidi and R. Antonia, "Direct Numerical and large-eddy simulations of turbulent flows over rough surfaces," *J. Fluid Mechanics*, vol. 491, pp. 229-238, 2003.
- [13] J. Jimenez and A. Pineli, "The autonomous cycle of near-wall turbulence," *J. Fluid Mech.*, vol. 389, pp. 335-359, 1999.

[14] A. A. Townsend, The Structure of Turbulent Shear Flows, Cambridge, UK: Cambridge Univ. Press, 1976.